University of Cape Town

Faculty of Engineering and Built Environment

Department of Mechanical Engineering

Centre for Materials Engineering

MICROSTRUCTURAL AND PROPERTY ASSESSMENT OF CREEP AGED 12Cr STEEL AFTER WELDING

By

Teboho Jacob Molokwane

Supervisors: Prof. B. Sonderegger & Prof. R.D Knutsen

December 2013

A thesis submitted to the Faculty of Engineering and the Built Environment of the University of Cape Town in fulfillment of the requirements for the degree of Master of Science in Engineering.

DECLARATION

I, Teboho Jacob Molokwane, know the meaning of plagiarism and declare that all the work in this document, save for that which is properly acknowledged, is my own.

Signed by candidate

Signature: Signature Removed

Date: 4 June 2014

Abstract

The electricity public utility of Eskom (South Africa) has an ageing fleet of power generation equipment and due to shortage of capacity there is limited time for maintenance and replacements. Complete main steam pipework replacements are not practical and in many instances selective welding must be done on creep aged and sometimes creep damaged material. The question arises whether these repair welds damage the components to an unacceptable degree or not, and a complete replacement can be avoided.

This work aims at studying the effect of the welding process on the damage state of the material on the example of the widely used X20 steel and advising Eskom on the weldability limits of this steel. Real welds consisting of new and creep aged steel were prepared and characterised. Furthermore, the heat input was simulated in additional samples using Gleeble thermo-mechanical equipment.

The evolution of microstructure during welding was characterised using light microscopy, scanning electron microscopy (SEM) and transmission electron microscopy (TEM). Hardness testing, tensile testing and creep rupture tests (cross-weld) were conducted to study the evolution of mechanical properties after the welding process.

The base material (BM), fine-grained heat-affected zone (FGHAZ), coarse-grained HAZ (CGHAZ) and the weld metal (WM) were analysed using the techniques mentioned above to determine change in microstructure and mechanical properties. Finer grained microstructure and coarse distribution of $M_{23}C_6$ precipitates was generally evident in the FGHAZ of the weldments and simulated HAZ samples relative to other regions of the weldment.

Cross-weld creep rupture test specimens ruptured in the FGHAZ of the weldments with creep aged BM. The reason for the decrease in creep strength can be explained by the higher interparticle spacing and finer grain structure. Increased precipitate spacing leads to fewer obstacles for dislocation movement and thus faster plastic deformation. Additionally, the finer grain structure in the FGHAZ leads to higher effective diffusion rates of vacancies and thus explain the higher observed creep rate. Both effects weaken the FGHAZ and therefore explain the decrease in the measured mechanical properties (hardness, hot strength and creep).

Welding on X20 steel BM with life exhaustion of 54% (accumulated 210kh in service) and 44%

(accumulated 130kh in service) is possible. Creep damage models coupled with creep master curves gave good predictions of the weldment creep life when the predictions are carried out using the average creep damage measured on the BM of service exposed X20 Steels.

Acknowledgements

I will like to express my sincere gratitude to the following people for their significant contribution in the course of this research:

- My supervisors, Professor B. Sonderegger and Professor R. D. Knutsen for their valuable suggestions, supervision and guidance throughout this work.
- Dr. J. Westraadt and the staff at Centre for High Resolution TEM, Nelson Mandela Metropolitan University for their great assistance on EBSD analysis and TEM analysis work.
- M. Bezuidenhout, F.C. Havinga, P. Doubell, T. Pete, M. Mkhize, P. Dlamini, Z. Nkosi, P. van der Meer and other Eskom RT&D staff for their mentoring and encouragement throughout my research.
- Dr. S. George, N. Clinning and L. Matthews for their assistance in the Gleeble simulation work.
- T. Thage, M. Mabaso and Eskom (Rosherville) workshop staff for their technical assistance on replica lifting and creep testing.
- Glen Newins and the workshop staff for their technical assistance
- Mrs P Park–Ross for her technical and logistical assistance in the laboratories.
- Ms. B. Glass for all the administrative assistance.
- The staff and students of the Centre for Materials Engineering for their constant words of encouragement.
- Eskom Power Plant Engineering Institute (EPPEI) for their financial supports.

I would also want to thank my late father Mr. L.J. Ramotsabi, my mother, Mrs. A.M. Molokwane, my fiancée, Ms. E.T. Zakwe, my siblings, my relatives and friends for their love, prayers and commitments throughout my life.

Finally and most importantly, I am thanking God for giving me the wisdom and strength throughout the course of this study.

Glossary

X20 – DIN 17175 X20CrMoV12-1

TMFS's – Tempered martensite ferritic steels

HTPP – High temperature pressure pipework

BM – Base metal

HAZ – Heat-affected zone

FGHAZ – Fine-grained HAZ

CGHAZ – Coarse-grained HAZ

WM – Weld metal

WJ – Weld-joint

CO_2 – Carbon dioxide

SC – Supercritical

USC – Ultra-supercritical

PC – Pulverized coal-fired

T_m – Absolute melting temperature

M and X (for precipitates) – Metallic element and carbon and or nitrogen, respectively

T_P – peak temperature

Ac_3 – Upper critical temperature (950ºC)

Ac_1 – Lower transformation temperature (820ºC)

Type IV cracking – cracking in the FGHAZ

α - ferrite

γ – austenite

σ_{eff} – effectively stress

σ_{in} – inner stress

σ_{disloc}, σ_{sg}, and σ_{prec} – strength contributions from dislocations, subgrain boundaries, and precipitates, respectively

CCT – Continuous cooling transformation

Sample ID. – Sample identity

t – Time

T/Temp - Temperature

P/Press – Pressure

ID – Internal diameter

WT – Wall thickness

ASME – American Society of Mechanical Engineers

TIG – Tungsten Inert Gas

MMA – Manual Metal Arc

PWHT – Post-weld heat-treatment

$\Delta t_{8\text{-}5}$ – Cooling time from 800 to 500°C

$T'_{800-500}$ - Mean cooling rate for the temperature range 800°C to 500°C

ECCC – European Creep Collaborative Committee

σ_R – reference stress

HV – Vickers hardness

SEM – Scanning electron microscopy

EBSD – Electron backscatter diffraction

EDX/S – Energy dispersive X-ray/spectroscopy

BSE – Back-Scattered Electrons

SE – Secondary Electrons

FIB-SEM – Focused ion beam SEM

TEM – Transmission electron microscopy

STEM – Scanning TEM

HAADF – High annular angle dark field

SDD – Silicon Drift Detector

Table of Contents

1. Introduction 3
1.1. Background 3
1.2. Motivation of the Research 5
1.3. Research Objectives 6
2. Literature Review 7
2.1. Power Plants 7
2.2. High Temperature and stress 8
2.3. Creep Resistant Steels 12
CMn-Steels 16
Mo Steels 17
CrMo Steels 18
9-12% Cr- Steels 19
2.4. Microstructure of 9-12%Cr Steels 21
2.4.1. Microstructure Evolution during Heat Treatment and Service Exposure 21
2.4.2. Particle Coarsening 27
2.4.3. Microstructural Evolution during Welding 29
2.5. The Back-Stress Concept 33
2.6. X20CrMoV12-1 Steel 35
3. Materials and Experimental Methods 39
3.1. Materials 39
3.2. Welding Procedure 43
3.3. Heat affected Zone Simulations 44
3.4. Mechanical Testing 50
3.4.1. Hardness Testing 50
3.4.2. High Temperature Tensile Testing 50
3.4.3. Creep Testing 50
3.5. Surface Replication Technique and Life Estimates 52
3.6. Light Microscopy Evaluation 56
3.7. Scanning Electron Microscopy (SEM) Analysis 57
3.8. Transmission Electron Microscopy (TEM) Analysis 58

4. Results 62
4.1. Overview on Samples and Investigations 62
4.2. Life Assessment for Service Exposed X20 Steels 63
4.3. Hardness profile of weldments 68
4.4. Creep Rupture Tests and Life Estimates for X20 Steel WJ's 74
4.5. Hot Strength of Simulated Weldings 82
4.6. General Microstructure 84
4.7. Microstructure: Grain Analysis 97
4.7.1. Subgrain Size and Grain Size Calculations 104
4.8. Microstructure: Precipitates Analysis 107
5. Discussion 114
5.1. Life Assessment for Service Exposed X20 Steels 114
5.2. Evolution of Hardness 114
5.3. Creep Rupture Tests and Life Estimates for X20 Steel WJ's 116
5.4. Evolution of Hot Strength 117
5.5. Evolution of Creep Voids 118
5.6. Evolution of Precipitate Parameters 118
5.7. Evolution of Grains 120
6. Conclusions 121
References 123

1. Introduction

1.1. Background

Creep resistant materials have been developed from the early 1900 and the drive has been on improving the efficiency of the power plant (Hagen 2002; EPRI 2006). Improving the efficiency of a power plant means less CO_2 emissions and low consumption of resources (Anand 2006; AGO 2009; Bhattacharya 2011).

Creep resistant steels are mainly used in power generating and petrochemical plants. All product forms are included. Large forgings and castings are used to build turbines, whereas tubes, pipes, plates and fittings are the typical products for application in pressure vessels, boilers and piping systems. High creep strength and other material properties such as hardenability, corrosion resistance and weldability are desired. The importance of such properties depends on the specific application e.g. good hardenability is very important for steel used for large turbine rotors, whereas good weldability is a prerequisite for an application in power plant tubing and piping (Hagen 2002).

Creep resistant steels have been improved over the years by addition of alloying elements such as Cr, V, Nb, N, and B. The increase in chromium content above 7% leads to a group of steels which have a martensitic microstructure as a common feature i.e. 9-12%Cr steels. 9-12%Cr steels are the current state of the art in the power plants. These steels have a tempered martensite microstructure with high dislocation density and finely dispersed precipitates (mainly $M_{23}C_6$ and MX precipitates). This microstructure is obtained after austenitisation and subsequent tempering heat treatment (Maruyama 2001; Hagen 2002; EPRI 2006).

Research into understanding evolution of microstructure and mechanical properties of tempered martensitic ferritic steels (TMFS's) during service exposure or conditions similar to that experienced during service has been conducted by many researchers. The effect of welding on the service behavior of TMFS's has also been a topic for many researches. The deterioration in material properties is closely related to the changes in microstructure such as the increase in subgrain size and coarsening of precipitates (Panait 2010).

Coarsening of $M_{23}C_6$ precipitates during service exposure has been reported. MX precipitates showed resistance to coarsening at service conditions (Aghajani 2009; Panait 2010). Laves phase

forms during service exposure, followed by rapid coarsening. Nucleation of Z-phase was also noticed on some 9-12% Cr steels; this phase forms in expense of MX precipitates (Aghajani 2009).

Reduction in creep strength was evident in the fine-grained heat affected zone (FGHAZ) of 9-12% Cr steel weldments. The reduction in creep strength was due to enhanced creep voids formation in the FGHAZ, leading to early failure (Type IV cracking). The FGHAZ of the 9-12% Cr steels is reported to have coarse distributed precipitates and a fine grained microstructure which lead to accelerated recovery (Tian 1991; Mannan 1999; Francis 2006; Xue 2009).

DIN17175 Grade X20CrMoV12-1 (known as X20) steel belongs to 9-12% Cr steels group and is widely used in the power utilities and petrochemical industries were high creep strength, fatigue, corrosion and oxidation resistance is desired. This alloy is used for superheater and reheater tubes, main-steam pipes, turbine cases and blades and other high temperature components (EPRI 2006).

Eskom is using this material in their power plants and most of their components have operated above 100,000 hours. The long term operation at high temperature and pressure results in accumulation of creep damage in the pipework. Selective welding of creep aged X20 steel pipework is usually conducted and adequate knowledge with respect to the evolution of microstructure and mechanical properties during welding of service exposed X20 steels is required for safe operation of Eskom power plants.

There is little literature reported on the evolution of microstructure and mechanical properties during welding of service exposed X20 steel. Research into this topic will aid in setting weldability limits for service exposed X20 steel pipework.

1.2. Motivation of the Research

Eskom is a South African electricity public utility, established in 1923 as the Electricity Supply Commission (ESCOM) by the government of South Africa in terms of the electricity act (1922). The utility is the largest producer of electricity in Africa, is among the top seven utilities in the world in terms of generation capacity and among the top nine in terms of sales. Eskom operates a number of notable power stations (coal fired, nuclear, hydroelectric and pumped storage, and gas turbines), including Kendal Power Station, and Koeberg nuclear power station in the Cape Town, the only nuclear power plant in Africa (Eskom 2013).

Eskom has ageing fleet of power plant components, and due to shortage of capacity, selective welding has to be conducted on creep aged and sometimes on creep damaged main steam pipework. System replacements are not economical and should be avoided if possible (a loss R2.5million is estimated per day for a 200MW unit – electricity cost is around 54c/KWh). Failure of high temperature pressure pipework (HTPP) could be catastrophic and must be avoided as they could result in life threatening incidents. The balance between early replacements and unsafe operation of critical components should be found for optimum and healthy operation of the power plant.

Eskom has life management strategies that provide healthy operation of HTPP and this life management strategies have been modified over the years to provide best performance out of these systems. Weldability limits for each material are also set in the life management strategies, which is usually done with respect to the creep damage accumulated in service. The weldability limits set, are normally too conservative and do not allow full exhaustion of the components' useful life (Van-Zyl 2000).

Life assessment methods that will allow setting of realistic weldability limits are required for full exhaustion of the components' useful life and safe operation of the component. X20 steel is extensively used in Eskom power plants, and full exhaustion of this components' life is required for economical operation of the plants.

Service exposed X20 steel pipework from Eskom power plants has been made available to study the evolution of microstructure and mechanical properties during welding. The materials used for research are chosen in terms of the creep voids density which was specified by Eskom. Eskom

has qualified welding procedures for service exposed X20 steels used in the research. Weldments consisting of service exposed X20 steel and new X20 steel were prepared during welding procedure qualification and will be analysed in the research project.

1.3. Research Objectives

The objectives of this research are as follows:

- Characterize the microstructure (precipitates, grain structure etc.) in the base material (BM), fine-grained heat affected zone (FGHAZ), coarse-grained HAZ (CGHAZ) and weld metal (WM) of the service exposed X20 steel and new X20 steel weldments to study the evolution of microstructure during welding.
- Simulate the FGHAZ and CGHAZ (using service exposed X20 steels and new X20 steel) using Gleeble thermo-mechanical test apparatus.
- Characterize microstructural evolution after HAZ simulation.
- Hardness measurements on X20 weldments (BM, FGHAZ, CGHAZ and WM) and X20 simulated HAZ samples to study hardness evolution during welding.
- Tensile testing at X20 design temperature using X20 simulated HAZ specimens.
- Conduct cross-weld creep rupture tests at elevated temperatures to study the fracture location of X20 weldments and obtained the creep rupture strength of the X20 weldments.
- Perform creep life estimates in conjunction with creep rupture data to assess weldability for creep aged X20 steels.
- Advice Eskom if there is potential of performing welding on creep aged X20 steel.

2. Literature Review

2.1. Power Plants

Coal is the world's most abundant and widely distributed fossil fuel, with global proven reserves totaling nearly 1000 billion tons (AGO 2009). Given these characteristics, coal has been a key component of the electricity generation mix worldwide. Coal fuels more than 40% of the world's electricity, though this figure is much higher in many countries, such as South Africa (93%), Poland (92%), China (79%), India (69%) and United States (49%). Moreover, the growing energy needs of the developing world are likely to ensure that coal remains a key component of the power generation mix in the foreseeable future, regardless of climate change policy (Anand 2006; Bhattacharya 2011). In coal-fired power plants, efficiency is an important performance parameter. Improving efficiency offers benefits such as:

- reduced emissions of carbon dioxide (CO_2), where a one percentage-point improvement in overall efficiency can result in up to 3% reduction in CO_2 emissions;
- reduced emissions of conventional pollutants; and
- resource preservation through reduction in consumption of coal (Anand 2006).

Considerable progress has been made in the development of highly efficient supercritical (SC) and ultra-supercritical (USC) pulverised coal-fired (PC) technology. While sub-critical plants can achieve efficiencies of 38% to 39%, state-of-the-art USC plants produce a far superior performance. USC plants operating at high steam conditions, with temperatures of 600°C to 620°C and pressures over 25MPa (250bar), result in design efficiencies of 45% to 46% on bituminous coals in some parts of the world. Unit capacity for such plants has reached up to 1100MWe. If ongoing developments in materials are successful, the efficiency of the best PC plants may approach 50% in the next 10 to 15 years. Effective policies must be implemented to accelerate such technology developments towards demonstration and deployment stages (Anand 2006).

2.2. High Temperature and stress

High-temperature alloys are class of alloys, generally complex, which have been developed for specific applications, usually by means of painstaking empirical methods. In retrospect, however, a number of general guidelines have emerged for obtaining high-temperature strength materials. For example, metals with a higher melting point tend to exhibit better creep resistance, largely because the rate of self-diffusion is strongly correlated with homologous temperature (Nabarro 1995).

Metals with lower stacking-fault energy tend to have better creep resistance, since extended partial dislocations have difficulty both in cross slipping and in climbing. Some of the most important creep-resistant alloys are strong at high temperature because the cores of their dislocations dissociate by climb into configurations which cannot glide. The addition of solid solution elements and finely dispersed precipitates impedes dislocation motion, and these are further methods of improving creep strength (Nabarro 1995).

The choice of materials for a given application is governed by balance between several engineering requirements, which often suggest different choices, and by cost. Included in the cost are factors such as direct cost, availability, ease of fabrication and maintenance costs. For example, typical applications for creep-resistant alloys at moderate temperatures (up to 550ºC) include certain furnace parts, piping, bolts, steam turbine rotors, boiler tubes carrying water in power plants and superheater tubes carrying steam in power plants (Nabarro 1995).

In these applications, the cheaper low-alloy steels containing Cr, Mo or V are generally used for moderate stressed parts. If the corrosion or oxidation resistance is important, economic considerations may justify the use of ferritic or austenitic stainless steels which contain higher content of chromium. These are more expensive and may cause more difficulties during the manufacture of a component (Nabarro 1995).

At high temperature, stresses imposed on metal components produce a continuously increasing strain even below the yield point, and result in a phenomenon known as creep. Creep is defined as time-dependent inelastic strain occurring under stress which is lower than yield point (Nabarro 1995).

As the temperature increases, the strength of most materials decreases and elongation may continue for a long time before fracture occurs. The temperature above which continuing slow deformation can be observed differs in different materials. The temperature above which substantial deformation by creep continues for a long time after application of a load is of the order of $0.5T_m$ (where T_m is the absolute melting temperature), although each material must be evaluated individually. At lower temperatures, the creep rate decreases more rapidly with time, in the regime of logarithmic creep (Nabarro 1995). Figure 1 shows the effect of temperature or stress on the creep curve.

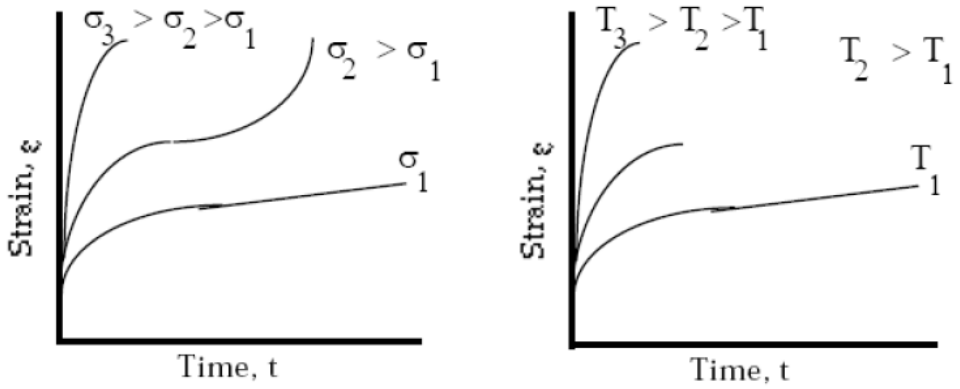

Figure 1: Effect of temperature/stress on creep (ARC).

The continuous plastic flow of a material during creep can eventually result in large plastic deformation and significant modifications to the microstructure of a material, and may terminate in fracture by creep rupture (Nabarro 1995).

Plastic flow is a kinetic process. Although it is often convenient to think of polycrystalline solid as having a well defined yield strength below which it does not flow and above which flow is rapid, this is true only at absolute zero. In general, strength of solid depends on both strain and strain-rate, and on temperature. It is determined by the kinetics of the processes occurring on the atomic scale: the glide motion of dislocation lines; their coupled glide and climb; the diffusive flow of individual atoms; the relative displacement of grains by grain boundary sliding (involving diffusion and defect motion in the boundaries); mechanical twinning (by the motion of twinning dislocations) and so forth. These are the underlying atomistic processes which cause flow. But it is more convenient to describe polycrystal plasticity in terms of the mechanisms to

which the atomistic process contribute. We therefore consider the following deformation mechanisms, divided into five groups (Frost 1982).

1. Collapse at the ideal strength – (flow when the ideal shear strength is exceeded).
2. Low-temperature plasticity by dislocation glide – (a) limited by lattice resistance; (b) limited by discrete obstacles; (c) limited by phonon or other drags; and (d) influenced by adiabatic heating.
3. Low-temperature plasticity by twinning.
4. Power-law creep by dislocation glide, or glide-plus-climb – (a) limited by glide processes; (b) limited by glide processes; (b) limited by lattice-diffusion controlled climb ("high-temperature creep"); (c) limited by core-diffusion controlled climb ("low-temperature creep"); (d) power-law breakdown, (the transition from climb-plus-glide to glide alone); (e) Harper-Dorn creep; (f) creep accompanied by recrystallization.
5. Diffusional Flow – (a) limited by lattice diffusion ("Nabarro-Herring creep"); (b) limited by grain boundary diffusion ("Coble creep"); and (c) interface-reaction controlled diffusional flow.

The mechanisms may superimpose in complicated ways. Certain other mechanisms (such as super plastic flow) appear to be examples of such combinations (Frost 1982).

It is useful to have a way of summarizing, for a given polycrystalline solid, information about the range of dominance of each of the mechanisms of plasticity, and the rates of flow they produce. One way of doing this is shown in Figure 2. The map is divided into fields which show regions of stress and temperature over which each of the deformation mechanisms is dominant. Superimposed on the fields are contours of constant strain-rate: these show the net strain-rate (due to an appropriate superposition of all the mechanisms) that a given combination of stress and temperature will produce (Frost 1982).

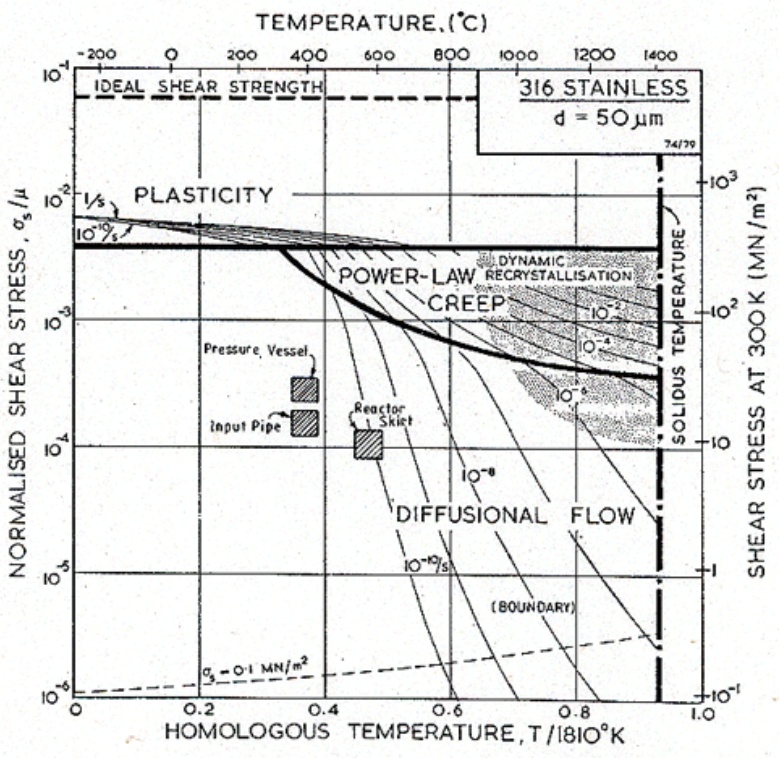

Figure 2: **Stress/temperature map for 316stainless steel with a grain size of 50µm, showing regions of temperature and stress over which each of the deformation mechanisms is dominant (Frost 1982).**

The high-temperature strength of materials and their deformation behaviour at elevated temperatures are affected by several factors. Dislocations may move out of their glide planes by thermally activated cross slip. Since the mobility of atoms and equilibrium concentration of vacancies increase with temperature, diffusion controlled processes become more important at higher temperatures. The mobility of dislocations is thus increased, because they can climb more easily at higher temperatures. New deformation mechanisms come into play, such as the operation of different slip at the grain boundaries (Nabarro 1995).

Recrystallisation, grain growth and the over-ageing of precipitation-hardened alloys affect the long-term properties of materials at elevated temperatures. In addition to changes in the bulk of the material, oxidation and corrosion occur more easily and rapidly at higher temperatures and can influence the mechanical properties, for example by influencing the initiation and growth of cracks (Nabarro 1995).

2.3. Creep Resistant Steels

Creep resistant steels have been used in technical applications for many years. History shows that there has been a fruitful interaction between advances in technology and advances in the development of new steels. New steels had to be developed to put new concepts into practice, and on the other hand new technological concepts were stimulated by the availability of new steels (Hagen 2002).

Creep resistant steels are mainly used in power generating and petrochemical plants. All product forms are included. Large forgings and castings are used to build turbines, whereas tubes, pipes, plates and fittings are the typical products for application in pressure vessels, boilers and piping systems. In addition to high creep strength other material properties are also important, e.g. hardenability, corrosion resistance, and weldability (Hagen 2002).

The importance of such properties depends on the specific application. For example, good hardenability is very important for steel used for large turbine rotors, whereas good weldability is a prerequisite for an application in power plant tubing and piping. Although the different requests from application are reflected by differences in chemical composition, all product forms use the same mechanisms to improve creep strength. The large variety of creep resistant ferritic steel may therefore be covered adequately by an overview of steels used for tubing and piping (Hagen 2002).

The major driving force behind the development of power plant technology has been the requirement for improved economic efficiency. Design improvements as well as the application of new steels with better properties were used in the past to meet this requirement. Figure 3 shows the efficiency increase for hard-coal-fired power plants from 1930 until the present days (Hagen 2002).

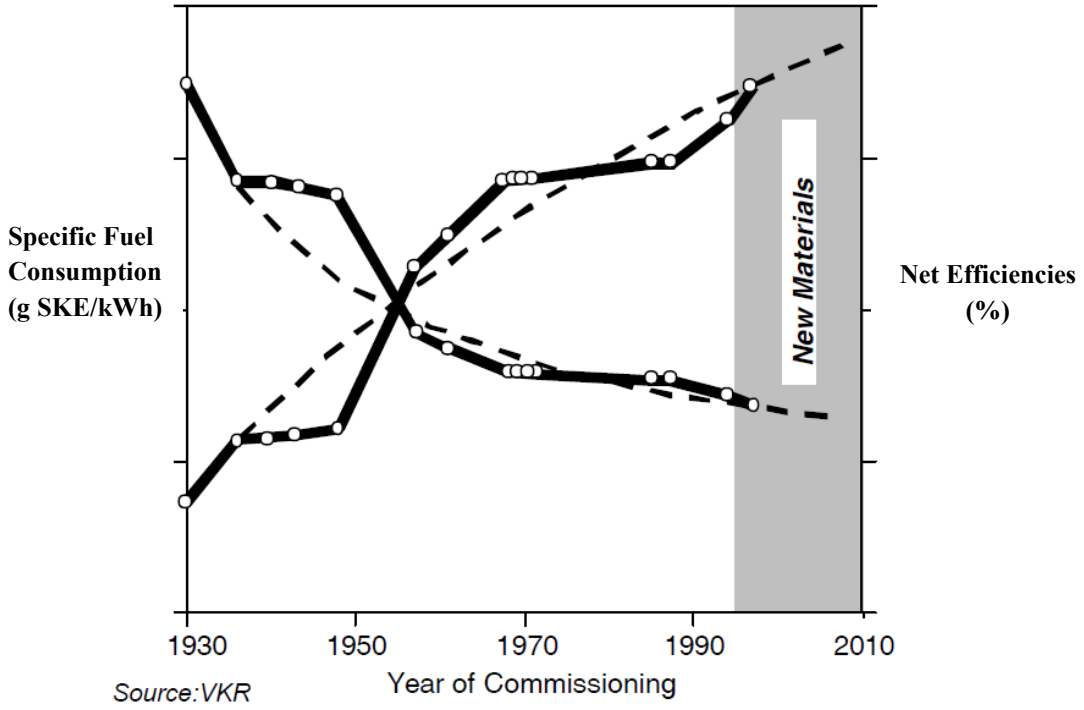

Figure 3: Increase of net efficiencies in hard-coal-fired power plants (Hagen 2002).

The fuel consumption per kWh has decreased by a factor of 2.6 within that time period. This implies an equivalent increase in plant efficiency and a decrease of CO_2 emission per kWh, which is becoming a more and more important issue. The increased efficiency is not described by a smooth curve. It is interesting to note that the kinks in the curve reflect the introduction of a new type of creep resistant steel. Currently we are in such a phase, where efficiency increases due to the recent development of new steels (Hagen 2002).

Table 1 gives an overview on creep resistant ferritic steels which are used in power plants for tubing and piping. The list of steels can be subdivided into CMn-steels (No.1&2), Mo-steels (No.3&4), low alloyed CrMo-steels (No.5-9), and 9-12%Cr-steels (No.10-15).

The steel grades have been listed according to increasing content of alloying elements. As can be seen from Table 2, niobium has been an important element. Niobium bearing steels are found in each group. It has been added for different purposes, as will be discussed later (Hagen 2002).

The complexity of chemical composition is reflected by a complexity in microstructure. Different hardening mechanisms have been used to achieve an optimized product. As a result the

creep rupture strength could have been raised by a factor of about 5-10 according to Figure 4 (Hagen 2002). A more detailed characterization of strength properties of the various steels will be given.

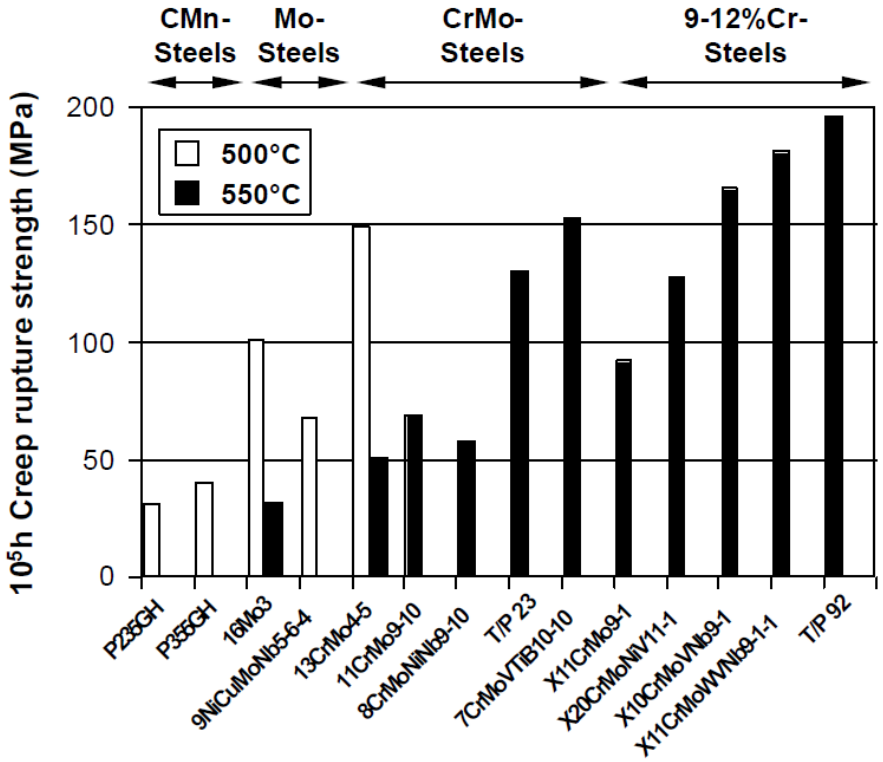

Figure 4: Creep rupture strength of heat resistant steels for tubes and pipes (Hagen 2002).

Creep rupture strength for advanced 9-12%Cr at 600ºC is shown in Table 1.

Table 1: Creep rupture strength at 600ºC for 9-12%Cr steels (Abe 2008).

Steel	Rupture Strength at 600ºC (MPa)	
	10^4h	10^4h
P91	124	94
E911	139	98
P92	153	113
P122	156	101
FB2	-	125
CB2	-	125

Table 2: Chemical compositions of creep resistant ferritic steels for power plants (Hagen 2002).

No.	EN-Designation	ASTM Grade	Chemical composition (wt%)													
			C	Si	Mn	Al	Cu	Cr	Ni	Mo	W	Ti	V	Nb	B	N
1	P235	A	max 0.16	max 0.35	0.40 0.80	min 0.020	max 0.30	max 0.30	max 0.30	max 0.08						
2	P355		max 0.22	0.15 0.35	1.00 1.50	max 0.060								0.0015 0.10		
3	16Mo3		0.12 0.20	0.15 0.35	0.40 0.80	max 0.040				0.25 0.35						
4	9NiCuMoNb5-6-4		max 0.17	0.25 0.50	0.80 1.20	max 0.30	1.00 1.30	0.25 0.50						0.015 0.045		
5	13CrMo4-5	T/P11	0.10 0.17	0.1 0.35	0.40 0.70	max 0.040		0.70 1.10		0.45 0.65						
6	11CrMo9-10	T/P22	0.08 0.15	0.15 0.40	0.30 0.70	max 0.040		2.00 2.50		0.90 1.20						
7	8CrMoNiNb9-10		max 0.10	0.15 0.50	0.40 0.80	max .050		2.00 2.50	0.30 0.80	0.90 1.10				min 10x%C		
8	7CrMoVTiB10-10	T/P24	0.05 0.10	0.15 0.45	0.30 0.70	max 0.020		2.20 2.60		0.90 1.10		0.05 0.10	0.20 0.30		0.0015 0.007	max 0.010
9		T/P23	0.040 0.10	max 0.50	0.10 0.60	max 0.030		1.90 2.60		0.05 0.30	1.45 1.75		0.20 0.30	0.02 0.08	0.0005 0.006	max 0.030
10	X11CrMo9-1	T/P9	0.08 0.15	0.25 1.00	0.30 0.60	max 0.040		8.00 10.00		0.90 1.00						
11	X20CrMoV11-1		0.17 0.23	0.15 0.50	max 1.00	max 0.040		10.00 12.5	0.30 0.80	0.80 1.20			0.25 0.35			
12	X10CrMoVNb9-1	T/P91	0.08 0.12	0.20 0.50	0.30 0.60	max 0.040		8.00 9.50	max 0.40	0.85 1.05			0.18 0.25	0.06 0.10		0.030 0.070
13	X11CrMoWVNb9-1	T/P911	0.09 0.13	0.10 0.50	0.30 0.60	max 0.040		8.00 9.50	0.10 0.40	0.90 1.10	0.90 1.10		0.18 0.25	0.06 0.10	0.0005 0.005	0.050 0.090
14		T/P92	0.07 0.13	max 0.50	0.30 0.60	max 0.040		8.50 9.50	max 0.40	0.30 0.60	1.50 2.00		0.15 0.25	0.04 0.09	0.001 0.006	0.030 0.070
15		T/P122	0.07 0.13	max 0.50	max 0.70	max 0.040	0.30 1.70	10.00 12.5	max 0.50	0.25 0.60	1.50 2.50		0.15 0.30	0.04 0.10	max 0.005	0.040 0.100

CMn-Steels

Steel grade P235 can be regarded as typical of a CMn-steel having a ferrite pearlite microstructure. The carbon and manganese contents are the major factors influencing the strength properties. Figure 5 shows a plot of the minimum 0.2% proof strength values together with the average 10^5h - creep rupture strength as function of temperature. The European design codes are based on minimum proof strength values at low and creep rupture strength values at high temperatures. Both regimes are separated by the intersection of the proof strength with the creep rupture strength curve. In the case of P235 the intersection point is around 420°C. Above this temperature design becomes time dependent, because the lifetime of a component is limited by the creep process (Hagen 2002).

An interesting modification of P235 is the niobium bearing grade P355. The proof strength values could be raised considerably as a result of niobium addition due to grain refinement (Hagen 2002).

However, the increase of creep rupture strength is rather small. This increase can be attributed mainly to the increase of manganese, which is a solution hardening element and also provides a finer pearlite structure. Since proof and creep rupture strength have not increased by equal amounts, the intersection point between the creep and proof strength regime is shifted to 400°C. The advantage of P355 clearly lies in the application below this temperature (Hagen 2002).

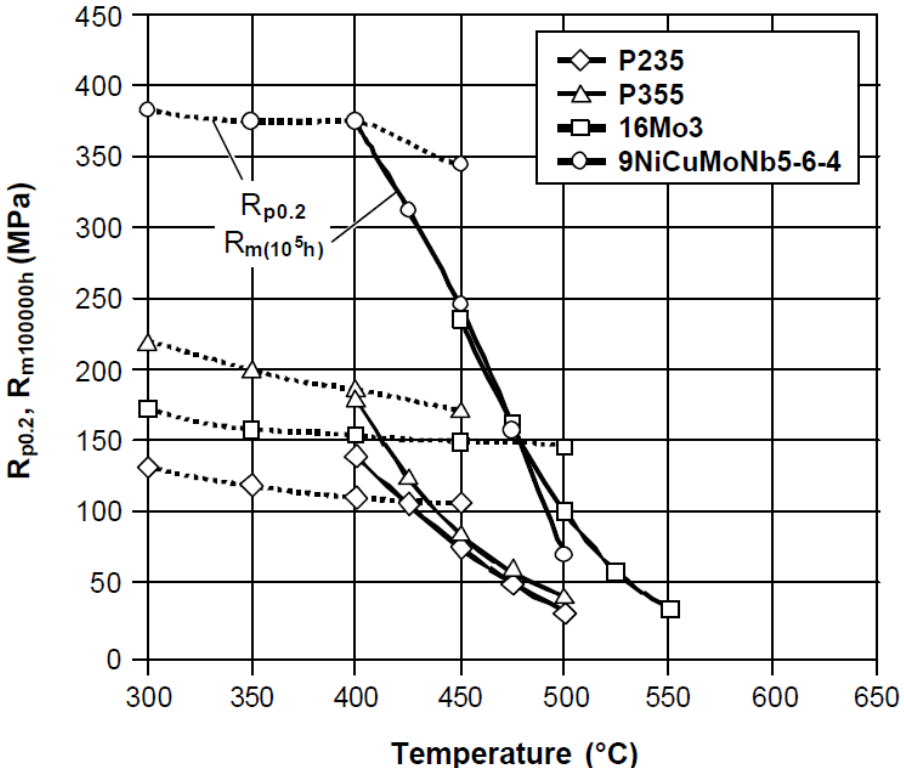

Figure 5: Strength properties of CMn- and Mo- steels (Hagen 2002).

Mo Steels

A similar effect can also be seen for the Mo- steels, which are also represented in Figure 5. These steels are basically of the same type with about 0.3% molybdenum, which is a strong solution hardening element. The solution hardening effect is the main cause for the increase of creep rupture strength, which is similar for both steels. Grade 9NiCuMoNb5-6-4, also well known as WB 36, shows a dramatic increase of proof strength, which again is partly caused by the grain-refining effect of niobium. In addition hardening by copper precipitation increases the proof strength (Hagen 2002).

The following carbides re formed in molybdenum steels as the Mo/C content ratio of the steel is increased under the equilibrium condition: M_3C, $M_{23}C_6$, M_2C, M_3C^*, M_6C. Where M_3C represent Fe_3C containing molybdenum. $M_{23}C_6$ represents $Fe_{21}Mo_2C_6$ containing iron solid solution. M_3C^* is the Fe-Mo-C ternary carbide (Fe_2MoC). M_2C represents the molybdenum carbide containing iron and M_6C represents the continuous series of solid solution between Fe_4Mo_2C and Fe_3Mo_3C (Tamaki 1982).

CrMo Steels

It has been found that the strengthening effect of molybdenum cannot fully be used, since creep ductility strongly decreases with increasing molybdenum content. Another limitation in the application of Mo-steels is the observed decomposition of iron carbides above 500°C (graphitization). A solution to both problems was the use of chromium as an alloying element in combination with molybdenum. In fact CrMo-steels were the first ones that allowed steam temperatures in power stations above 500°C (Hagen 2002).

The carbides present in the CrMo steels are similar to those present in Fe-Cr-C (Cr steels) and Fe-Mo-C ternary systems i.e. M_3C, M_7C_3, M_2C, M_3C^*, M_6C (Tamaki 1982).

The classical CrMo steels are 13CrMo4-5 (T/P11) and 11CrMo9-10 (T/P22). Their creep rupture strengths are distinctly higher than the simple Mo-steels (Figure 6), which is mainly a result of higher Mo content. CrMo steels form chromium carbides which are stable above 500°C. Therefore graphitization is no longer a problem. Chromium also promotes the use at higher temperatures due to its positive influence on oxidation resistance (Hagen 2002).

The steels 7CrMoVTiB10-10 (T/P24) and T/P23, also represented in Figure 5, reveal extremely high strength properties. These are newly developed steels on the basis of T/P22. Having a similar microstructure as T/P22, their strengths properties have been raised considerably by additional alloying with titanium, vanadium and boron in the case of T/P24 as well as tungsten, vanadium, niobium and boron in T/P23 (Hagen 2002).

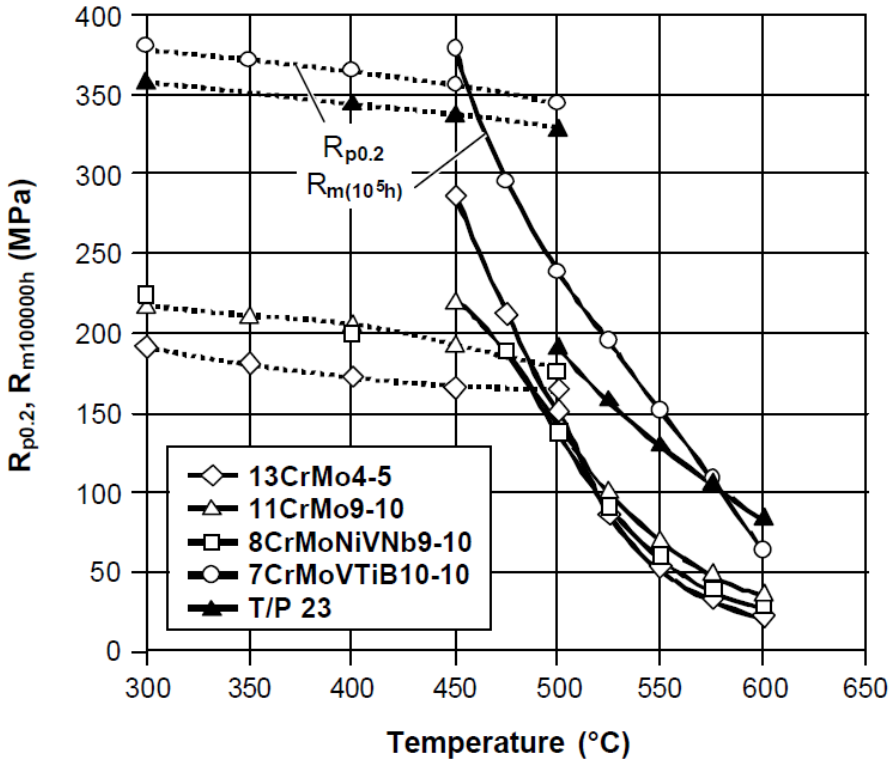

Figure 6: Strength properties of CrMo- steels (Hagen 2002).

Another interesting steel of this group is 8CrMoNiNb9-10. This is also a niobium bearing steel which reflects another facet of its use in creep resistant ferritic steels. The steel has been developed for nuclear applications in liquid sodium cooled fast breeder reactors. A problem has arisen from the use of low chromium ferritic steels, like T/P22, in combination with high chromium austenitic steels. The higher carbon affinity of the high chromium austenitic steel caused a massive diffusion of carbon from the ferritic steel via the liquid sodium into the austenitic steel. As a result a strong decrease of strength occurred in the ferritic steel and an embrittlement in the austenitic steel. The problem was solved by alloying T/P22 with niobium leading to the formation of niobium carbides instead of chromium carbides. The stronger affinity of carbon to niobium prevents a carbon depletion of the ferritic steel and consequently a decrease in strength (Hagen 2002).

9-12% Cr- Steels

The increase of chromium in CrMo- steels above 7% leads to a group of steels which have a martensitic microstructure as common feature. This microstructure introduces a new element of

structural hardening. It is characterized by a high dislocation density and a fine martensite lath structure which is stabilized by $M_{23}C_6$ precipitates. Thus structural hardening is responsible for the large increase in strength of X11CrMo9-1, as compared to 11CrMo9-10 (Figure 6). Further improvements of especially the creep strength have been achieved by alloying with vanadium, niobium, tungsten and boron. The introduction of X20CrMoNiV11-1 at the beginning of the sixties has been a major step to increase power plant efficiency, which can clearly be seen in Figure 7. Its creep rupture strength at a temperature of 540°C is nearly twice that of the low-alloy ferritic steels available at that time (e.g. 10CrMo9-10 with a10^5h- creep rupture strength of 78 MPa compared to 147 MPa for X20CrMoNiV11-1) (Hagen 2002).

Transformation behavior and microstructure is comparable to X11CrMo9-1. The higher creep rupture strength of X20CrMoNiV11-1 is mainly caused by the higher amount of $M_{23}C_6$ carbides as caused by the higher carbon content (Hagen 2002).

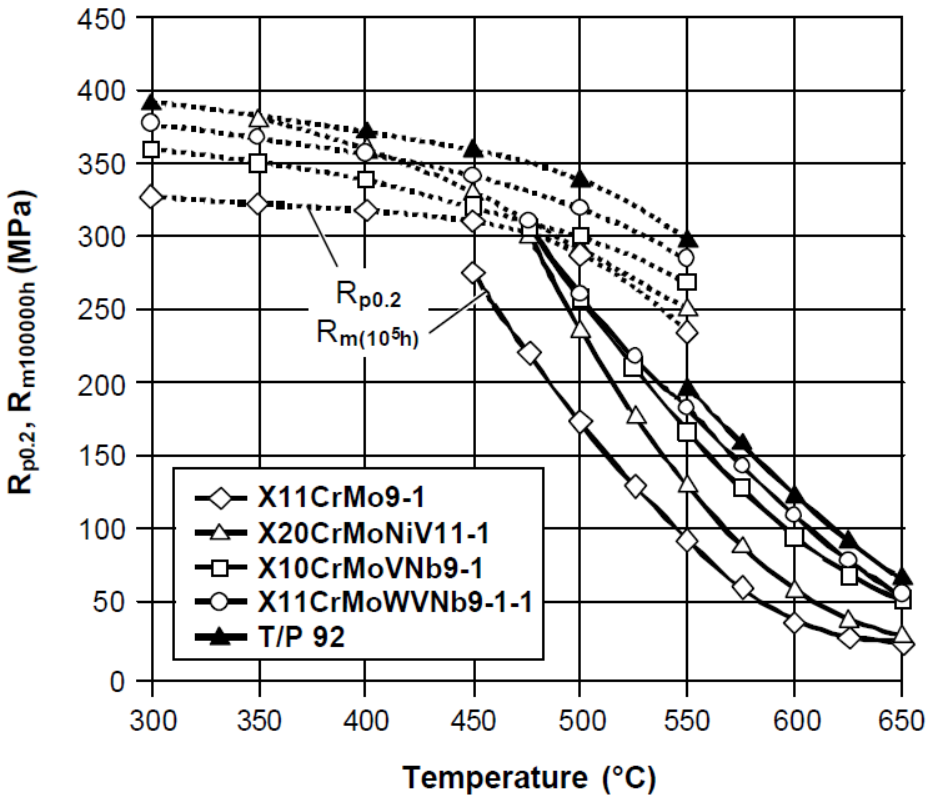

Figure 7: Strength properties of 9-12% Cr steels (Hagen 2002).

After a period of standstill, the material development was reactivated by work carried out in the

USA and Japan in the mid seventies. The prototype of the new steels from this development work is the modified 9% Cr steel T/P91 (EN designation: X10CrMoVNb9-1) invented in the USA. Meanwhile this steel is well known and applied in power plants all over the world. It is used in new plants as well as in refurbishment work of high pressure/high temperature piping systems. Although the carbon content is lower, the creep rupture strength of T/P91 is distinctly higher than that of X20CrMoNiV11-1 (Hagen 2002).

This has been achieved by alloying with vanadium and niobium. T/P91 uses the precipitation of finely dispersed Nb/Vcarbonitrides of type MX as additional strengthening effect. It was essential to balance the composition, because an optimum dispersion and particle size of MX can only be achieved by an optimized Nb/V- ratio and nitrogen content (Hagen 2002).

Subsequently new steel grades have been developed on the basis of T/P91, like X11CrMoWVNb9-1-1 (T/P911), T/P92 and T/P122 (Hagen 2002).

2.4. Microstructure of 9-12%Cr Steels

2.4.1. Microstructure Evolution during Heat Treatment and Service Exposure

The heat treatment of martensitic Cr steels is basically characterized by a normalizing treatment in the austenite regime (usually between 1040°C and 1100°C) and several tempering cycles at temperatures between 650°C and 780°C, depending on the kind of component (e.g. rotors, boiler tubes or pipes) (Maruyama 2001). After austenitising, during air cooling, due to the high Cr concentration the material transforms entirely into martensite (Krauss 1999). The prior austenite grains are divided into packets and further into blocks, as shown schematically in Figure 7(a). The microstructure in this state is characterized by the martensitic lath structure and a high density of dislocations (Sonderegger 2005).

During the tempering treatment dislocation density reduces and a dislocation substructure is introduced. This subgrain structure is characterized by small angle grain boundaries due to the reconfiguration of dislocations during annealing. These small angle boundaries must not confound with martensitic lath boundaries, still present in the material (Sonderegger 2008). The EBSD measurements showed that there is a definite difference in misorientations between subgrain and martensite lath boundaries. While misorientations of small angle grain boundaries are completely random, martensite lath boundaries show preferential axes-angle combinations.

However, it can be often found in literature that, martensitic lath and block boundaries are regarded as elongated subgrains (Maruyama 2001; Abe 2008).

Depending on the effective chemical composition of the material, different secondary phases precipitate during tempering, whereas $M_{23}C_6$ and/or MX carbo-nitrides are considered as main strength determining precipitate phases present in the material (Foldyna 1996; Hald 1996; Maruyama 2001; Sawada 2001; Hofer 2002; Barkar 2005; Bose 2005; Lee 2006; Kostka 2007; Dimmler 2008; Mayer 2008; Shen 2008). The Cr carbides $M_{23}C_6$ are generally located on grain and subgrain boundaries (Hald 1996; Cerri 1998; Hättestrand 2001; Gustafson 2002; Bose 2005). After tempering, in the so-called 'as-received' condition, $M_{23}C_6$ can reach sizes of about 50-100nm (Cerri 1998; Gustafson 2002; Sonderegger 2005; Abe 2008).

The smaller MX carbo-nitrides are commonly classified into VN and NbC (Lee 2006). However, parts of the N in VN and C in NbC can be substituted with C and N, respectively (Ennis 1997; Sonderegger 2005). These precipitates nucleate within subgrains, on subgrain boundaries and on dislocations. The MX precipitates range typically between 20-50nm size in the 'as-received' condition (Gustafson 2002; Sonderegger 2005; Abe 2008).

The effect of these precipitates on creep strength of 9-12% Cr steels must be respected as superior compared to the $M_{23}C_6$ precipitates. The precipitates are located within the subgrains as well as on sub-boundaries (Hald 1996; Gustafson 2002; Abe 2008). Thus, in the 'as-received' condition the microstructure of 9-12% Cr steels is characterized by prior austenite grains which imply martensite lath and subgrain boundaries together with small finely distributed precipitates, as shown schematically in Figure 8.

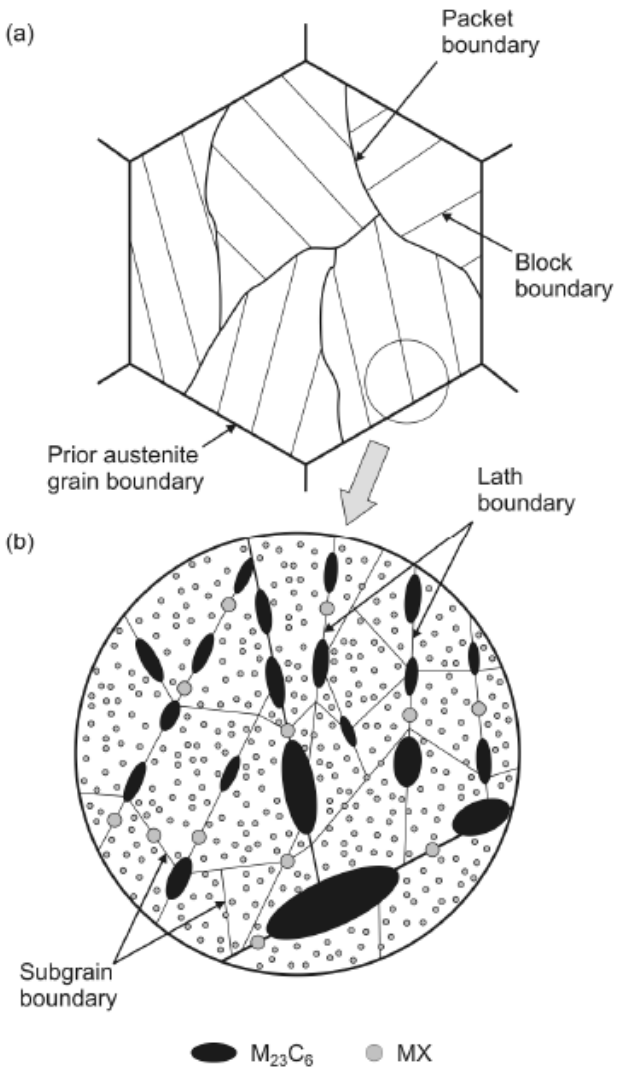

Figure 8: Schematic illustration of tempered martensitic microstructure of 9-12% Cr steels (Holzer 2010).

The high Cr ferritic steels (9-12%Cr steels) contain several obstacles to dislocation motion. They are sub-boundaries, free dislocations within subgrains, and $M_{23}C_6$, Fe_2M (Laves phase – forms during service exposure) and MX particles. Solute atoms such as Mo and W can contribute to creep strength. The strengthening mechanisms attributed to these obstacles are classified into the following categories (Maruyama 2001):

- Dislocation hardening: sub-boundaries and free dislocations.
- Particle hardening: $M_{23}C_6$ and Fe_2M on sub-boundaries and MX within subgrains.
- Solution hardening: W and Mo in solution.

The dislocation substructure of tempered martensitic steel is essential stable at high temperature, but plastic deformation promotes its recovery. The free dislocation density within the subgrains decreases and the subgrain width increases with the progress of creep deformation. These changes are the typical recovery process of the dislocation substructure (Maruyama 2001).

Recovery of the dislocation substructure controls creep deformation and subsequent creep failure. High resistance to recovery of dislocation substructure is essential to keep a good creep resistance for a long duration (Maruyama 2001).

Two processes have been pointed out on the recovery of the subgrain substructure.

(a) Disappearance of a sub-boundary by annihilation of dislocations constructing the sub-boundary (dislocations moving from the interior into the subgrain boundaries may annihilate dislocation with an opposite Burger's vector within the boundary and will increase the misorientation angle across the subgrain boundary and hence the subgrain boundary's energy, which makes it more mobile. In some steels, this may even initiate recrystallisation),

(b) mutual annihilation of two sub-boundaries with opposite signs,

The first process is dominant at least in the first stage of recovery, though the latter process may occur at the latter stage. Dislocations constructing sub-boundaries are in their stable position after tempering, and it is difficult for them to climb sub-boundaries. However, if dislocations glide into the sub-boundaries from sub-grain interior, they disturb the balance in the sub-boundaries and results in annihilation of dislocations in the sub-boundaries. As a result, the dislocation density decreases in the sub-boundary and in the sub-grain interior as well (Maruyama 2001).

The annihilation rate of dislocations at sub-boundaries is proportional to the product of number of dislocations supplied per unit length of sub-boundary and the climb velocity of dislocations. In order to reduce the annihilation rate, velocity of free dislocations within the sub-boundaries is required to be small. Dispersion of fine MX particles is necessary to keep the velocity of free dislocations within the subgrains small and retain fine subgrains (Maruyama 2001).

The interaction force between dislocations increases with increasing dislocation density, this result in high driving force for recovery in high Cr tempered martensitic steels. A large pinning force of particles is necessary to compensate for the large driving force for recovery. This

pinning force is related to interparticle spacing. A fine interparticle spacing of precipitates is needed to keep fine subgrains for a long duration (Maruyama 2001).

Major particles in the high Cr ferritic steel are MX carbo-nitride within subgrains and $M_{23}C_6$ carbide and Fe_2M Laves phase on the sub-boundaries. The particles on the sub-boundaries act as obstacles to dislocation climb motion and slow down the recovery of subgrain structure. The density of $M_{23}C_6$ is significantly higher than that of Fe_2M, suggesting that $M_{23}C_6$ particles are the major obstacle to dislocation climb at subgrain boundaries (Maruyama 2001).

Coarsening of $M_{23}C_6$ precipitates is evident after service exposure of 9-12%Cr steels as shown in Figure 9 and Figure 10 (Panait 2010). Increase in particle size and decrease in particle density is noticed (Aghajani 2009; Panait 2010). $M_{23}C_6$ particles which are in contact with subgrain boundary were found to coarsen faster than carbides which loose contact during creep (which is the evidence of short-circuit diffusion along subgrain boundaries) (Kostka 2007; Hald 2008). The stability of $M_{23}C_6$ carbides against coarsening is reported to be improved by boron addition (Abe 2008), but also significantly by loss of Mo and W from solid solution through Laves phase precipitation (Aghajani 2009).

MX precipitates indicated much stable behavior during creep, were negligible changes in particle size and distribution is observed as shown Figure 9 and Figure 10 (Cerri 1998; Gustafson 2002). MX carbonitrides rich in V and Nb are extremely stable against coarsening, but may be dissolved by precipitation of complex nitride Z-phase (Cr(V,Nb)N). This is mainly a problem in Nb-containing steels with Cr contents of 10% and above (Aghajani 2009).

Precipitation of Laves phase was detected after creep exposure and this was reported to have a potential effect on the creep strength. These precipitates are reported to nucleate and grow rapidly during service exposure (Aghajani 2009). The formation and growth of Laves phase can be promoted by addition of silicon (Armaki 2011).

A decrease in dislocation density within sub-grains and a heterogeneous subgrain growth was reported after creep deformation (Aghajani 2009; Panait 2010). The as-received material and the crept material states showed significantly higher scatter in the local dislocation densities (Pešička 2003).

Loss of creep strength in 9-12%Cr steels is proposed to be due to coarsening of $M_{23}C_6$ carbides, significant precipitation and coarsening of Laves phases, the replacement of finely distributed MX particles by coarse Z-phases and significant recovery of the matrix (Aghajani 2009; Aghajani 2009; Panait 2010). The significant coarsening of precipitates during creep accelerates the degradation of microstructure and assists the breakdown in creep strength (Pešička 2010).

It was also established that precipitate hardening controls long-term microstructure stability, and solid solution strengthening from Mo and W plays no significant role in the long-term microstructure stability of 9 – 12% Cr steels (Aghajani 2009).

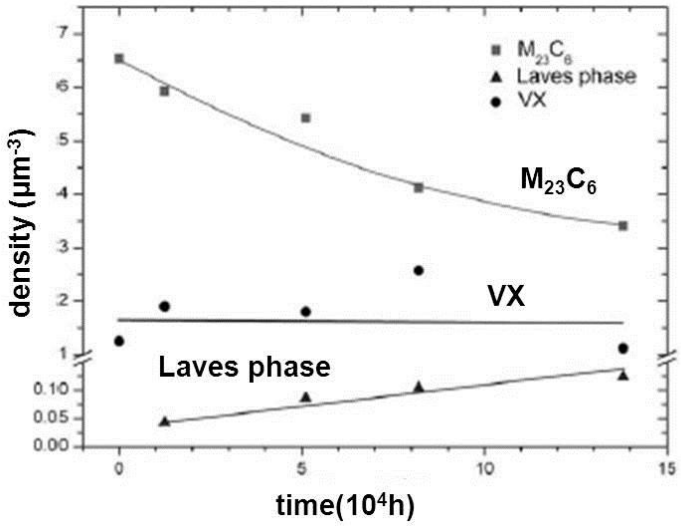

Figure 9: Evolution of number density for $M_{23}C_6$, VX and Laves phase during creep (Aghajani 2009).

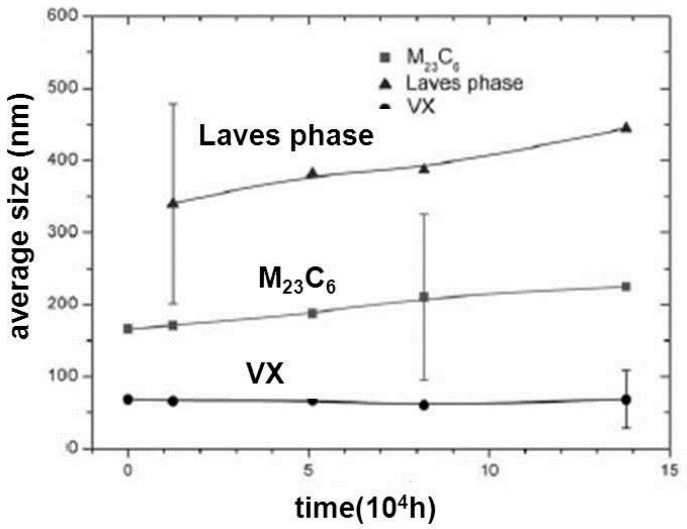

Figure 10: Evolution of precipitate mean diameter for $M_{23}C_6$, VX and Laves phase during creep (Aghajani 2009).

2.4.2. Particle Coarsening

The mechanism of creep strengthening by secondary phase particles, known as precipitate strengthening was reviewed by Pickering et al. (Pickering 1978). In order for mobile dislocations to negotiate non-deformable precipitates within the matrix, the applied stress must be sufficient to force the dislocations to cut the precipitates or 'loop' between them. This critical stress for the latter process is known as the Orowan stress, and is inversely proportional to the inter-particle spacing. In other words, the higher the number of precipitates, the larger the (Orowan) stress needed to achieve dislocation motion around these precipitates. The following relationship illustrates this (Holzer 2010):

$$\tau = \frac{kb}{\lambda} * ln\frac{r}{b} \text{ ... Equation 1}$$

where τ is the critical resolved shear stress, λ is the inter-particle spacing, r is the average radius of intersection between particle and slip plane, and b is the Burgers vector.

Precipitates within alloys like the 9-12% chromium steels such as the face centred cubic MX structure are often coherent with the matrix after tempering, with low interfacial energies around 0.05J/m^2 (Gladman 1998). The interfacial energy between a coherent particle and the matrix within which it is embedded is low. Coherency with the matrix also has the added benefit of high

precipitate pinning force. This is because in order for the grain boundary concerned to move, the particles must rotate, dissolve or re-precipitate; otherwise their coherency will be lost. An increase in the interfacial energies can occur as a result of loss of coherency brought about by precipitate coarsening. From a thermodynamic perspective, the driving force for the coarsening of MX precipitates should be comparatively low as coarsening actually increases interfacial energy. On the other hand, the loss of coherency during precipitate growth leads to a reduction in the Orowan stress, since coarsening increases inter-particle spacing, thereby allowing dislocations to loop with greater ease.

Increase in mean particle size as a result of creep/thermal exposure (strain and/or time at temperature) in these steels is well documented. The coarsening process that occurs during creep can be attributed to the 'Ostwald ripening' mechanism. This is a thermally induced, time dependent, diffusional process and has been described by Nutting (Nutting 1998) and Gladman (Gladman 1998) as follows. Ostwald ripening is characterised by an increase in mean particle diameter, mean inter-particle spacing and a reduction in the number of particles, although the volume fraction remains unchanged. Within the microstructure of a material such as the tempered martensitic steel P91, secondary phase precipitates over a distribution of particle sizes exist, primarily along grain boundaries but also within the subgrains. After sufficiently long exposure at high enough temperatures, larger particles grow at the expense of smaller particles, which go into solution. Atoms from smaller particles migrate by bulk diffusion through the matrix and deposit on larger particles. The driving force for this process is a reduction in the total interfacial energy. The coarsening process is also time-dependent, as can be seen from the Ostwald ripening law:

$$d^3 = d_o^3 + k.t \ldots \text{Equation 2}$$

where d is the mean particle size after creep, do is the particle size at $t=0$, and k is the particle growth rate.

A concentration gradient exists in the matrix, between the elements of the particle that are dissolving and the precipitates. Consequently, the solute will diffuse along this gradient from small particles to larger particles.

The Ostwald ripening theory has been shown not to sufficiently predict the coarsening rate of precipitates and this led to development of new simulation methodologies (Holzer 2010).

2.4.3. Microstructural Evolution during Welding

During welding process, gradients of microstructures are formed near the fusion zone due to different thermal cycles experienced. The area which experience this transformation is referred to as the heat-affected zone (HAZ). The microstructural regions of a ferritic weldment are illustrated in Figure 10 and characterized as follows (Middleton 1996):

- Coarse-grained HAZ (CGHAZ): Material near the fusion boundary that reaches a temperature well above Ac_3 during welding. Any carbides which constitute the main obstacle to growth of the austenite grains, dissolve resulting in coarse grains of austenite. In the 9–12% Cr steels, this austenite transforms into martensite on cooling.
- FGHAZ: Away from the fusion boundary where the peak temperature T_P is lower, but still above Ac_3. Austenite grain growth is limited by the incomplete dissolution of carbides. Fine grained austenite is produced, which subsequently transforms into martensite in the 9–12% Cr steels.
- Intercritical region (ICHAZ): Here $Ac_1 < T_P < Ac_3$, resulting in partial reversion to austenite on heating. The new austenite nucleates at the prior austenite grain boundaries and martensite lath boundaries, whereas the remainder of the microstructure is simply tempered. The austenite (in 9–12%Cr steels) transforms into untempered martensite on cooling.
- Over tempered region: With T_P below Ac_1, the original microstructure of the plate material undergoes further tempering.

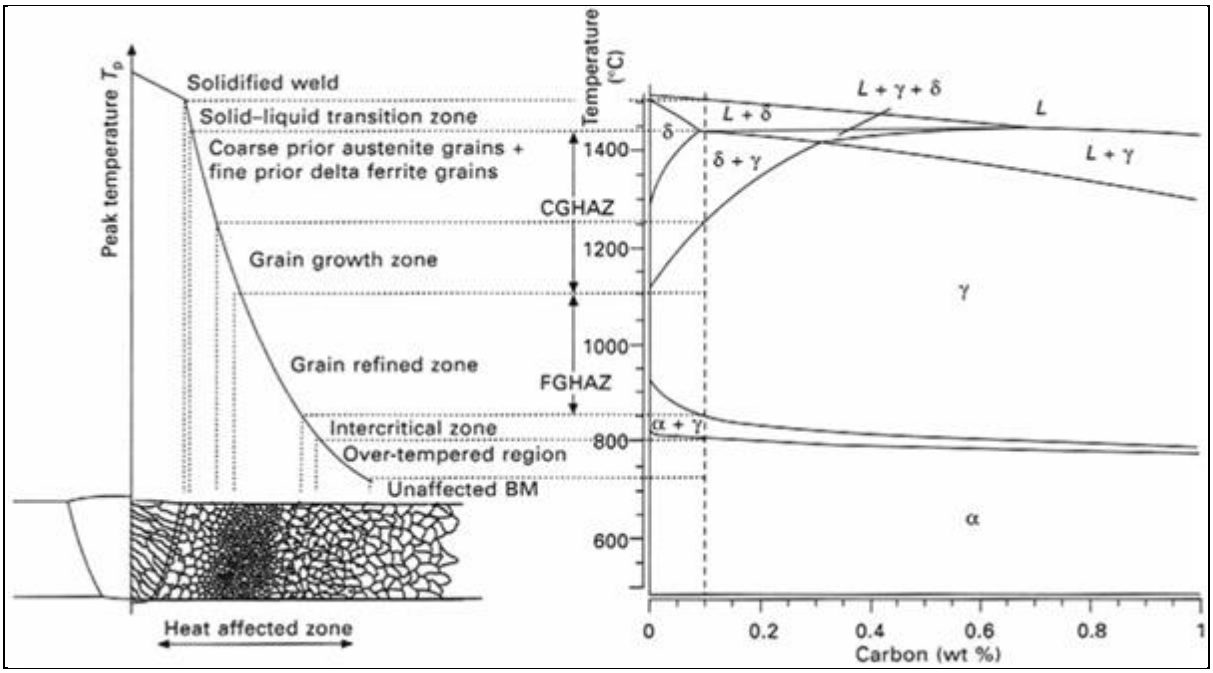

Figure 11: Schematic representation of microstructures developed in HAZ as approximate function of peak temperature during welding (Cerjak 2008).

The majority of premature failures which have occurred on all types of high temperature plant have been at weldments. The reason this failures occurred is that, at the time of the original design, virtually no weldment property data were available and therefore almost all designs were based on parent material properties. Unfortunately, weldment properties for many materials can be so reduced relative to parent properties that they are not accommodated by the engineering safety factor and failures eventually ensue. Weldment behaviour has however been the subject of extensive global research over the last two decades and most of the features responsible for the various characteristic failure modes have been identified and new procedures devised which eliminate or minimise the weakness (Middleton 1996).

The following section gives a short summary of weldment failure modes in ferritic steels which also serve to illustrate the general problem existing in many other high temperature material weldments:

The properties of ferritic weldments are generally determined by those of the heat affected zone (HAZ) and/or those of the weld metal. Interface failures do occasionally occur but are relatively rare, excepting dissimilar metal joints and renormalised seam welds. Integrity problems

associated with both heat-affected zones and weld metals arise from a combination of two characteristics of ferritic (body centred cubic) steels (Middleton 1996):

i. The ability to transform to austenite (face centred cubic) above 800°C- 900°C with the associated dissolution of carbides and destruction of the ferritic grain boundary network. Succeeding cooling to ambient temperature reverses the process leading to precipitation of a new dispersion of creep strengthening carbides and the formation of a new grain boundary network.

ii. The dependence of creep strength and creep rupture life on the peak austenitising temperature. Fine grained material at the extremities of the HAZ typically exhibits a rupture life reduced by more than an order of magnitude relative to the coarse grained material adjacent to the fusion interface.

The distribution of microstructures throughout a ferritic weldment generated by these characteristics determines the mechanical properties, and especially toughness, high temperature creep strength and ductility (Masuyama 2000).

The cracking of welded joints is usually classified according to the position of the crack. Type I and Type II modes occur within the weld metal, the former confined to the weld metal whereas the latter may grow out of the weld into the HAZ as shown in Figure 12. Type III cracking occurs in the coarse grained region of the HAZ. Type IV is a pernicious form of cracking where there is an enhanced rate of creep void formation in the fine grained and intercritically annealed HAZ of the weld, leading to early failure when compared to the unwelded material (Masuyama 2000).

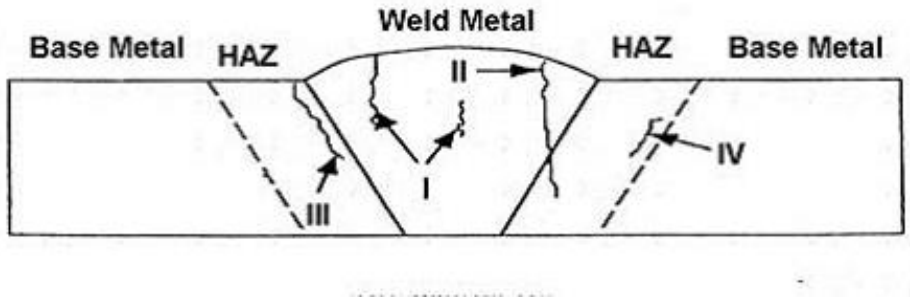

Figure 12: Classification of cracks in a weld joint (Schuller 1974).

A substantial decrease in the creep life of welded joints is caused by Type IV cracking, which refers to premature failure of welded joints due to an enhanced rate of creep voids formation in the FGHAZ (Francis 2006).

The fine grained heat-affected zone exhibits much higher secondary creep rate and shorter creep rupture time compared with the base material (BM). This indicates that remarkable drop in creep properties occurs in the FGHAZ (Mannan 1999).

The structure in the FGHAZ was reported to have large spheroidized $M_{23}C_6$ carbides on grain boundaries larger than the ones in the BM. The interparticle spacing is reported to be large and the dislocation density is lower in the FGHAZ compared to the BM (Tian 1991; Xue 2009). Small grains increase the effective diffusion coefficient of the material and therefore enhance creep.

Spheroidized carbides in the FGHAZ results due to welding temperature cycle experienced by this part of the HAZ. For X20CrMoV12-1 material, the $\alpha \rightarrow \gamma$ transformation start at about 820ºC and finishes at 950ºC. For complete dissolution of the $M_{23}C_6$ carbides, however, an austenitizing temperature of 1020ºC – 1050ºC is required (Laha 2007). Therefore, a certain amount of $M_{23}C_6$ carbides remain undissolved in the matrix of the part of the HAZ which undergoes a welding thermal cycle of 820ºC – 1000ºC, and coarsen in that temperature range (Barraclough 1985).

The partial dissolution of $M_{23}C_6$ in the FGHAZ is claimed to promote Z-phase formation in some 9-12%Cr steels, which in turn destabilizes MX precipitates. The deterioration of creep properties thus becomes localized to Type IV region (Masuyama 2000; Sawada 2008) . In steels with higher Cr contents, the formation of Z-phase is accelerated even in the FGHAZ of welded joints (Sawada 2008).

The stress triaxiality and maximum principle stress located at the FGHAZ are reported to be higher than that of other zones in the weld joint during creep. It implies that they can accelerate the creep strain development and creep damage accumulation; as a result Type IV cracking is likely to occur in this zone (Spigarelli 2002; Hongyang 2010).

Increases in the weld preheat and interpass temperature was reported to significantly improve Type IV limited rupture life. Although there may be some benefit associated with using a higher

heat input, it was concluded that any effect of heat input on the tendency for Type IV failure is small (Francis 2006; Francis 2009).

2.5. The Back-Stress Concept

If an external force is acting on a microstructure, part of the external driving pressure σ_{ex} is counteracted by heterogeneous internal microstructure constituents such as precipitates and interfaces. Consequently, not all the external load can be assumed to represent the driving force for creep deformation. Only that part of the external stress σ_{ex} which exceeds the amount of the inner stress σ_i from the counteracting microstructure effectively contributes to the deformation process. Since the inner stress reduces the effect of the external stress, this inner stress is commonly denoted as back-stress and the approach is known as the back-stress concept. Thus, the effective creep stress σ_{eff} can be expressed as (Aghajani 2009; Holzer 2010):

$$\sigma_{eff} = \sigma_{ex} - \sigma_i \quad \text{...Equation 3}$$

With the inner stress, the general Norton creep law can be rewritten as (Aghajani 2009; Holzer 2010):

$$\dot{\varepsilon} = A_1 \exp\left(-\frac{Q}{RT}\right) * (\sigma_{ex} - \sigma_i)^n = A(\sigma_{eff})^n \quad \text{...Equation 4}$$

where:

Q – is activation energy (J),

R – gas constant (8.314J/mol.K),

T – temperature in K, and

A_1 and n are constants.

The inner stress can be expressed as a superposition of individual contributions from the immobile dislocations and precipitates. When the contribution from the subgrain boundaries is also taken into account, the inner stress can be expressed as (Aghajani 2009; Holzer 2010):

$$\sigma_i = M\tau_i = M\left(\sigma_{disl} + \sigma_{sg} + \sigma_{prec}\right) \quad \text{...Equation 5}$$

where M is the Taylor factor (usually between 2 and 3). The subscripts in the terms in the parentheses denote contributions from dislocations, subgrain boundaries, and precipitates respectively.

When examining the individual contributions of the different mechanisms to the back-stress, the part stemming from dislocations can be expressed as (Aghajani 2009; Holzer 2010)

$$\sigma_{disl} = \alpha G b \sqrt{\rho_n} \text{ ...Equation 6}$$

Where ρ_n denotes the density of mobile dislocations and α is a constant (ranges between 0.84 and 1). G is the shear modulus and b is the Burgers vector.

The sub-boundary hardening given by (Aghajani 2009; Holzer 2010):

$$\sigma_{sg} = \frac{10Gb}{\lambda_{sg}} \text{ ...Equation 7}$$

where λ_{sg} is the short width of elongated subgrains.

The contribution of precipitates to the total back-stress can be described by critical Orowan stress. If the precipitates are sufficiently hard, such that dislocations cannot bypass them by cutting, the upper limit of the pinning force is determined by the Orowan stress. The Orowan back-stress can be calculated as follows (Aghajani 2009; Holzer 2010):

$$\sigma_{or} = \frac{\alpha.M.G.b}{\lambda} \text{ ...Equation 8}$$

This quantity denotes the maximum back-stress caused by a random distribution of precipitates using the mean distance λ between the precipitate (Aghajani 2009; Holzer 2010). The mean distance λ between the precipitate can be calculated as follows (Sonderegger 2011):

$$\lambda = \sqrt{\frac{\ln(3)}{2\pi \sum_i n_{V,i}} + (2r_A)^2} - 2r_A \text{ ...Equation 9}$$

For i size classes, r_i denotes the radii and $n_{V,i}$ denotes the number densities. The mean projected radius r_A can be calculated as mean value of all projected radii, weighed by the probability that the corresponding precipitates intersect the glide plane (Sonderegger 2011).

$$r_A = \sqrt{\frac{2}{3}} \frac{\sum_i n_{V,i} . r_i^2}{\sum_i n_{V,i} . r_i} \text{ ...Equation 10}$$

The precipitates parameters (radii, number density and volume fraction) cannot be observed directly in the Transmission electron microscopy (TEM) Energy Dispersive X-ray (EDX) maps but have to be evaluated using stereological methods. New stereological methods produce significantly lower deviations and their systematic errors can be assessed. The precipitate diameter is calculated as follows (Sonderegger 2006):

$$d_i = \frac{2}{\pi}\left(d_{m,i} - t_i\right) + \sqrt{\frac{2}{\pi}(d_{m,i} - t_i)^2 + \frac{4 d_{m,i} t_i}{\pi}} \quad \text{...Equation 11}$$

$d_{m,i}$- measured diameter of precipitate i,

t_i- sample thickness at position of precipitate i.

The weighed mean diameter can be calculated as follows (Sonderegger 2006):

$$\bar{d} = \frac{\sum_i d_i w_{Sample,i}}{\sum_i w_{Sample,i}} \quad \text{...Equation 12}$$

The weight for each precipitate $w_{Sample,i}$ is the probability to find its centre in the sample volume and it is calculated as follows (Sonderegger 2006):

$$w_{Sample,i} = \frac{t_i}{t_i + d_i} \quad \text{...Equation 13}$$

The phase fraction and the number density are calculated as follows, respectively(Sonderegger 2006):

$$f_V = \frac{1}{V_{Sample}} \sum_i \frac{d_i^3}{6} \frac{t_i}{t_i + d_i} \quad \text{...Equation 14}$$

V_{Sample} – volume of the sample

$$n_V = \frac{1}{A_{Sample}} \sum_{i=1..N_A} \frac{1}{t_i + d_{mi}} \quad \text{...Equation 15}$$

A_{Sample} – area of the sample.

2.6. X20CrMoV12-1 Steel

The grade X20CrMoV12-1 steel is established based on the corrosion-resistant 13%Cr high temperature steels containing up to 0.25%C in tempered condition (EPRI 2006). These high-temperature steels were used in structures as early as the 1920s for turbine blades and corrosion-

resistant machine elements (Kauhausen 1957). However, due to the problems associated with weldability, material development concentrated on austenitic steels (EPRI 2006).

The breakthrough in welding of X20CrMoV12-1 in engineering crack-free welds facilitated its application in boilers and turbine piping with steam temperature at 560°C and service pressure of 21.28MPa as early as 1959 (Baumann 1968; Schinn 1969). The 12CrMoV steels were standardized for use in steam pipes under the DIN designation X20CrMoV12-1, known as X20 (EPRI 2006).

The first application of X20 steel in steam plants dates back to 1963. High creep strength of the steel allowed construction of larger power plants in Germany with more advanced steam parameters. The high thermal fatigue resistance of the X20 steel enabled components with good cyclic properties in plant operations (Klueh 2001). This alloy has been very successful during long-term service for tubes and pipes at a temperature of 565°C (EPRI 2006).

Grade X20CrMoV12-1 can be used for components in power generation, and chemical plants. These include superheater and reheater tubes, main-steam pipes, turbine cases and blades and other high-temperature services where high creep strength, corrosion, and oxidation resistance are desired (EPRI 2006).

The chemical composition of X20 steels is shown in Table 3 for different standards.

Table 3: Chemical Requirements of X20 steel (Kalwa 1978).

Standard	Designation	Chemical composition (wt %)								
		C	Si	Mn	P	S	Cr	Mo	Ni	V
DIN 17175	X20CrMoV12-1	0.17 0.23	≤0.50	≤1.00	≤0.030	≤0.030	10 12.50	0.80 1.20	0.30 0.80	0.25 0.35
ISO 9327	X20CrMoV11-1	0.17 0.23	≤0.04	0.30 1.00	≤0.035	≤0.030	10 12.50	0.80 1.20	0.30 0.80	0.25 0.35
EN10222-2	X20CrMoV11-1	0.17 0.23	≤0.04	0.30 1.00	≤0.025	≤0.015	10 12.50	0.80 1.20	0.30 0.80	0.25 0.35

The mechanical, creep and fracture properties of X20 steels are highly dependent on the microstructure, which in turn is influenced by the chemical composition, casting, and cooling processes. It may be further improved by heat treatment and thermo-mechanical treatment of cast and/or wrought structure (EPRI 2006).

Material engineering properties are determined using standard testing methods to obtain information about component design and service behavior. Table 4 shows mechanical and fracture properties for X20 steels.

Table 4: Room Temperature Mechanical and Fracture Properties of X20 steel (ECCC 2005).

Standard	Designation	Mechanical properties						
		Thickness (mm)	Yield stress (MPa)	Tensile strength (MPa)	Fracture elongation (%)		Charpy impact energy (J)	
					L	T	L	T
DIN 17175	X20CrMoV12-1	≥16,≤60	490	690-840	≥17	≥14	≥48	≥34
EN10222-2	X20CrMoV11-1	≤100	500	700-850	≥16	≥16	≥39	≥27
		>100,≤200					≥31	≥27
		>250,≤300				≥14	≥27	≥24
ISO 9329-2		≤100	490	700-850	≥16	≥14	≥39	≥27
		>100,≤200					≥31	
		>250,≤300					≥27	

The microstructure evolution can be determined following continuous cooling transformation (CCT) diagrams. The microstructure of the material depends on composition and heat treatment history. Slower cooling rates, which are nearer to equilibrium, typically results in the formation of ferrite, whereas bainite or martensite is formed under more rapid cooling conditions. Fast cooling rates are typically associated with welding process, in particular weld metal and HAZ (EPRI 2006).

The CCT curves can be used to develop required microstructures through control of the applied thermal cycles for a number of different manufacturing processes. It is important that the thermal cycle used to produce the CCT curve is relevant to the particular process. A CCT diagram of X20 steel is shown in Figure 13.

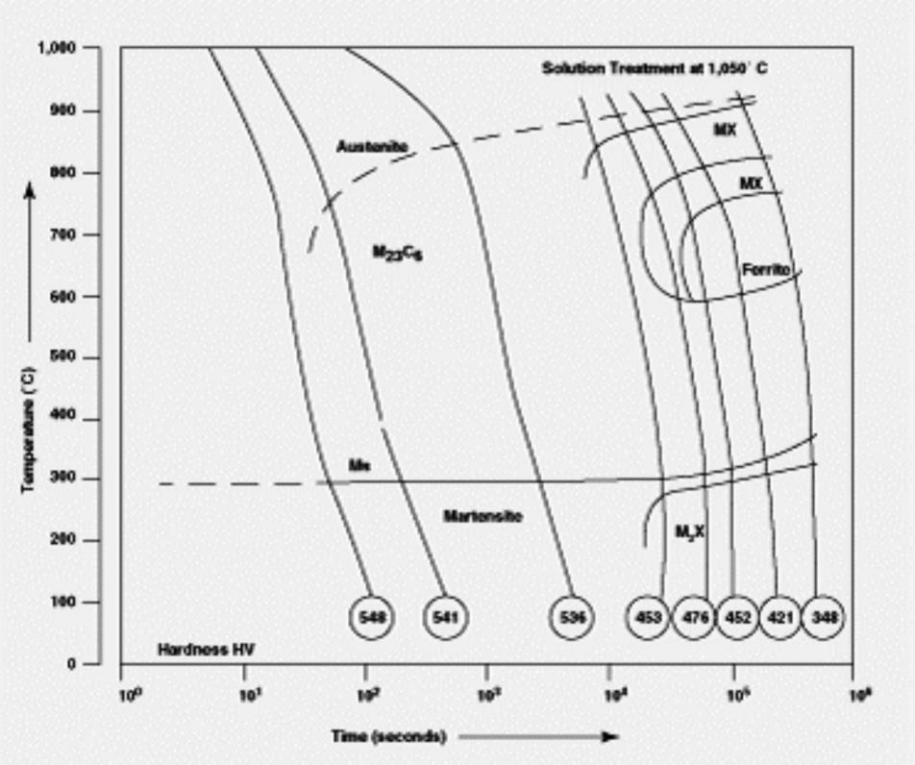

Figure 13: CCT diagram for X20CrMoV12-1 steel.

3. Materials and Experimental Methods

3.1. Materials

Ex-service (creep aged) X20 steels and virgin X20 steel pipework were obtained from Eskom Sustainability Division for research. The service exposed samples were chosen in terms of creep damage measured on the surface of the pipework using surface replication technique (please refer to section 3.4 for details on the method). The samples used for research were identified as follows: New X20 (virgin X20 steel), X20_210_540 (service exposed X20 steel) and X20_130_555 (service exposed X20 steel).

The operating data for service exposed pipework is shown on Table 5. High service temperatures were reported for X20_130_555. X20_210_540 had relatively high operating hours and had operated below the design temperature.

Table 5: Operating data for service exposed samples.

Sample ID.	*Operating Temp. (˚C)*	*Operating Press. (MPa)*	*Design Temp. (˚C)*	*Design Press. (MPa)*	*Operating hrs*
X20_210_540	540	17.5	545	19.4	208302
X20_130_555	555	17.5	545	19.4	129801

The pipework used to undertake the research had an internal diameter (ID) of 255mm±5mm and wall thickness (WT) of 35mm±1mm as shown Figure 14.

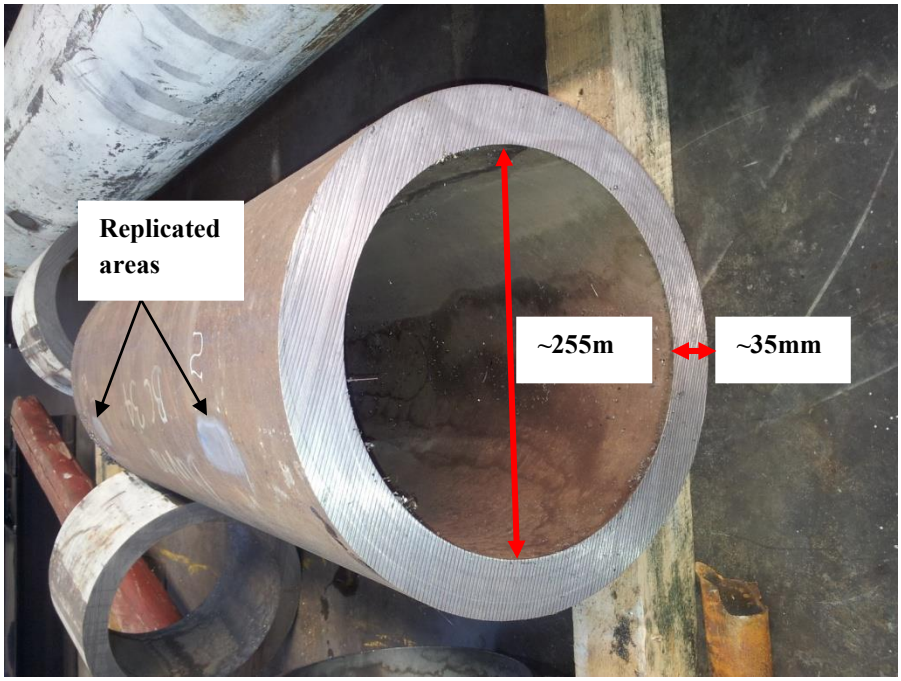

Figure 14: X20 pipework used for research.

One sample was sectioned from each pipework and sent to Scrooby's Laboratory Service Close Cooperation for chemical analysis. Table **6** shows the required chemical composition for DIN 17175 Grade X20CrMoV12-1 and the chemical analysis results for the research samples. The research samples had chemical composition within the specification range of X20CrMoV12-1.

Table 6: Chemical analysis results (in weight %) for the X20 samples used for research.

Element	*X20CrMoV12-1 (DIN 17175)*	*New X20*	*X20_210_540*	*X20_130_555*
C	0.17 - 0.23	0.19	0.21	0.2
Mn	≤1.00	0.35	0.41	0.46
S	≤0.030	≤0.005	≤0.005	≤0.005
P	≤0.030	0.012	0.006	0.015
Si	≤0.50	0.15	0.31	0.31
Cr	10.00 – 12.50	10	10.8	11.1
Mo	0.80 – 1.2	0.86	0.84	0.88
Ni	0.30 – 0.80	0.48	0.52	0.50
Cu		0.12	0.11	0.14
Al		0.025	0.036	0.038
V		0.24	0.28	0.26
Nb		≤0.005	≤0.005	≤0.005
Ti		≤0.005	≤0.005	≤0.005
B		≤0.001	≤0.001	≤0.001
W		≤0.005	≤0.005	≤0.005
Sn		≤0.002	≤0.002	≤0.002
As		0.0096	0.0086	0.0157
Sb		≤0.005	≤0.005	≤0.005
N		676ppm	530ppm	547ppm
Fe	Matrix	Matrix	Matrix	Matrix

High silicon content was noted on service exposed X20 steels relative to the New X20. Laves phase contains approximately 5% Si. Si therefore promotes the formation of Laves phase.

Creep aged X20 pipework (X20_210_540 and X20_130_555) was welded to X20 pipework with virgin X20 pipework (New X20), and these were used for X20 welding procedure qualification (see sectioned 3.2 for detailed information). Figure 15 shows a typical macro image taken on the X20 steel weld-joint.

Figure 15: Typical macro image of X20 steel weld-joint indicating that the weld-joint was sound.

The welded X20 pipework was sectioned into samples easy to handle during laboratory preparation; these samples consisted of the BM, HAZ and WM as shown in Figure 16. Two samples were sectioned from each weldment and used for hardness testing and metallographic analysis.

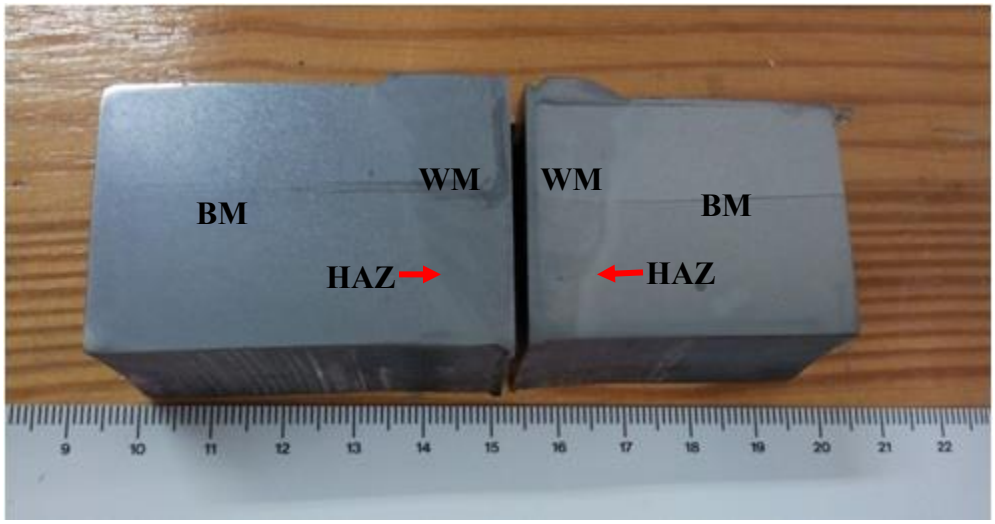

Figure 16: X20 samples sectioned from the weldments. The samples consisted of the BM, HAZ and WM. The HAZ of a weldment is only few millimetres.

As shown in Figure 16, the HAZ of a weldment is only few millimeters and gradients of microstructures exist within this small volume. This restricts the study of important mechanical properties in individual regions of the HAZ. HAZ simulation has been used recently to study the effect of welding on mechanical properties in the HAZ (Adonyi 2006). This process was used to mimic the welding process in order to study to study mechanical properties of interest in X20 steel HAZ (please refer to section 3.3. for detailed information).

Research samples were used to characterize the evolution of mechanical properties and microstructure after the welding process. The evolution of property was characterized using hardness testing, tensile testing and creep testing. Microstructural evolution was characterized using light microscopy, scanning electron microscopy and transmission electron microscopy.

3.2. Welding Procedure

Welding procedure qualification was conducted using New X20, X20_210_540 and X20_130_555. The welding procedure qualification was done in accordance to the American Society of Mechanical Engineers IX (ASMEIX) Qualification Standard for Welding and Brazing Procedures, Welders, Brazers, and Welding and Brazing Operators (ASME 2008).

12Cr-1Mo-0.025V-0.4W filler metal was used to prepare New X20 – X20_210_540 weld-joint (WJ) and New X20 – X20_130_555 WJ. Preheat/interpass temperature of 200˚C/250˚C and a maximum heat input of 1.9kJ/mm was used for the welding process. Tungsten Inert Gas (TIG) (for root and hot pass) and Manual Metal Arc (MMA) welding processes were used to weld the X20 steel pipework using Bohler 20MVW-IG and Bohler Fox 20MVN filler materials respectively.

Post-weld heat-treatment (PWHT) of the weld joints was done using parameters stipulated by Eskom. Annealing of the weldments is typical done at temperatures of 720 – 780°C. Holding time at the temperature depends on the thickness of the work piece. The recommended minimum holding time for a component thickness <15mm is 15 minutes, for thickness <15mm to <30mm is 30 minutes, for the thickness >30mm is 60 minutes. Welding is followed by cooling below 150°C, whereas thick-walled tubes should not be cooled below 100°C prior to PWHT (EPRI 2006).

Non-destructive testing (NDT) and destructive testing (tensile tests, guided-bend tests, notch-toughness tests etc.) were conducted after welding in accordance to ASMEIX (ASME 2008). Destructive tests were conducted by MATLAB laboratories.

Welding process results in formation of narrow transformed region (HAZ) adjacent the fusion zone. Studying the change in microstructure mechanical properties in this region is difficult as the region is only few millimeters. Detailed study of the change in microstructure and mechanical properties can be done by physical simulation of individual HAZ regions.

3.3. Heat affected Zone Simulations

Actual HAZ present a complex mix of microstructures within a small volume next to the fusion zone. Temperature gradients are so large that microstructure can be found within tenths of millimeter. Therefore, the property of one single microstructure that has the worst properties becomes difficult to measure. Physical simulation of the HAZ microstructure is required to effectively study the change in mechanical properties during welding. Gleeble thermo-mechanical simulator provides the technology required to mimic the welding process (Adonyi 2006).

A typical arc weld thermal cycle consists of very rapid heating (several hundreds of degrees per second) to a peak temperature, followed by relatively fast cooling (a few tens or hundreds of degrees per second) to ambient temperature. The microstructural changes in the weld zone, as well as the heat-affected zone, are greatly dependent on the heating and cooling rates, which in turn depend on the weld heat input, the plate thickness/geometry and the initial or interpass temperature. The microstructural changes will directly affect the property changes in the weld zone and the HAZ. Therefore, it is important to be able to predict the actual thermal cycle characteristics such as peak temperature and cooling rate if microstructure is to be characterized and correlation with property is sought. The most widely used and the best known analytical solutions to predict thermal history and cooling rate are those of Rosenthal (Poorhaydari 2005).

The solutions give the temperature variation during cooling as a function of time for a given location, the peak temperature (T_P) as a function of distance from the heat source, and the weld time constant ($\Delta t_{8\text{-}5}$), which is the cooling time from 800 to 500°C (Poorhaydari 2005). The cooling time is calculated as follows:

$$\Delta t_{8-5} = \frac{q/v}{2\pi\lambda\theta_1} \quad \text{...Equation 16}$$

$$\theta_1 = \frac{1}{500-T_0} - \frac{1}{800-T_0} \quad \text{...Equation 17}$$

$$\frac{q}{v} = \frac{EI\eta}{v} \quad \text{...Equation 18}$$

T – Temperature, °C

T_P – Peak temperature, °C

t – Time, s

$\Delta t_{8\text{-}5}$ – Cooling time from 800°C to 500°C, s

T_0 – Initial temperature, °C

λ – Thermal conductivity, $Js^{-1}m^{-1}°C^{-1}$

q – Arc power, J/s

v – Travel speed, m/s

q/v – Heat input, J/m

E – Voltage, V

I – Current, A

η – Thermal efficiency (<1)

Note the unique characteristic of cooling rate is that it is independent of the distance from the heat source, at least in the HAZ. This fact has also been confirmed by numerical analysis as well as experiments where it was found that the cooling rate is only dependent on the heat input, plate thickness/geometry, and the plate initial temperature (Hess ; Zhang 2004).

The mean cooling rate for the temperature range 800°C to 500°C is calculated in °C/s from a simple equation:

$$T'_{800-500} = \frac{300}{\Delta t_{8-5}} \text{ ...Equation 19}$$

The data from the welding procedure qualification was used to calculate the parameters required. The cooling time and cooling rate from 800°C to 500°C was calculated to be 8.3s and 36°C/s, respectively.

The cooling rate, initial temperature and peak temperature experienced in each HAZ zone were used to simulate the FGHAZ and the CGHAZ. The preheat temperature and peak temperatures were obtained from literature (Barraclough 1985; Middleton 1996; EPRI 2006). Three thermal cycles were used to mimic the conditions of a multi-pass weld HAZ. Table 7, Table 8, Figure 17 and Figure 18 show the data used to simulate the FGHAZ and CGHAZ.

The peak temperatures used for HAZ simulation were according to the predicted temperature for the FGHAZ and CGHAZ. The peak temperatures were reduced by 50°C from the previous peak temperature, but the temperatures were kept within each region of interest. A preload of 300kN was applied during simulation and this was done to induce the constraint effect of a real weld. During welding, tensile residual stresses are introduced due this constraint effect.

Table 7: Multiple thermal cycles used to simulate the FGHAZ.

Initial Temperature (ºC)	Peak Temperature (ºC)	Final Temperature (°C)	Heating rate (ºC/s)	Cooling rate (ºC/s)
250	950	250	200	36
250	900	250	200	36
250	850	100	200	36

Table 8: Multiple thermal cycles used to simulate the CGHAZ.

Initial Temperature (ºC)	Peak Temperature (ºC)	Final Temperature (°C)	Heating rate (ºC/s)	Cooling rate (ºC/s)
250	1150	250	200	36
250	1100	250	200	36
250	1050	100	200	36

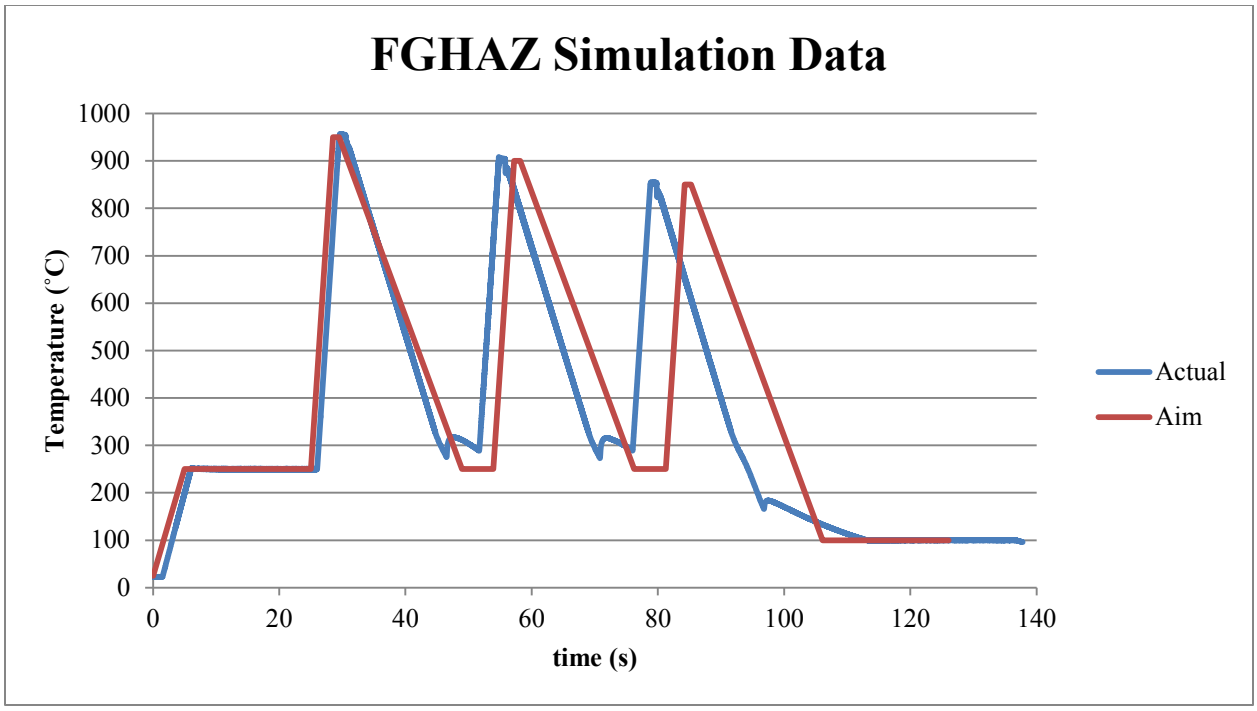

Figure 17: **Thermal cycles used to simulate the FGHAZ of New X20, X20_210_540 and X20_130_555. The heating rate of 200°C/s and cooling rate of 36°C/s were used for the FGHAZ simulation.**

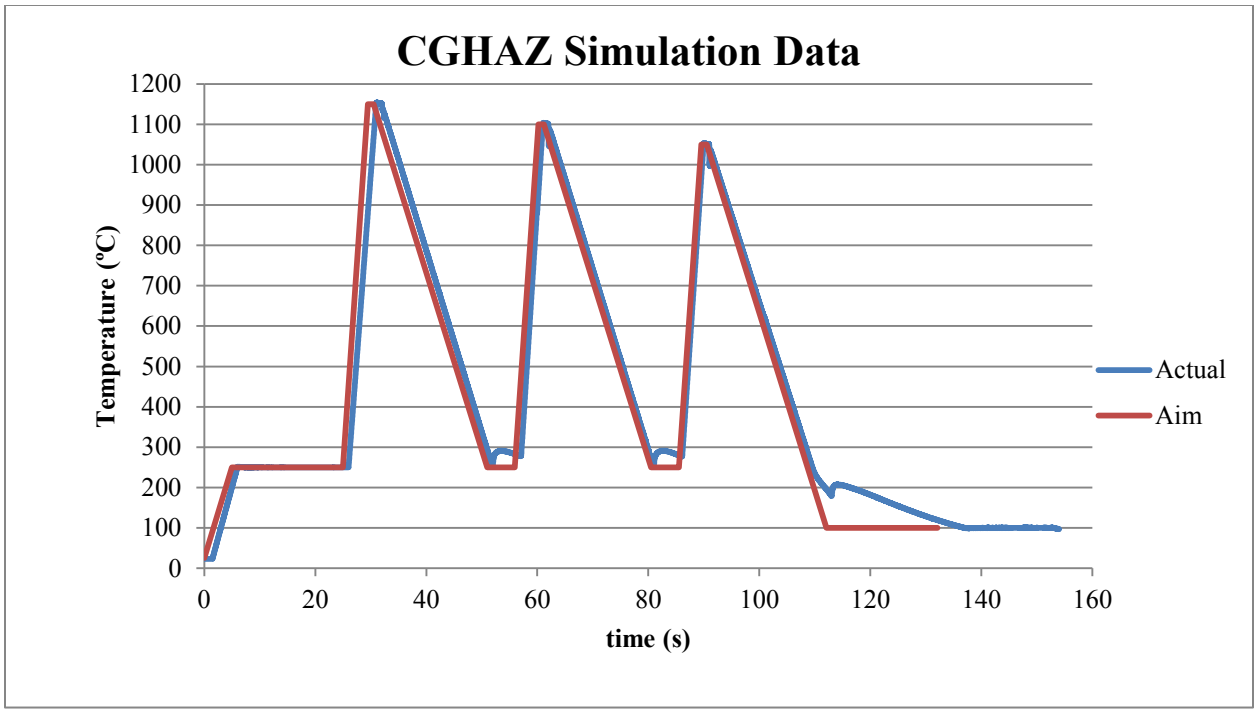

Figure 18: Thermal cycles used to simulate the CGHAZ New X20, X20_210_540 and X20_130_555. The CGHAZ was simulated using a heating rate of 200°C/s and a cooling rate of 36°C/s.

Twelve 100mm long specimens with a diameter of 6mm (see Figure 19) were machined from New X20, X20_210_540 and X20_130_555 bulk material. Four CGHAZ and four FGHAZ simulations were conducted using these samples. The HAZ simulations were conducted using Gleeble 3800.

Figure 19: Simulated HAZ specimens (length ~ 100mm, diameter = 6mm).

Simulated HAZ specimens were heat-treated following X20 heat-treatment procedure shown in Table 9. Two simulated FGHAZ specimens and two simulated CGHAZ specimens (from each batch) were used for tensile testing and the rest of the simulated HAZ specimens were used for microstructural analysis and hardness testing.

Table 9: Heat-treatment parameters used for X20 simulated HAZ specimens (EPRI 2006).

Initial Temperature (°C)	Peak Temperature (°C)	Heating rate (°C/h)	Hold time (min)	Cooling rate (°C/h)	Final Temperature (°C)
25	730	100	30	100	25

3.4. Mechanical Testing

3.4.1. Hardness Testing

Samples sectioned from X20 weldments and simulated HAZ specimens were prepared following standard procedure for ferrous alloys. The samples were ground using a silicon carbide paper (80, 120, 240,500, 800 and 1000 grit size) and polished using 3µ and 1µ diamond paste. The samples were then etched using Villela's Reagent (1gram picric acid, 5ml hydrochloric acid and 100ml ethanol).

Hardness tests were carried out on the prepared samples using EMCO TEST DURASCAN Vickers hardness testing machine. Hardness profiles were obtained across the weldments (1mm intervals across the WJ X 3 rows) and simulated HAZ specimens using a load of 3kgF.

The hardness tests were performed using CSM Nano-indentation tester applying a load of 300mN to identify different regions of the HAZ. The hardness trends were used as markers for SEM analysis and TEM sample extraction using Focused ion beam (FIB) equipment.

3.4.2. High Temperature Tensile Testing

Simulated HAZ specimens were used to conduct tensile tests using the Gleeble 3800 thermo-mechanical apparatus. The samples were cleaned using silicon carbide paper (1000 grit size) after heat-treatment and the diameter of the samples was then measured using the Vernier Caliper. Type-K thermocouples were attached on the specimens using the Dynamic System Inc Thermocouple Welder. Spot-welded samples were loaded into Gleeble 3800 and then heated up to 545°C within 30seconds. The samples were held at this temperature for 20seconds and then deformed at a strain rate of $10^{-2}s^{-1}$ at this temperature.

3.4.3. Creep Testing

Cross-weld creep specimens were machined following the European Creep Collaborative Committee (ECCC) recommendations (ECCC 2004). The cross-weld creep specimen dimensions were chosen to represent all regions of the weldment (BM, HAZ and WM). Figure 20 shows dimensions of the specimens used for creep rupture tests. Creep rupture tests were conducted at 650˚C, applying a reference stress of 63MPa. Two identical specimens were machined from New

X20-X20_210_540 weldment and New X20-X20_130_555 weldment and used to conduct creep tests at similar conditions.

The reference stress was calculated using the modified Von Mises equation (Van-Zyl 1997):

$$\sigma_R = P\frac{\sqrt{3}}{2}[ln\frac{R_o}{R_i}]^{-1} \text{ ...Equation 20}$$

where:

P – operating pressure

R_o – outer radius

R_i – inner radius

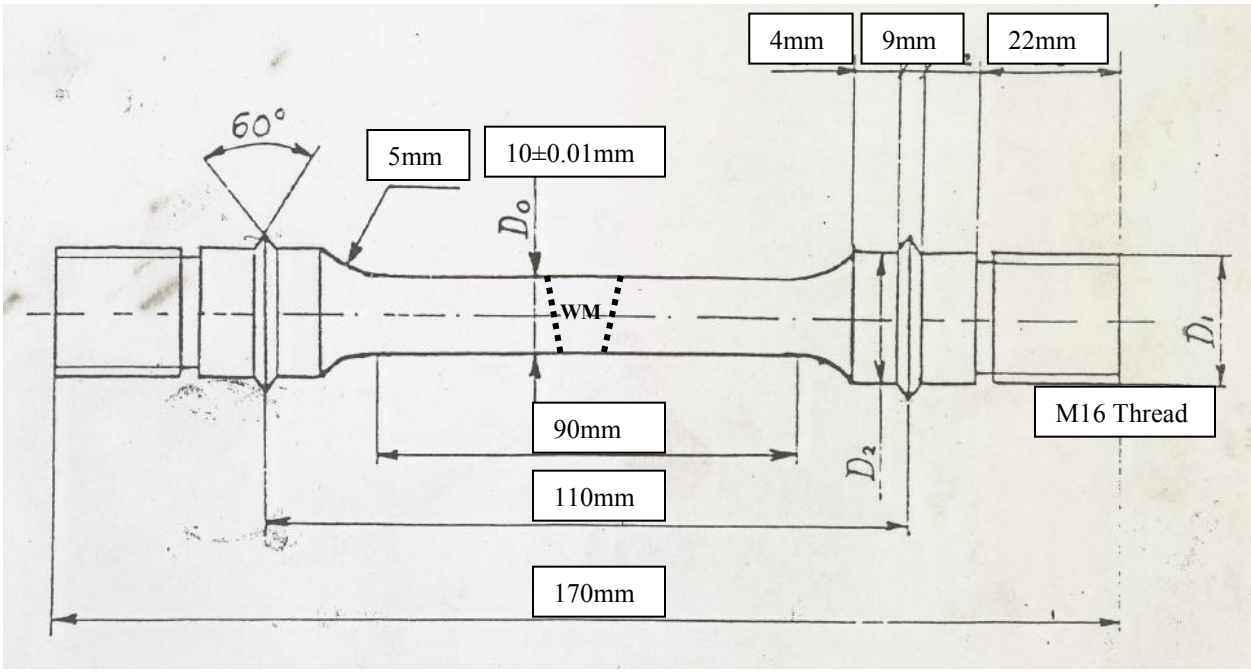

Figure 20: Cross-weld creep specimen dimensions.

3.5. Surface Replication Technique and Life Estimates

Surface replication technique is a well-developed microscopy technique that can be used to conduct in situ measurements of microstructure of components. The in situ determination of microstructural deterioration and damage of materials subjected to various environments can be conducted. The need to assess the condition of the power plant and petrochemical metallic components led to the application of surface replication to address the problem of determining remaining life. The usual method of metallographic investigation, which may involve cutting large pieces from the component so that laboratory preparation and examination can be performed, usually renders the component unfit for service or necessitates costly repair. As a result, metallographic investigations are avoided, and important microstructural information is not available for evaluating the component for satisfactory performance. Therefore, an in situ or field microscopy examination is needed to aid in the proper determination of component life (Marder 1989).

The replication technique for examination of surfaces has been extensively used for studying the structure of polished and etched specimens. Component in service usually have a well-developed corrosion or oxidation product or decarburized layer on the surface that must be removed prior replication. Coarse grinding equipment can be used as long as the proper precautions are taken to prevent an introduction of artifacts into the structure due to overheating or plastic deformation. Sandblasting, wire wheels, flap wheels, and abrasive disks can be used. After initial preparation steps are completed, standard mechanical polishing techniques can be used. Various silicon carbide abrasive disks of different grit size, together with polishing cloth disks with diamond paste or alumina of varying grit size, are used to prepare for the etching step. Finally, an appropriate etchant for the material being examined is applied to develop the microstructure. For the proper identification of such microstructural features as creep cavities, a maximum double or triple etch-polish-etch procedure should be used (for details, please see reference (Marder 1989)).

Surface replicas provide an image of the topography of a specimen which is subsequently examined in the microscope. The technique uses plastic, or oxide replica material. All direct methods except plastic methods are destructive and therefore require further preparation of the specimen before making addition replicas. Plastic replicas lend themselves to in-plant non-

destructive examination because of their relative simplicity and short preparation time. Plastic replicas can be examined with light optical microscope, scanning electron microscope, and transmission electron microscope, depending on the resolution required. As illustrated in Figure 21, the plastic replica technique involves softening a plastic film in a solvent, applying it to the surface, and then allowing it to harden as the solvent evaporates. After careful removal from the surface, the plastic film contains a negative image, or replica, of the microstructure that can be directly examined in the light microscope, or, after some preparation, in the electron microscope. Double-faced tape is used to bond the replica to the glass slide in order to obtain large, flat, undistorted replica surfaces (Marder 1989).

Creep defects cause the majority of failure in the power plant components operating under stress and thermal load, and the replica method is especially suitable for the detection of these defects. Therefore, the replica method has become an especially important tool in the determination of remaining life in such components as boiler tubes, steam piping, and turbine components. The replica method reveals defects due to creep at much earlier stage than other NDE techniques. Creep defects begin as small holes or cavities at grain boundary or second phases. With time and stress, these cavities can link up to form cracks that eventually lead to failure of the component as shown in Figure 22 (Marder 1989).

Metallographic surface replication is used extensively by Eskom for the quantitative 'non-destructive' assessment of creep damage and other damage of high temperature components. The scope depends on the condition and age of plant, previous inspection records and future requirements with respect to life, operating mode, maintenance, outages, economics and development of new assessment technologies (Van-Zyl 2000).

Damage models are based on metallographic micro void damage as evident under the optical microscope at a magnification of 400X or 500X. Voids are counted and expressed as number of voids per square millimeter. The damage model used is shown in equation below (Van-Zyl 1997):

$$\frac{t}{t_r} = 1 - (1 - \frac{N}{N_f})^{\lambda} \quad \text{...Equation 21}$$

where:

t – exposure time (h)

t_r – rupture time (h)

N – number of voids.mm^{-2}

N_f – number of voids.mm^{-2} at fracture

λ – material creep ductility parameter.

In the model N_f is usually limited to 1000 voids.mm^{-2} but in practice it could evolve to a few thousand voids.mm^{-2} before micro crack formation and crack development occur in a component (Van-Zyl 1997).

Numerous small sub-microscopic creep voids with diameters less than 0.1µ initiate as early as 10 percent of the creep rupture life of a material. Some of these voids will grow and become visible under an optical microscope at a magnification of 500X when they have grown to a size of 1µ (± 0.5µ). The latter will happen typically for low alloy and 12CrMoV steels where the strain rate is less than $10^{-6}h^{-1}$ at life fractions consumed between 0.2 and 0.5 (Van-Zyl 2005).

During the secondary creep stage the contribution of sub-microscopic voids are insignificant with respect to the strain due to their small volume contribution and this is in sharp contrast with those visible at 500X which increases slowly in number and size (Van-Zyl 2005).

Finally in the tertiary stage the number of voids visible at 500X hardly increases but their size increases rapidly (Van-Zyl 2005).

These are the observations made from metallographic replica taken from components in Eskom plant and post exposure laboratory creep tests that dates back over a period of more than two decades (Van-Zyl 2005).

During the secondary creep stage and where the creep strain rate is less than 10-6h-1 only approximately five percent of the strain can be explained as due to the volume created by void growth and this is mostly due to the number of voids moving into the 500X visible window. The assumption that the strain rate is directly proportional to the void formation rate is a fair one (Van-Zyl 2005).

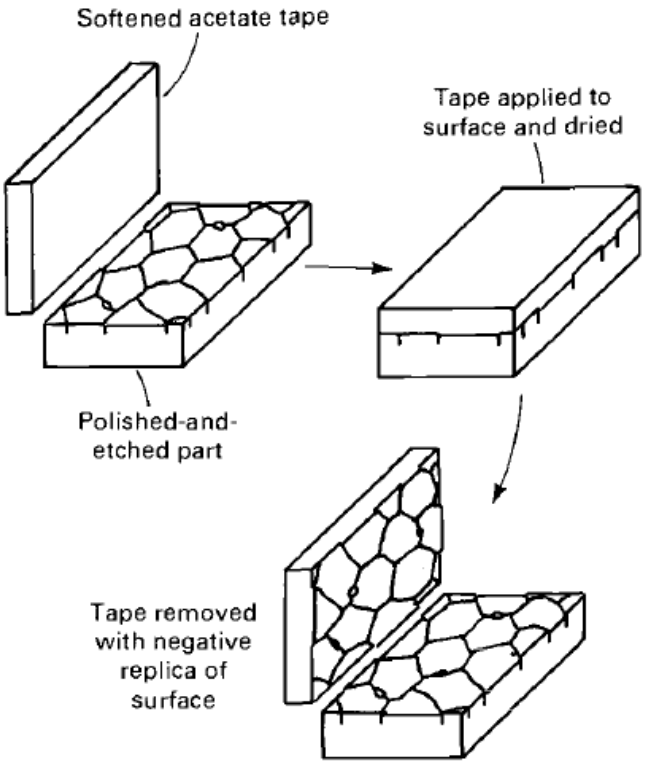

Figure 21: Schematic illustration of the plastic replication technique (Marder 1989).

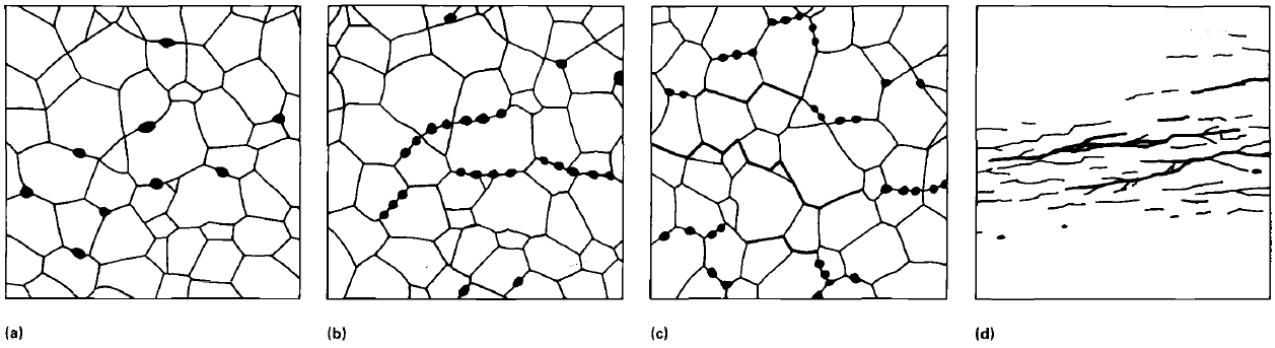

Figure 22: Schematic of creep crack formation. (a) Small cavities, (b) link up over time, (c) form intergranular cracks and (d) eventually macrocracks (Marder 1989).

Creep void density measurements were carried out on the service exposed pipework following Eskom replication procedure. The X20 pipework was ground using silicon carbide paper (80, 120, 240, 500, 800, and 1000 grit size), polished using 1µ diamond paste and etched using

Villela's reagent. Metallographic replicas were taken on eight positions from each pipe sample at two times four equally spread circumferential positions, ~180mm apart from each other in the axial direction. The replicas were initially analysed by Eskom replica evaluation metallurgist to ensure that replicas with good quality are used for research. The replicas were analysed under light microscope at 500X magnification using Leica light microscope. X20 pipework with the required creep damage was then identified.

Master curves are also used to perform life estimates within Eskom and these are based on the following equation (PD6525 1990):

$$P(\sigma) = a + b(log\sigma) + c(log\sigma)^2 + d(log\sigma)^3 + e(log\sigma)^4 \quad \text{...Equation 22}$$

$$= \frac{logt - logta}{(T - Ta)^r}$$

where:

P(σ) – stress rupture parameter,

σ – stress (Pa),

a to e – constants,

r – temperature exponent,

T – temperature (K), and

t – time to rupture (h).

The life estimates using master curves are strongly affected by operating conditions (temperature and stress) and this method will also be used to evaluate the life of service exposed X20 steel samples.

3.6. Light Microscopy Evaluation

Replica samples, weldments (BM, FGHAZ, CGHAZ and WM) and simulated HAZ (FGHAZ and CGHAZ) samples and creep rupture samples were analyzed after surface preparation and etching using Leica light microscope. Creep damage was investigated using the replica samples and the damage observed was quantified using Eskom Replication Technique Procedure. Microstructural evolution during welding was investigated using light microscopy. This was

done by analyzing different regions of the weldments and simulated HAZ samples. Creep ruptured samples were analyzed under light microscope to study fracture location of the weldments.

3.7. Scanning Electron Microscopy (SEM) Analysis

EBSD provides quantitative microstructural information about the crystallographic nature of metals, minerals, semiconductors, and ceramics, in fact most inorganic crystalline materials. It (PD6525 1990)reveals grain size, grain boundary character, grain orientation, texture, and phase identity of the sample under the beam. Centimeter-sized samples with millimeter-sized grains, to metal thin films with nanograins may be analyzed. The nominal angular resolution limit is ≈0.5° and the spatial resolution is related to the resolution of the SEM, but for modern field emission SEMs (FE-SEMs), 20nm grains can be measured with reasonable accuracy. The macroscopic sample size is dependent on the ability of the SEM's stage and chamber to orient a sample at 70° tilt at an appropriate working distance, usually in the range 5 to 30mm (Maitland 2007).

As EBSD is a surface-sensitive technique, with the diffraction signal coming from the top few nanometres (5-50nm) of the crystal lattice, it is essential that this top layer remains free from damage and also free from contamination or oxidation layers and this makes specimen preparation absolutely critical for collecting good EBSD data. The fact that the specimen must be tilted up to high angles (typically 70°), means that the surface topography/relief must be kept to an absolute minimum to avoid shadowing problems (Struers 2010).

Nova Nano SEM equipped with Back-Scattered Electrons (BSE), Secondary Electrons (SE) and Energy Dispersive X-ray (EDX) detectors was used to analyze X20 weldments (BM, FGHAZ, CGHAZ and WM), simulated HAZ (FGHAZ and CGHAZ) samples and creep ruptured samples after surface preparation and etching.

Etched samples were analyzed using accelerating voltage of 20keV, spot size of 2.5 and a working distance approximately 6 mm. Chemical compositions of phases observed was analyzed using the electron dispersive spectroscopy (EDS).

Samples cut from the weldments and simulated HAZ samples were mounted in a resin, ground with silicon paper and electrolytic polished for electron backscatter diffraction (EBSD) analysis. EBSD analysis was carried out in the BM, FGHAZ (weldment and simulated), CGHAZ

(weldment and simulated) and WM. JEOL7001F + Nordlys SEM was used to conducted the analysis using a magnification of 1100X, step size of 0.1µm, voltage of 15kV, and a beam current of 4-5nA.

3.8. Transmission Electron Microscopy (TEM) Analysis

In the TEM only thin samples, which allow a fraction of the incident electron beam to go through the sample can be studied. When an accelerated beam of electrons impinges upon a sample, a variety of interactions takes place as shown in Figure 23. The versatility of electron microscopy and x-ray microanalysis is derived in large measure from this variety of interactions that the beam electrons undergo in the specimen (Williams 2009).

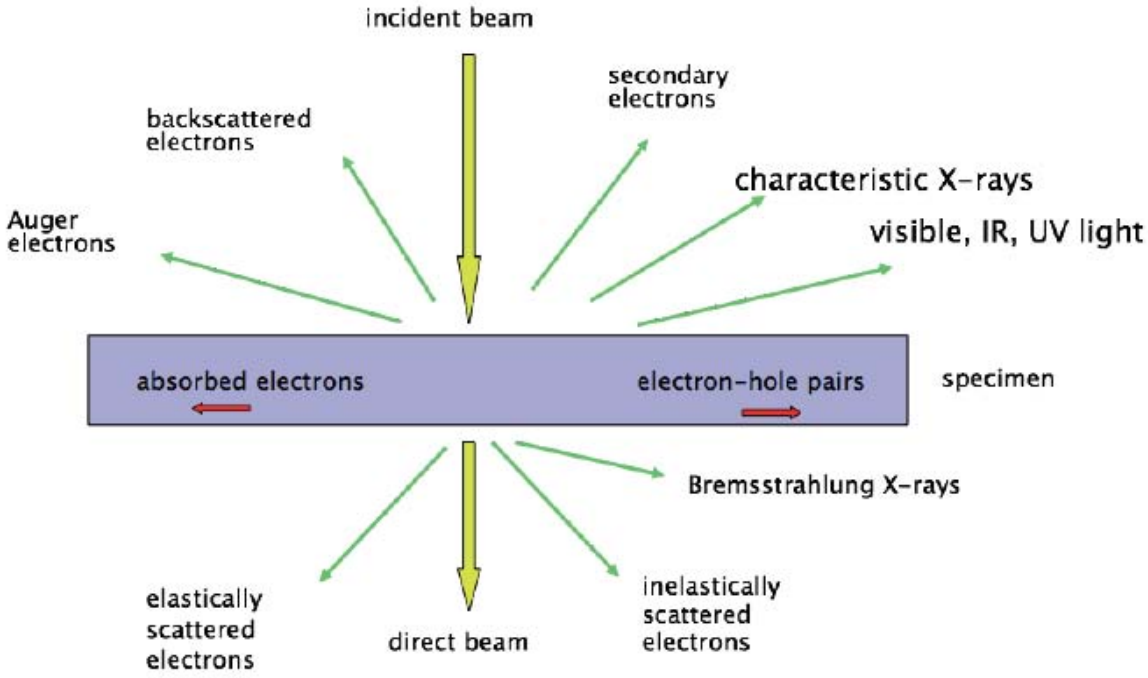

Figure 23: Interactions that occur during the collision of electron beam and the sample (Williams 2009).

During TEM analysis, the sample is placed in front of the objective lens in a form of thin foil, thin section, or fine particles transparent for the electron beam. The objective lens forms an image of the electron density distribution at the exit surface of the specimen based on the electron optical principles. A diffraction pattern is formed in the back focal plane of the objective lens and the recombination of the diffracted beams forms an image in the image plane of the objective lens. The diffraction, projection, and intermediate lenses below the objective lens are used to focus and magnify either the diffraction pattern or the image onto a fluorescent screen, which converts the electrons into visible light signal (Williams 2009). Figure 24 shows a typical TEM set-up.

The transmission electron microscope may be operated to produce either a diffraction pattern from a specific region of the specimen or one of several types of images, where quantitative information about the microstructure of the material is required, and a detailed correlation is made between the diffraction pattern and the image (Williams 2009).

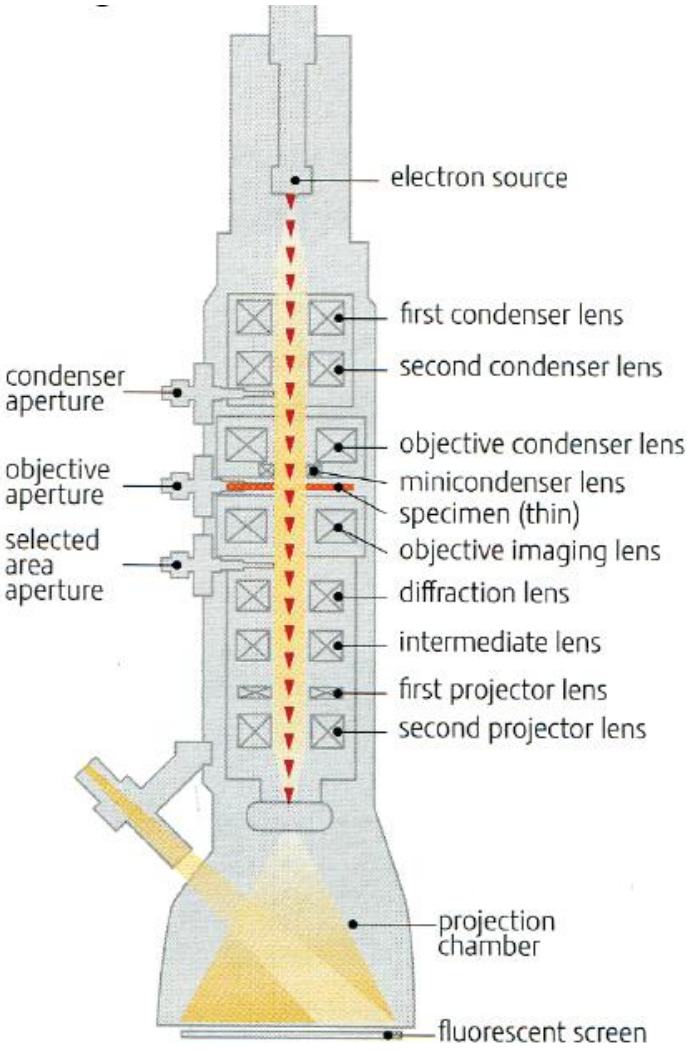

Figure 24: Typical TEM set-up (Williams 2009).

The HAZ of a weldment is only few millimeters and hence it is difficult to extract TEM samples from each region using the conventional method. FIB instrument provides the technology to extract TEM samples from the weldment HAZ. Samples with area of approximately 6mmx6mm and thickness of about 50nm are obtained after FIB extraction (Li 2012).

Bulk TEM samples were prepared from simulated HAZ samples using the conventional method (see reference (Giannuzzi 1999) for detailed information on the technique). The samples are initial cut to 0.5mm thickness and then punched into 3mm disks. The samples are then ground, polished, dimpled and finally ion milled to electron transparency. Samples with thickness less than 100nm were obtained.

FEI Helios NanoLab 650 Focused ion beam–SEM (FIB-SEM) was used to extract TEM samples from X20 weldments. Samples were extracted from the BM, FGHAZ, CGHAZ and WM of X20 weldments.

Prepared samples were analyzed using JEOL2100 (LaB6 filament) TEM using 200kV voltage. Scanning TEM (STEM) high annular angle dark field (HAADF) imaging was conducted using the analytical mode, 20cm camera length. EDS analysis was performed using Oxford 80mm^2 Silicon Drift Detector (SDD).

TEM sample thickness measurements were conducted using Image J program. The following equation was used to determine TEM sample thickness (Malis 1988):

$$\lambda_{TEM} = \frac{106F(E_o/E_m)}{\ln(2\beta E_o/E_m)} \text{ ... Equation 23}$$

where: λ_{TEM} is in nm, E_o in keV, β in mrad, F is a relativistic correction factor, and E_m is the average energy loss in eV.

The equation was stored in the TEM computer and the thickness was calculated using the variables used to perform TEM analysis. The TEM thickness data is stored with the image and programs such as ImageJ program can be used to obtain the sample thickness at the area of interest.

Sample thickness was evaluated across the entire EDS map and the thickness values were noted across the sample. An average sample thickness was calculated from the data obtained from the EDS map and this was used to calculate the precipitate parameters. The EDS maps obtained from samples prepared using the conventional method had a large scatter in thickness and sufficient data was captured to obtain a good average thickness.

4. Results

4.1. Overview on Samples and Investigations

X20 weldments and simulated HAZ samples were analysed in this study to characterise microstructural evolution after welding. Mechanical testing and microstructural analysis techniques were used to characterise the effect of welding on creep aged X20 steel. Hardness testing, tensile testing and cross-weld creep rupture tests were conducted to evaluate the change in mechanical properties after welding (see section 4.3,

4.4 and 4.5 respectively for details). Light microscopy analysis, scanning electron microscopy (SEM) analysis and transmission electron microscopy (TEM) analysis were carried out to characterise microstructural evolution during welding (for details see section 4.6, 4.7 and 4.8, respectively). Table 10 gives a summary of samples analysed and the methods used to conducted the investigations.

Table 10: Summary of samples characterised in the study and the methods used to conduct the analysis.

	Hardness Testing	*Tensile Testing*	*Creep Testing*	*Light Microscopy*	*SEM*	*TEM*
New X20 Weldment	**X**			**X**	**X**	**X**
New X20 Simulated FGHAZ	**X**	**X**		**X**	**X**	**X**
New X20 Simulated CGHAZ	**X**	**X**		**X**	**X**	**X**
X20_210_540 Weldment	**X**			**X**	**X**	**X**
X20_210_540 Simulated FGHAZ	**X**	**X**		**X**	**X**	**X**
X20_210_540 Simulated CGHAZ	**X**	**X**		**X**	**X**	**X**
X20_130_555 Weldment	**X**			**X**	**X**	**X**
X20_130_555 Simulated FGHAZ	**X**	**X**		**X**	**X**	**X**
X20_130_555 Simulated CGHAZ	**X**	**X**		**X**	**X**	**X**
New X20 – X20_210_540 Cross-weld			**X**	**X**	**X**	
New X20 – X20_130_555 Cross-weld			**X**	**X**	**X**	

4.2. Life Assessment for Service Exposed X20 Steels

When Eskom plans to have an outage, the first life estimates calculations are carried out using the master curves ($P(\sigma) = a + b(log\sigma) + c(log\sigma)^2 + d(log\sigma)^3 + e(log\sigma)^4$ ...Equation 22) as only operating parameters are available at this stage. The life estimates results were conducted using the PD6525 data (PD6525 1990) and the results obtained are shown in Table 11.

Table 11: Life estimates results for X20_210_540 and X20_130_555 obtained using the master curves.

Sample ID.	ID (mm)	Minimum WT (mm)	Operating Temp (ºC)	Operating hrs	%Life Exhaustion (PD6525 - 20%)	%Life Exhaustion (PD6525 - mean)
X20_210_540	250	30	540	208320	26	12
X20_130_555	250	30	555	129801	52	23

Maximum life exhaustion of 26% and 52% was calculated for X20_210_540 and X20_130_555, respectively.

The second stage of life management involves replica lifting and assessing of the creep damage on steam pipework. X20 steel pipework used for research was replicated and then the creep damage was measured on the replicas to quantify the density of creep voids on these steels.

Table 12 shows a summary of replica analysis results obtained on the X20 steel pipework used for research. A maximum of 200voids/mm^2 and 485voids/mm^2 was measured on the surface of X20_210_540 and X20_130_555, respectively. No voids were noted on New X20.

Table 12: Creep damage measured on the surface of New X20, X20_210_540 and X20_130_555 pipework.

Sample ID.	*Creep Damage (voids/mm^2)*
New X20	No damage
X20_210_540	130≤x≤200
X20_130_555	340≤x≤485

Typical replica micrographs of the samples used for research are shown in Figure 25. Few creep voids observed on the samples were associated with inclusions.

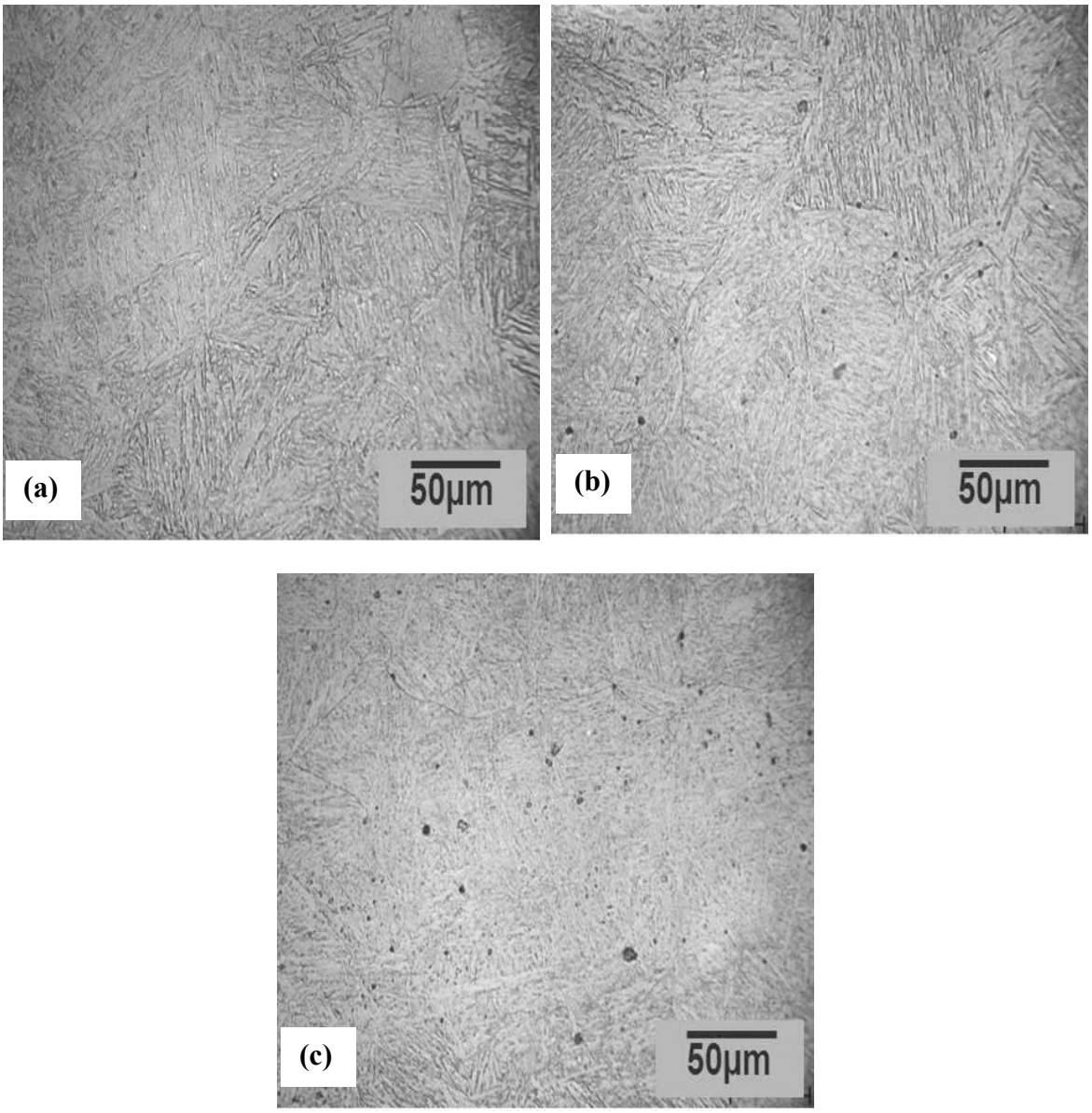

Figure 25: Replica-micrographs of research samples. Creep damage was observed on service exposed samples (a) New X20, (b) X20_210_540 (130 – 200 voids/mm^2) and (c) X20_130_555 (340 – 485 voids/mm^2).

Through-wall creep damage profile measured on service exposed samples is shown in Table 13. An average creep void density of 178voids/mm^2 and 140voids/mm^2 was measured on X20_210_540 and X20_130_555, respectively. An inhomogeneous distribution of creep voids was observed on both samples and this can be attributed to system loading that take place during

shut downs and when the unit is brought back to service. Detailed study should be conducted to understand this phenomenon.

Table 13: Through-wall creep damage profile measured on X20_210_540 and X20_130_555.

Distance(mm)	*X20_210_540(voids/mm^2)*	*X20_130_555(voids/mm^2)*
3(outer surface)	250	345
6	170	100
9	190	95
12	235	105
15	195	210
18	115	80
21	170	70
24	235	175
27	120	75
30(inner surface)	95	145
Average	178	140

Maximum and Average creep voids density was used to perform life estimates for serviced exposed X20 steels. The life estimates were conducted using creep damage models and the results obtained are shown in Table 14.

Table 14: Remaining life estimates for service exposed X20 steels.

Sample ID.	*Operating hrs.*	*%Life Exhaustion, λ=3.4 (maximum/average)*	*Remaining life (maximum/average)*
X20_210_540	208320	69/54	~10/20 years
X20_130_555	129801	84/44	~2/18 years

If remaining years calculated is <3years then class 1
If remaining years calculated is 3 - 9 years then class 2
If remaining years calculated is 10-18 years then class 3 else class 4 with onset of damage.

Creep life estimates conducted using the maximum damage measured on the surface of X20 steel pipework indicated end of life for X20_130_555, while X20_210_540 had remnant life of 10 years. The remaining life estimates using the average creep voids density indicated a remnant life above 18 years for both steels and this means that these steels can still be managed within the Eskom outage philosophy shown in Table 15.

Table 15: Eskom component life interpretation.

Damage Classes	Default Recommendations
CLASS 1 Component at the end of its useful life. Not manageable inside outage philosophy. High risk of failure with continued operation.	1. Replace immediately. Do not operate further 2. Maybe limit operation with full risk assessment and special mitigation measures.
CLASS 2 Component approach end of its useful life. Still manageable inside outage philosophy. Plan replacement and operate within design.	1. Replace within 3 years. 2. Investigate all excursions and dynamic events.
CLASS 3 Damaged component with significant remnant life. Safely manageable by inspections.	1. Inspect within 3 years. 2. Operate within design and maintain within Eskom philosophy.
CLASS 4 Component without damage. Manageable within outage intervals.	1. Inspect mostly within 6 years if past design life. 2. In exceptional cases, inspection intervals could be extended to 9 years.

4.3. Hardness profile of weldments

New X20, X20_210_540 and X20_130_555 weldments and simulated HAZ samples were analysed using the EMCO Vickers hardness testing machine. A load of 3kg was used for all the hardness tests. Table 16 shows hardness measurements conducted on the base material (BM) of X20 samples used for research. Hardness values in the lower bound of X20 steel hardness specification (215-265HV_{10kg}) were obtained for X20_210_540 BM (EPRI 2006).

Table 16: Through-wall hardness profile measured on the base material of X20 samples used for research ($HV3_{kg}$).

	New X20	*X20_210_540*	*X20_130_555*
Distance (mm)	***HV3***	***HV3***	***HV3***
0	255	196	249
2	256	210	247
4	256	224	241
6	257	204	243
8	254	215	239
10	256	208	235
12	256	212	235
14	254	209	237
16	248	211	243
18	260	208	243
20	259	218	246
22	257	215	241
24	260	202	234
26	256	202	243
28	265	209	250
30	260	204	248
Average	**257**	**209**	**242**
Std. dev.	**3.7**	**6.9**	**5.1**

Figure 26 and Figure 27 show hardness profiles measured on X20 weldments. The heat-affected zone showed a decrease in hardness values from the WM to the BM. The zones in the weldment were identified from the hardness values measured. The HAZ region with the highest hardness

value was identified as the CGHAZ while the FGHAZ was identified as the HAZ region with intermediate hardness values.

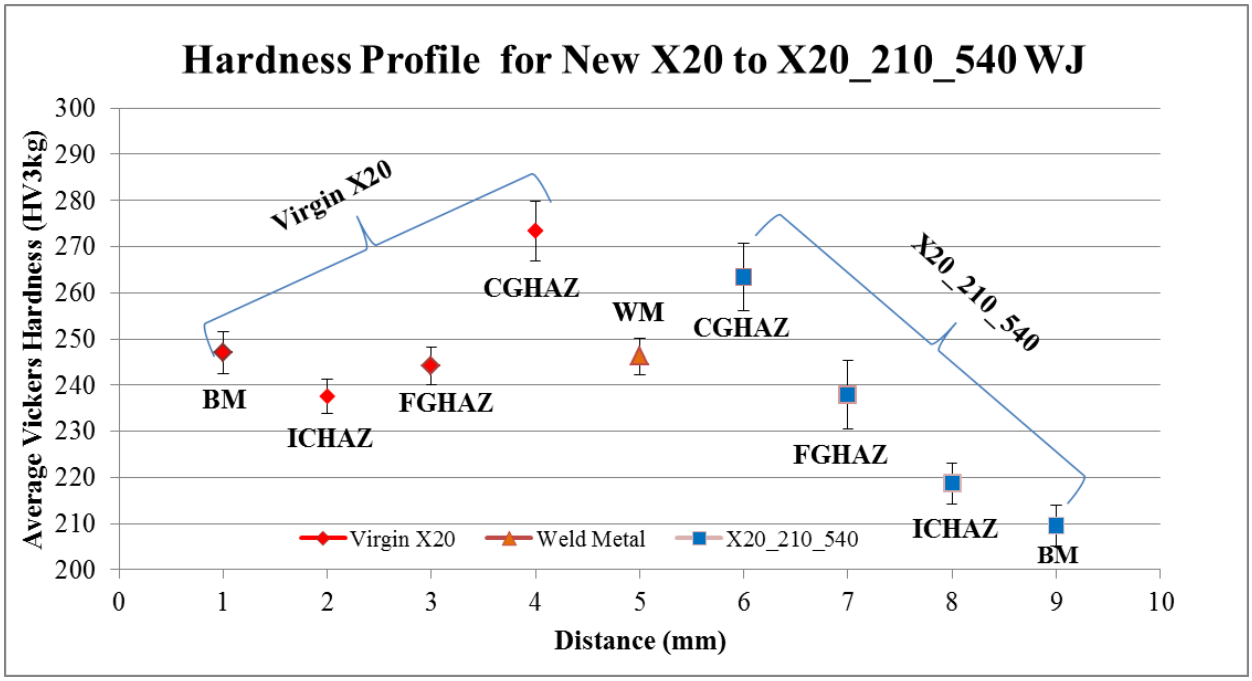

Figure 26: **Hardness profile for New X20 - X20_210_540 weld-joint. High hardness values were measured in the CGHAZ, while low hardness values were measured in the ICHAZ. Intermediate hardness values were measured in the FGHAZ.**

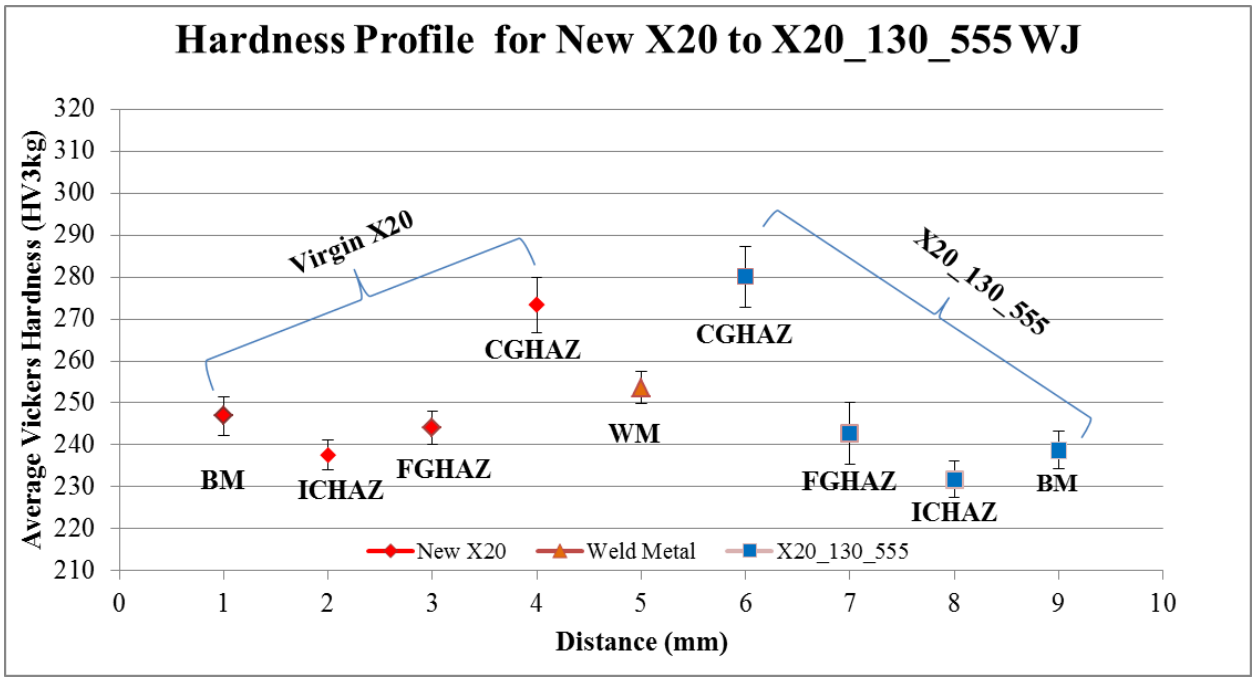

Figure 27: Hardness profile for New X20 - X20_130_555 weld-joint. High hardness values were measured in the CGHAZ, while intermediate hardness values were measured in the FGHAZ.

FGHAZ and CGHAZ of X20 steel was simulated was using Gleeble 3800 (details on the work are shown in section 2.3). Table 17 shows hardness profiles obtained on simulated HAZ samples. Low hardness values were measured in the simulated FGHAZ.

Table 17: Hardness profiles for simulated HAZ obtained using EMCO Vickers Hardness Testing Machine ($HV3_{kg}$).

	New X20 Simulated FGHAZ	New X20 Simulated CGHAZ	X20_210_540 Simulated FGHAZ	X20_210_540 Simulated CGHAZ	X20_130_555 Simulated FGHAZ	X20_130_555 Simulated CGHAZ
	249	257	230	289	233	265
	253	263	225	286	237	273
	253	255	222	293	230	267
	255	265	230	289	235	263
	246	269	228	303	233	302
	246	275	225	289	253	316
	242	282	220	289	259	296
	247	273	222	291	282	303
	247	277	227	293	273	298
	253	280	222	296	263	301
Average	**249**	**270**	**225**	**292**	**250**	**288**
Std.dev	**4**	**9**	**4**	**5**	**19**	**19**

Nano hardness measurements were conducted on X20 steel weldments using CSM Nano-indentation tester to identify the regions of interest in the HAZ. The nano hardness test results for X20 steel weldments are shown in Figure 28, Figure 29 and Figure 30. The FGHAZ was identified as the HAZ region with intermediate hardness values, while the CGHAZ was identified as the HAZ with high hardness values.

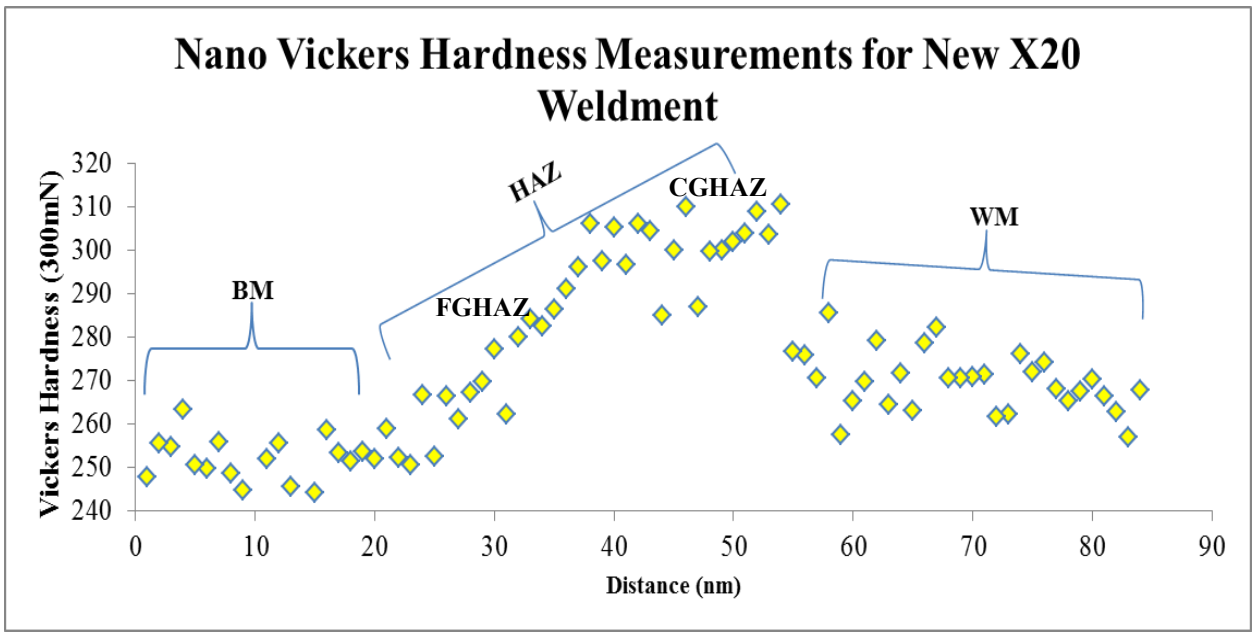

Figure 28: **Nano hardness profile for New X20 weldment. The CGHAZ was identified as the HAZ region with high hardness values, while the FGHAZ was identified as the HAZ region with intermediate hardness.**

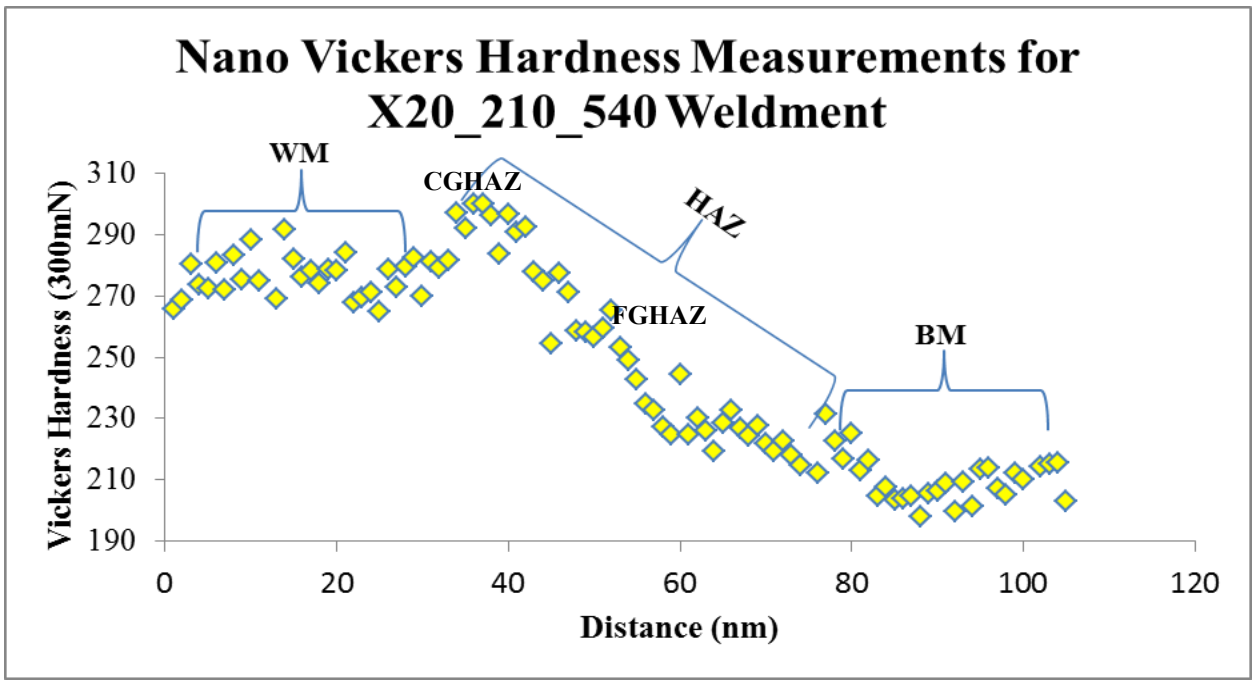

Figure 29: **Nano hardness profile for X20_210_540 weldment. The CGHAZ was identified as the HAZ region with high hardness values, while the FGHAZ was identified as the HAZ region with intermediate hardness.**

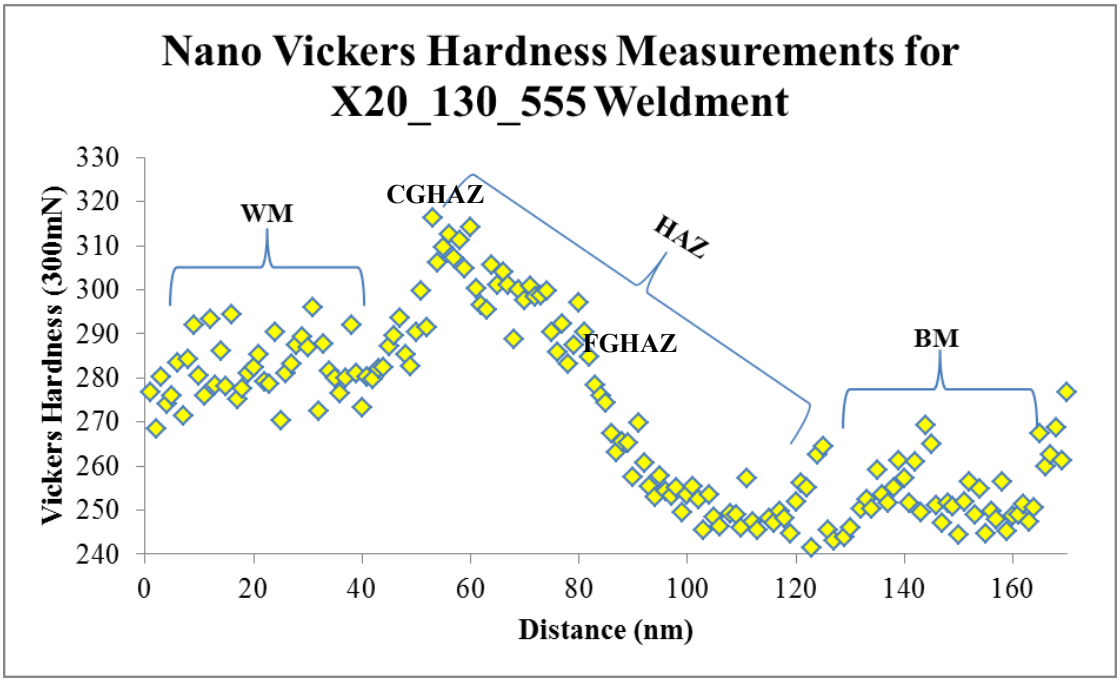

Figure 30: **Nano hardness profile for X20_130_555 weldment. The CGHAZ was identified as the HAZ region with high hardness values, while the FGHAZ was identified as the HAZ region with intermediate hardness.**

4.4. Creep Rupture Tests and Life Estimates for X20 Steel WJ's

Cross-weld creep rupture tests were carried out to study to evaluate the reduction in creep strength after welding and to evaluate the fracture location of X20 steel weldments. Creep rupture tests were conducted at 650˚C, applying a reference stress of 63MPa. The tests were conducted at this temperature in order obtain results within the research time frame but long term creep tests are planned.

The cross-weld creep rupture tests results for New X20 to X20_210_540 WJ, and New X20 to X20_130_555 WJ are shown in Table 18.

Table 18: Cross-weld creep rupture tests results for X20 weldments.

Sample ID.	*Temperature (˚C)*	*Average rupture time (hr)*	*% Elongation*	*% Δ Area*
New X20 - X20_210_540 WJ	650	357	1.3	2.6
New X20 - X20_130_555 WJ	650	239	1.2	2.3

Low creep ductility values were observed on both X20 steel WJ's and this can be attributed to loss of ductility during service exposure.

Microstructural analysis was carried out at fracture location to evaluate damage propagation in vicinity of fracture. Figure 31 and Figure 32 show micrographs of New X20 – X20_210_540 weld-joint fracture location. The fracture location for New X20 – X20_130_555 weld-joint is shown on Figure 33 and Figure 34. The weld-joints ruptured on the FGHAZ of service exposed samples i.e. FGHAZ of X20_210_540 weldment and X20_130_555 weldment. High density of creep voids was noted adjacent the fracture location.

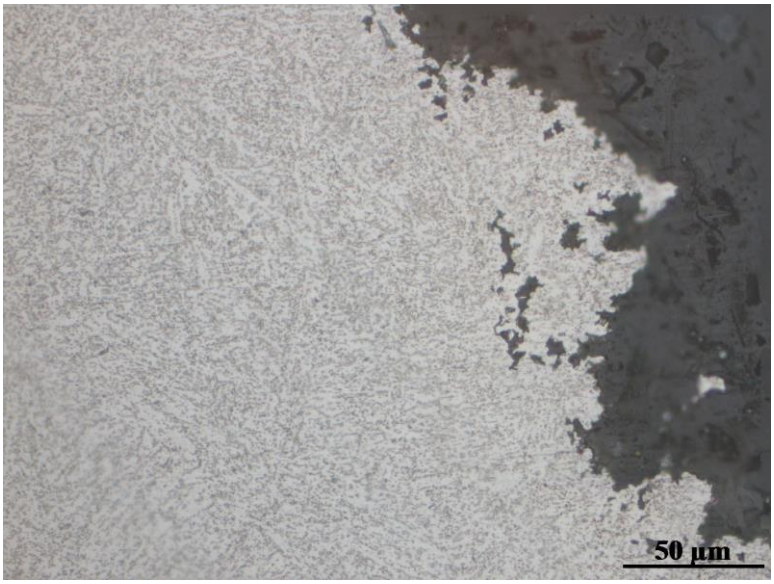

Figure 31: Micrograph of New X20 - X20_210_540 WJ showing the fracture location. The sample fractured on X20_210_540 FGHAZ. Fissures were observed in the fraction location.

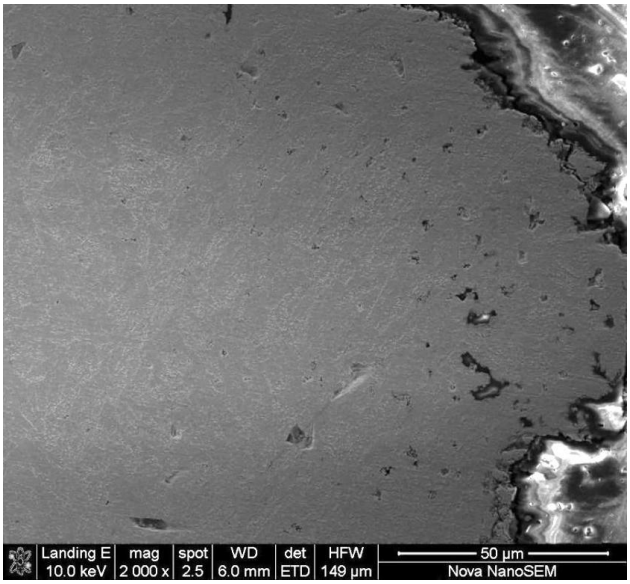

Figure 32: **SEM-SE micrograph of New X20 - X20_210_540 WJ showing the fracture location (X20_210_540 FGHAZ). High density of creep cavities was observed adjacent the fracture location.**

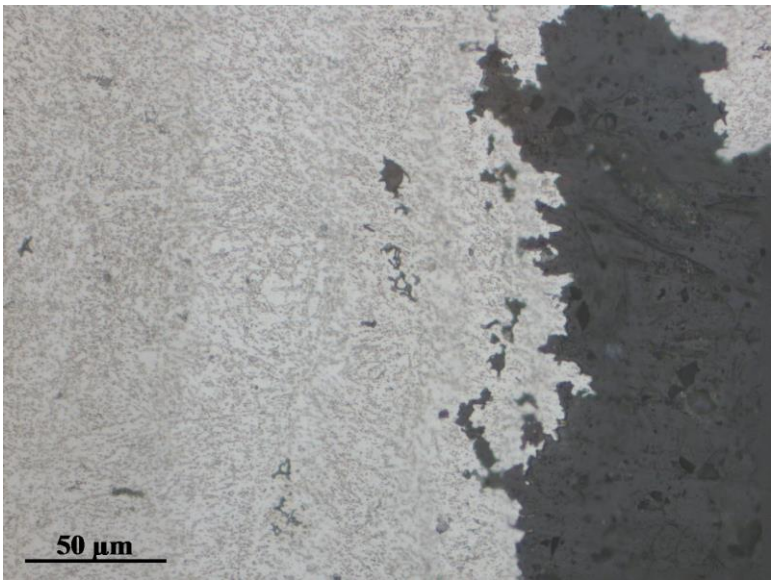

Figure 33: **Micrograph of New X20 - X20_130_555 WJ showing the fracture location. The sample fractured on X20_130_555 FGHAZ. Fissuring was noted in the fracture location.**

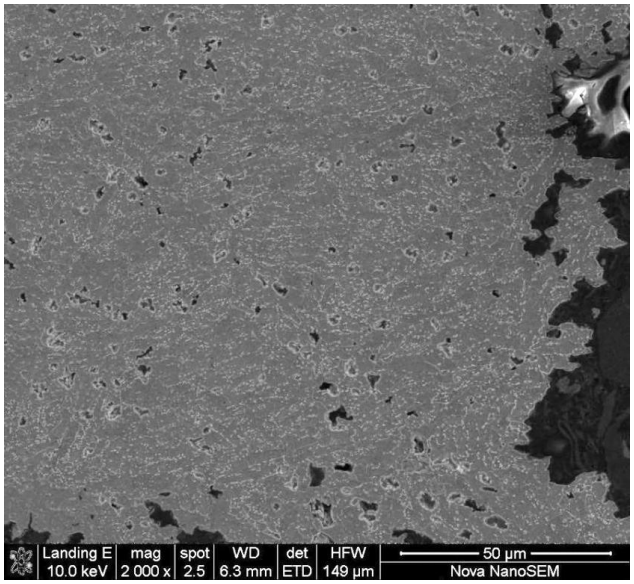

Figure 34: SEM-SE micrograph of New X20 - X20_130_555 WJ showing the fracture location (X20_130_555 FGHAZ). Significantly high density of creep cavities was noted adjacent the fracture location.

Creep life estimates were conducted for the X20 steel WJ's using the results obtained from creep damage models (% life exhaustion). The master curves (using PD6525 parameters) were used to estimate the life of the creep aged BM at the creep test conditions (650˚C, 63MPa). The life for a weldment with creep aged BM was calculated using a weld reduction factor of 70%. This factor is normal used by Eskom during welding of virgin X20 steel. The results obtained are summarised in Table 19 and Table 20.

Table 19: Creep life estimates for New X20 to X20_210_540 WJ at 650°C and 63MPa.

	New X20 to X20_210_540 WJ			
	BM exhaustion, λ=3.4 (%)	**BM failure prediction, PD6525 -20% (h)**	**Weld failure prediction,WRF=70% (h)**	**Actual failure (h)**
Maximum	69%	246	173	357
Average	54%	368	257	

Table 20: Creep life estimates for New X20 to X20_130_555 WJ at 650°C and 63MPa.

	New X20 to X20_130_555 WJ			
	BM exhaustion, λ=3.4 (%)	**BM failure prediction, PD6525 -20% (hr)**	**Weld failure prediction,WRF=70% (hr)**	**Actual failure (hr)**
Surface	84%	125	87	239
Prep average	44%	442	309	

The creep life estimates conducted using the maximum creep void density result in over-conservative failure prediction, while the estimates conducted using average creep void density give realistic failure prediction.

The estimated creep rupture data for X20 steel weldments obtained using the average creep void density was superimposed to creep rupture test results of X20 steel WJ's and this is illustrated in Figure 35 and Figure 36.

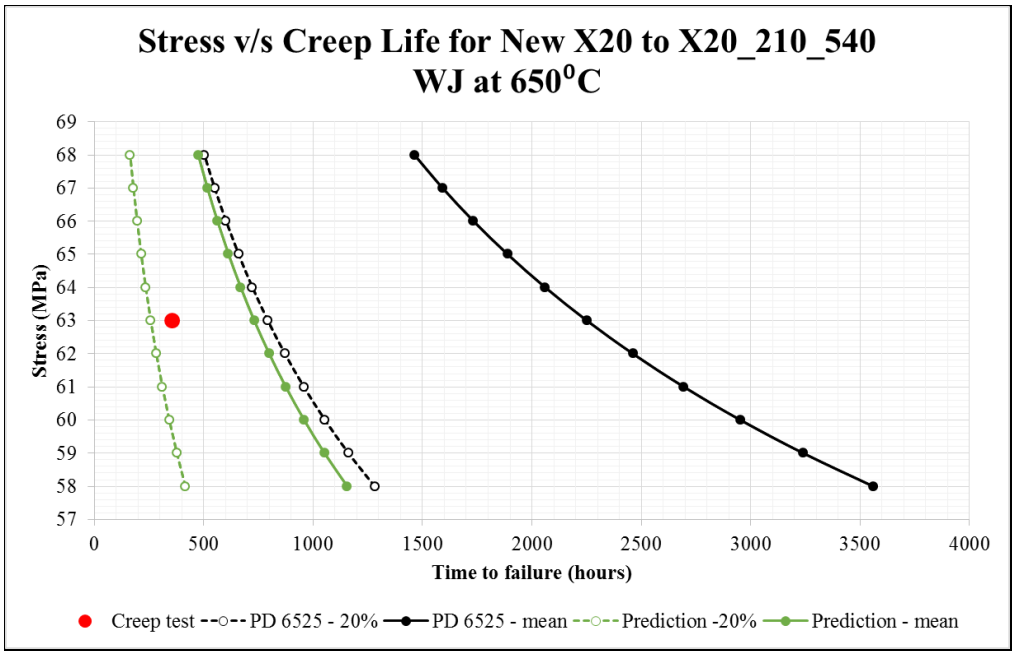

Figure 35: **Relationship between stress and creep life for New X20 to X20_210_540 WJ at 650^{0}C. New X20 – X20_210_540 WJ (ruptured in the FGHAZ of X20_210_540) has creep properties below the PD6525 scatter-band for creep aged BM with 54% exhaustion but has properties within the predicted scatter-band (close to minimum) for a weldment (WRF of 70%).**

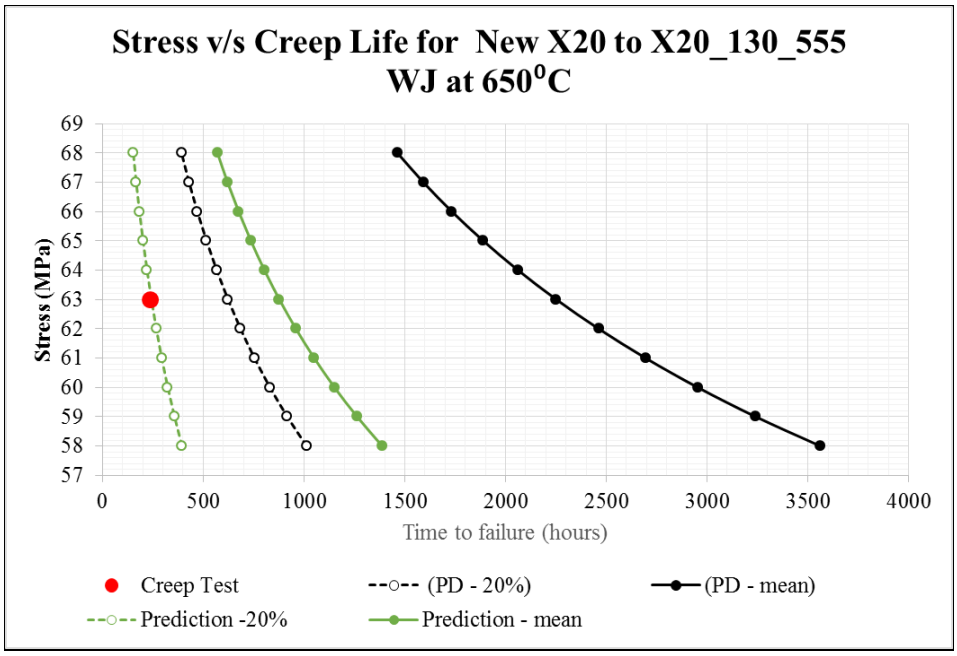

Figure 36: Relationship between stress and creep life for New X20 to X20_130_555 WJ at 650°C. New X20 – X20_130_555 WJ (ruptured in the FGHAZ of X20_130_555) has creep properties below the PD6525 scatter-band for creep aged BM with 44% exhaustion but has properties just within the predicted scatter-band (on the minimum) for a weldment (WRF of 70%).

Creep rupture data for both WJ's lies within the predicted scatter-band (towards the minimum) for a weldment with creep aged BM.

Remaining life estimates (RLE) were further conducted at plant operating condition for X20 steel weldments. RLE estimates were conducted using results obtained from the creep damage models and further using the master curves to predict the life of the creep aged BM from the operating data. The life of a weldment is then calculated using the WRF of 70%. The results obtained are shown in Table 21 and Table 22.

Table 21: Creep life estimates for X20_210_540 weldment at plant operating conditions (540^{0}C).

X20_210_540 Weldment (540^{0}C)				
	BM Exhaustion, λ=3.4 (%)	**BM RLE prediction, PD6525 -20% (hr)**	**Weldment RLE prediction, WRF=70% (hr)**	**Comment**
Maximum	69	93909	65736	replace in 3-6 years
Average	54	180188	126132	Replace in 12-15 years

Table 22: Creep life estimates for X20_130_555 weldment at plant operating conditions (540^{0}C).

X20_130_555 Weldment (540^{0}C)				
	BM Exhaustion, λ=3.4 (%)	**BM RLE prediction (hr)**	**Weldment RLE prediction, WRF=70% (hr)**	**Comment**
Maximum (540^{0}C)	84	24255	16978	Cannot operate further
Average (540^{0}C)	44	163095	114167	replace in 9-12years

Life management decisions are made are according to Table 15 as indicated before. Weldment life predictions indicated that X20_210_555 weldment had remaining life between 3 – 6 years and 12 – 15 years using the maximum and average creep damage, respectively. This indicates that this weldment can be safely managed within the Eskom outage philosophy. X20_130_555 weldment life predictions indicated end of life if the maximum creep damage is used to estimate the remaining life but predictions using the average creep damage indicated life between 9 – 12 years.

4.5. Hot Strength of Simulated Weldings

Tensile tests were conducted at X20 design temperature (545°C) at a strain rate of $10^{-2}s^{-1}$ to evaluate the effect of welding on X20 hot strength and ductility. Simulated HAZ specimens and the BM of New X20, X20_210_540 and X20_130_555 were used for tensile tests. Duplicate tests were carried out to evaluate if the results were consistent. Table 23 and Figure 37 show a summary of tensile tests results. A decrease in hot strength was noticed in the simulated FGHAZ and no significant change in ductility was noted.

Table 23: Yield strength, ultimate tensile strength (UTS) and ductility results for X20 BM and X20 simulated HAZ.

Sample ID.		Yield Strength(MPa)	UTS (MPa)	Elongation (%)
New X20	BM	118	508	8.5
		132	504	8.5
	Average	**125**	**506**	**8.5**
	Std.dev	**9.9**	**2.8**	**0.0**
	Simulated FGHAZ	90	416	8.2
		104	484	8.3
	Average	**97**	**450**	**8.3**
	Range	**9.9**	**48.1**	**0.1**
	Simulated CGHAZ	147	616	7.9
		145	601	7.8
	Average	**146**	**609**	**7.9**
	Range	**1.4**	**10.6**	**0.1**
X20_210_540	BM	143	488	8.1
		119	476	8.4
	Average	**131**	**482**	**8.3**
	Range	**17.0**	**8.5**	**0.2**
	Simulated FGHAZ	145	450	8.9
		135	463	8.8
	Average	**140**	**457**	**8.9**
	Range	**7.1**	**9.2**	**0.1**
	Simulated CGHAZ	169	550	8.3
		152	496	8.4
	Average	**161**	**523**	**8.4**
	Range	**12.0**	**38.2**	**0.1**
X20_130_555	BM	88	436	8.4
		112	471	8.8
	Average	**100**	**454**	**8.6**
	Range	**17.0**	**24.7**	**0.3**
	Simulated FGHAZ	89	450	8.8
		71	446	8.5
	Average	**80**	**448**	**8.7**
	Range	**12.7**	**2.8**	**0.2**
	Simulated CGHAZ	132	504	8.8
		153	519	8.6
	Average	**143**	**512**	**8.7**
	Range	**14.8**	**10.6**	**0.1**

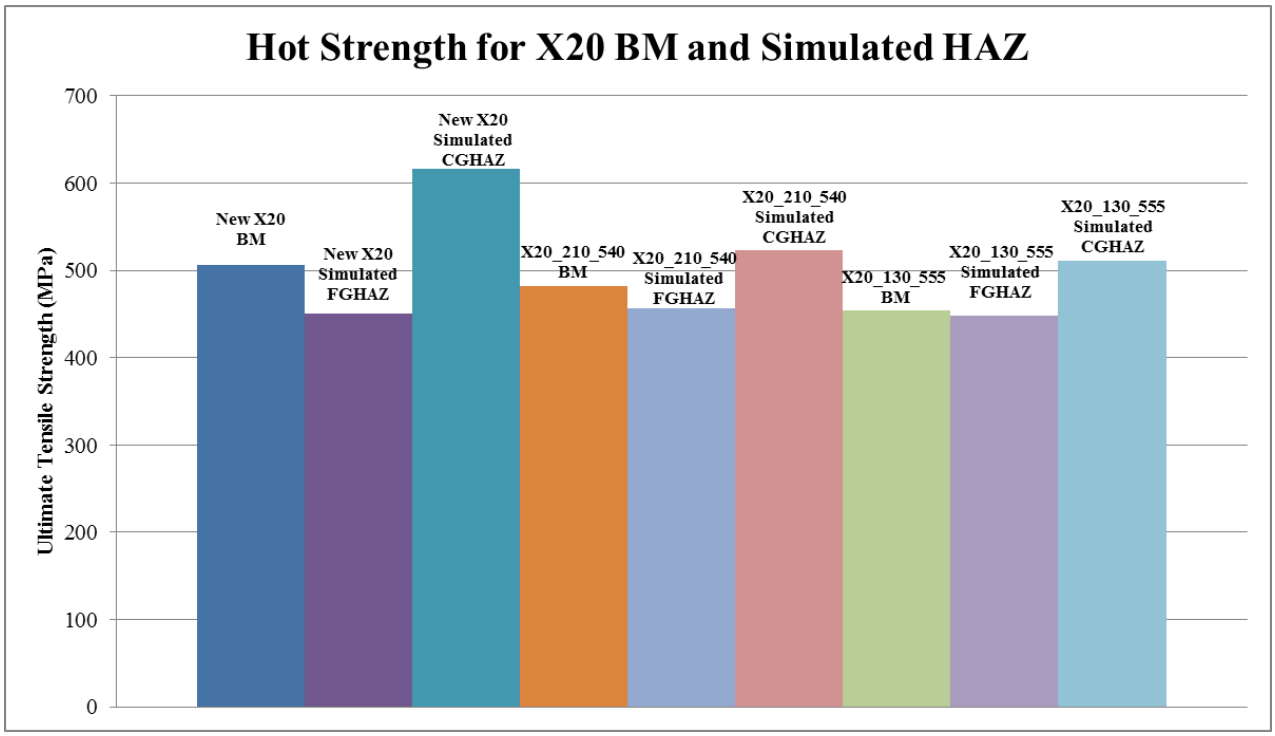

Figure 37: **Hot strength results for X20 BM and X20 simulated HAZ. Low ultimate tensile strength (UTS) values were measured in the simulated FGHAZ relative to the BM and simulated CGHAZ.**

4.6. General Microstructure

New X20, X20_210_540 and X20_130_555 weldments and simulated HAZ samples were analysed using light microscopy and SEM. Different regions of the weldments were analysed to evaluate microstructural evolution during welding.

Figure 38 shows gradient microstructures observed on New X20 weldment (BM, FGHAZ, CGHAZ and WM). Similar micrographs were observed on X20_210_540 and X20_130_555 weldments.

Simulated HAZ micrographs were analysed similarly and the results obtained for New X20 are shown in Figure 39. X20_210_540 and X20_130_555 simulated HAZ samples were also analysed under the light microscope and similar microstructures were observed.

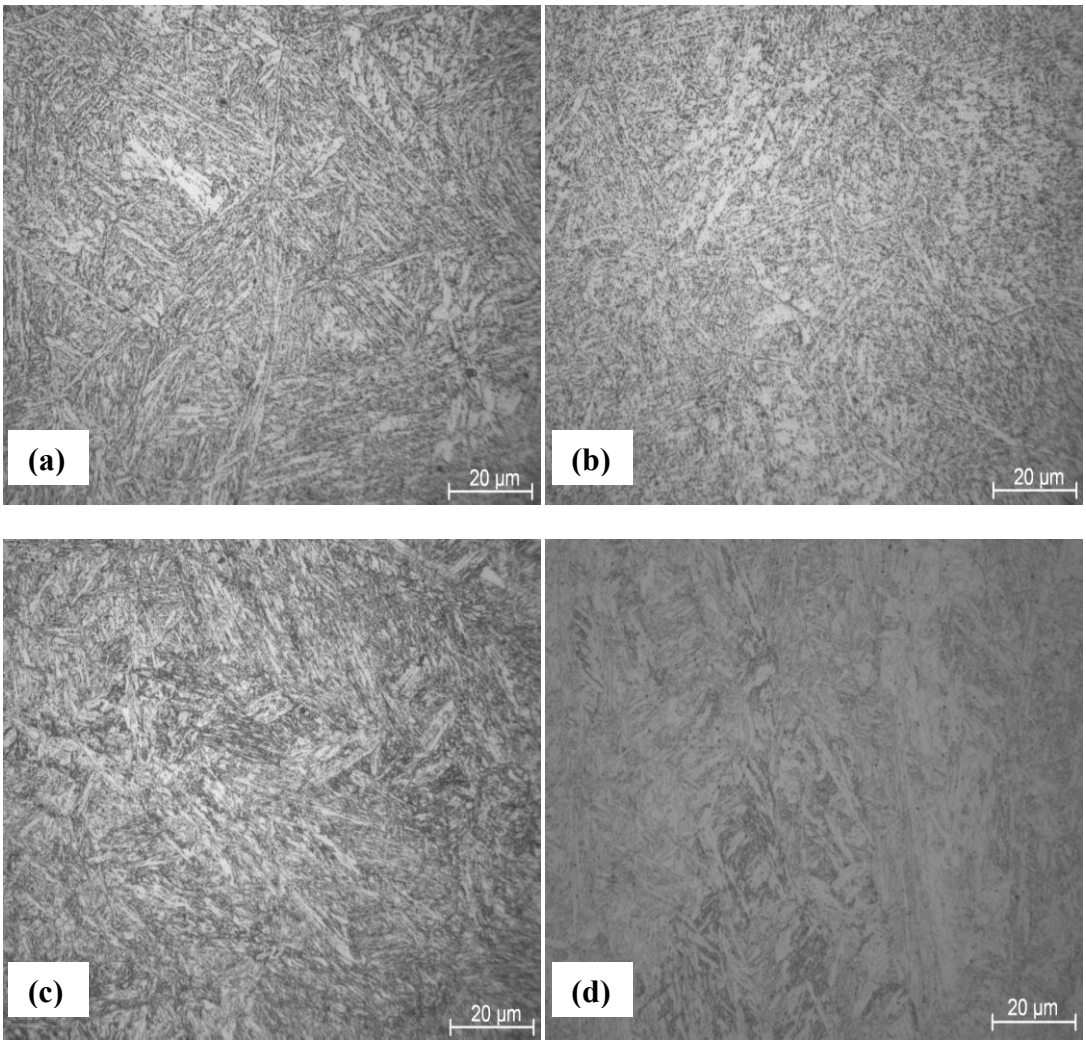

Figure 38: Micrographs of New X20 weldment (a) BM (b) FGHAZ (c) CGHAZ and (d) WM. Gradient microstructures were observed in the weldment.

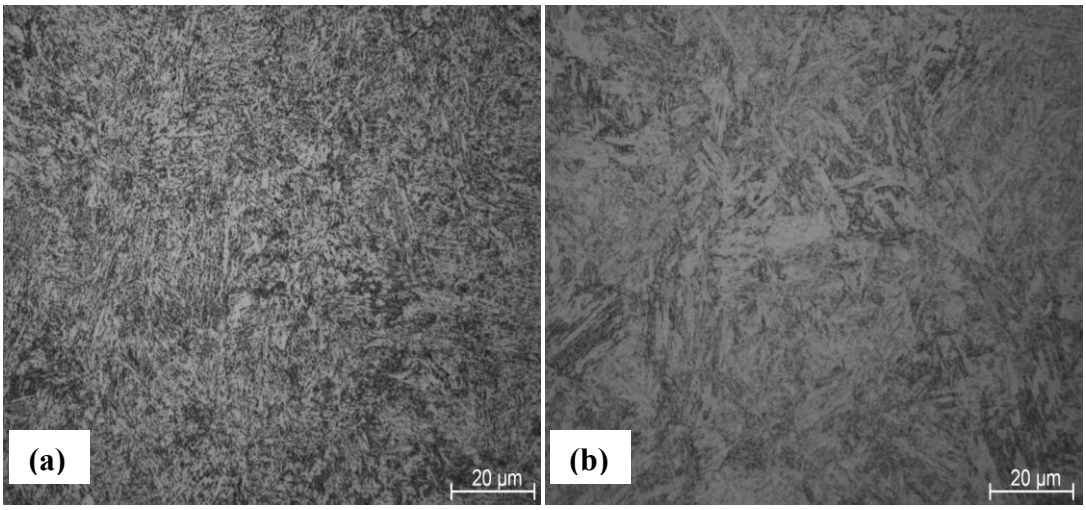

Figure 39: Micrographs of New X20 simulated HAZ (a) simulated FGHAZ (b) simulated CGHAZ.

SEM analysis of New X20 BM indicated finely dispersed precipitates and randomly dispersed silicon containing inclusions as shown Figure 40 and Figure 41. Micrographs taken on New X20 weldment and New X20 simulated HAZ are shown in Figure 42 and Figure 43, respectively. High precipitate density was noted in the CGHAZ of New X20 weldment relative to other regions of the weldment.

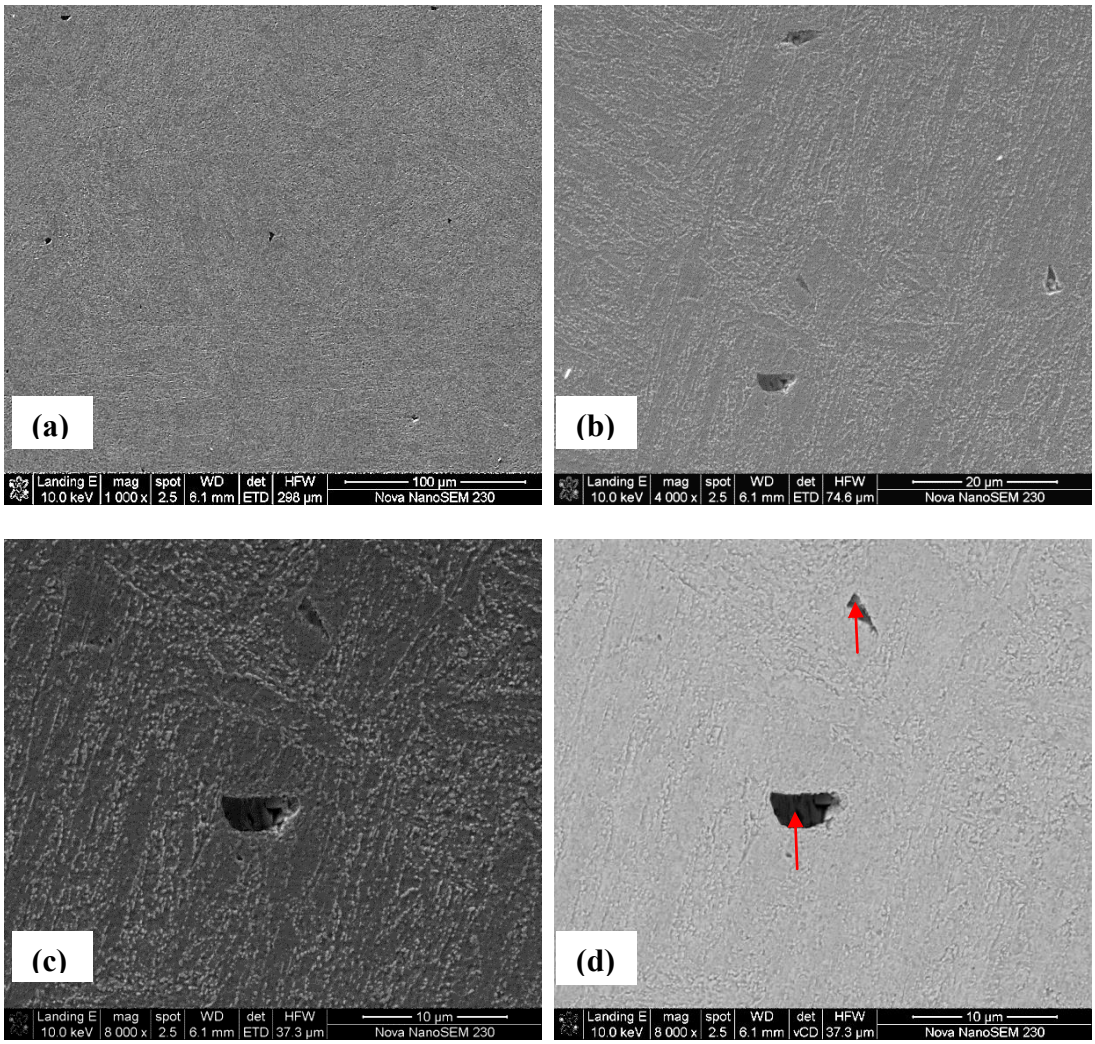

Figure 40: **SEM micrographs of the New X20 base material (BM). Finely dispersed precipitates and randomly dispersed inclusions (shown with arrows) were observed (a) SE image, (b) SE image, (c) SE image and (d) BSE image.**

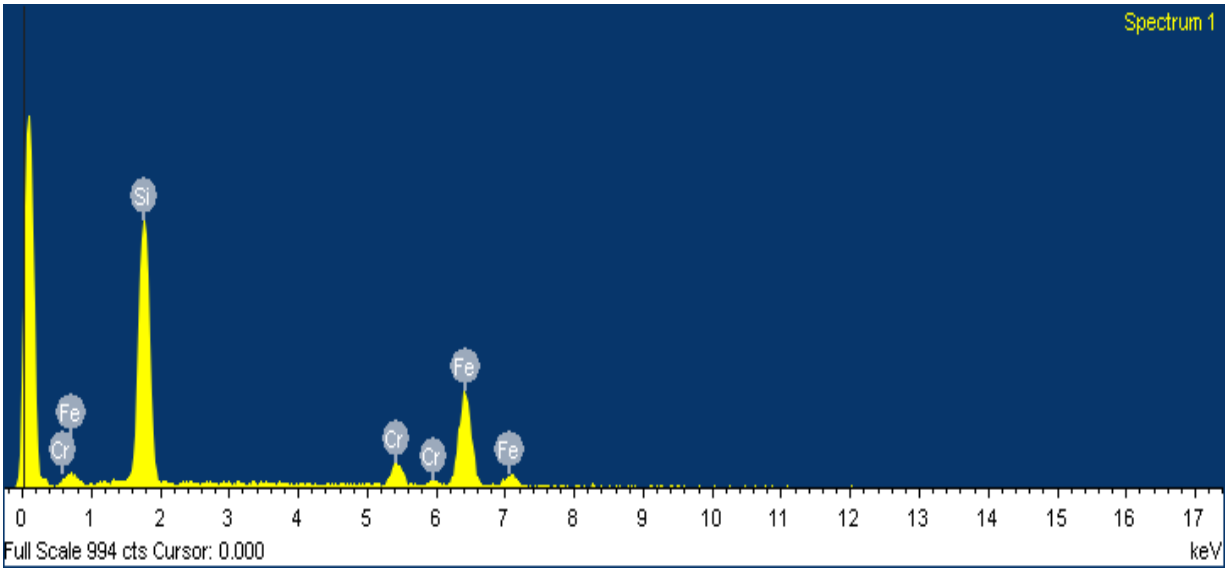

Figure 41: **SEM-EDS analysis of inclusions observed on New X20 BM indicated that they were silicon-containing inclusions.**

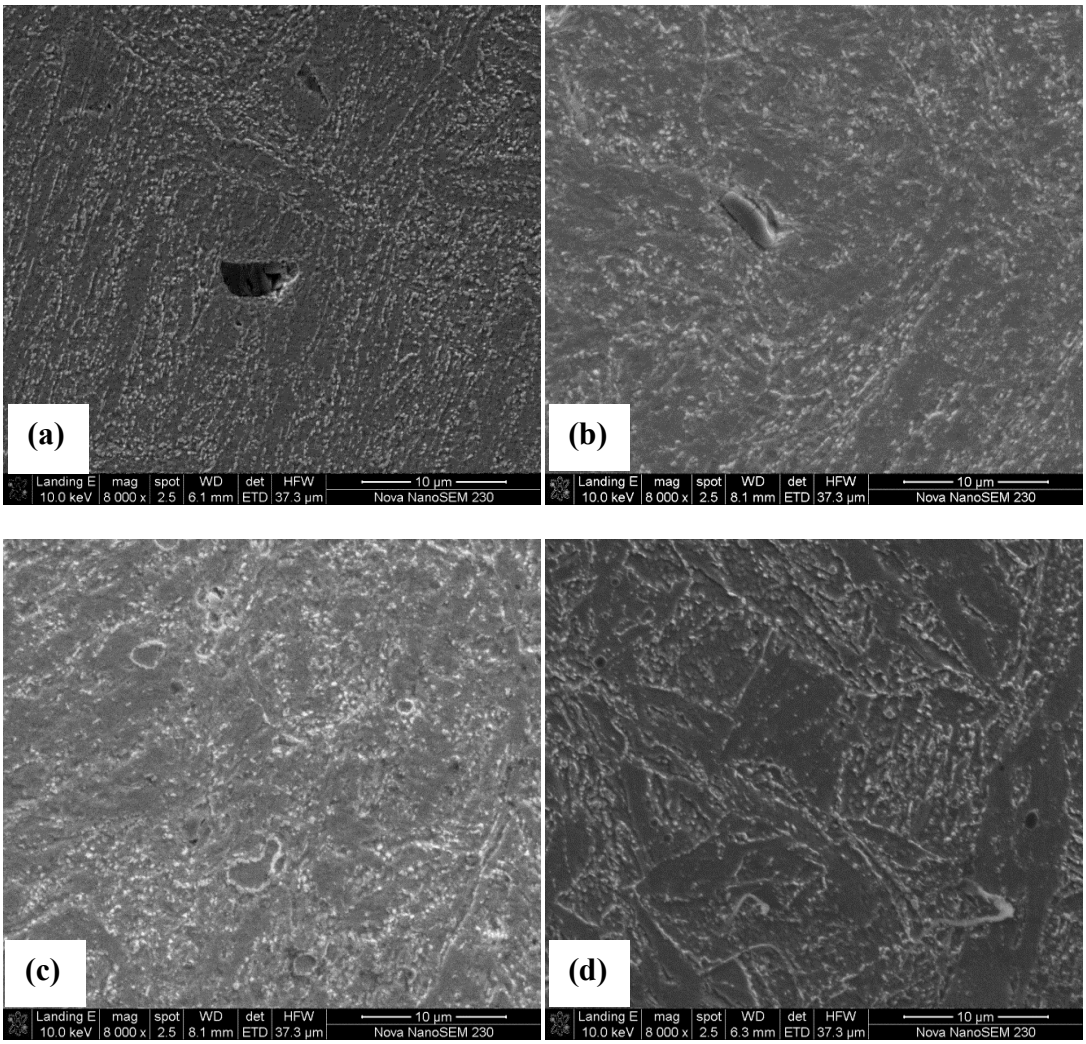

Figure 42: **SEM-SE micrographs of the New X20 weldment (a) BM (b) FGHAZ (c) CGHAZ (d) WM. High precipitate density was noted in the CGHAZ relative to other regions of the weldment.**

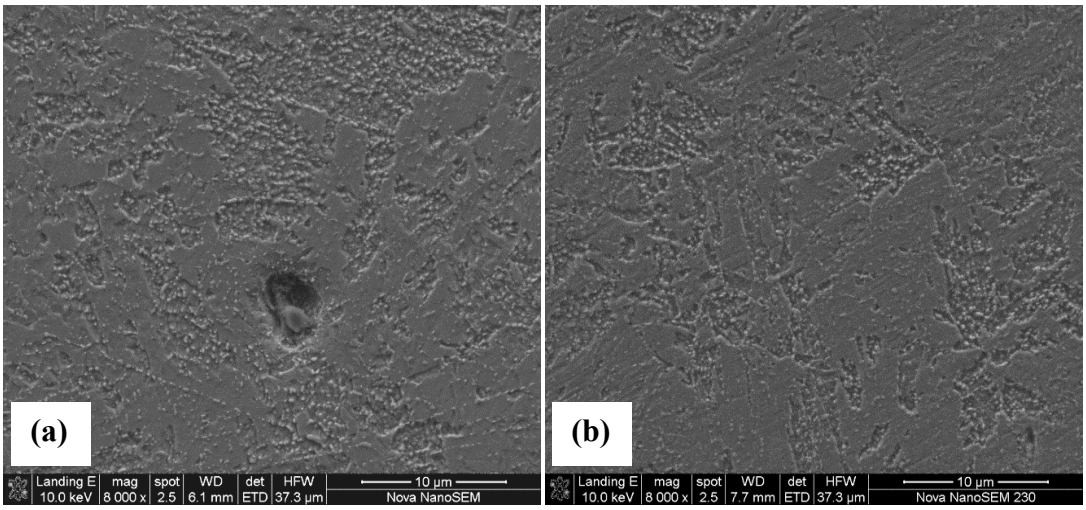

Figure 43: SEM-SE micrographs of New X20 simulated FGHAZ and simulated CGHAZ, respectively.

Figure 44 show micrographs of X20_210_540 BM. Strings of manganese sulfide and aluminum oxide/sulfide inclusions with evidence of damage were noted on X20_210_540 BM (see Figure 44, Figure 45 and Figure 46). The damage on MnS inclusions could have been introduced during the hot rolling process.

X20_210_540 weldment (FGHAZ and CGHAZ) and X20_210_540 simulated HAZ (FGHAZ and CGHAZ) SEM analysis results are shown in Figure 47. The precipitate distribution appeared to be modified after welding.

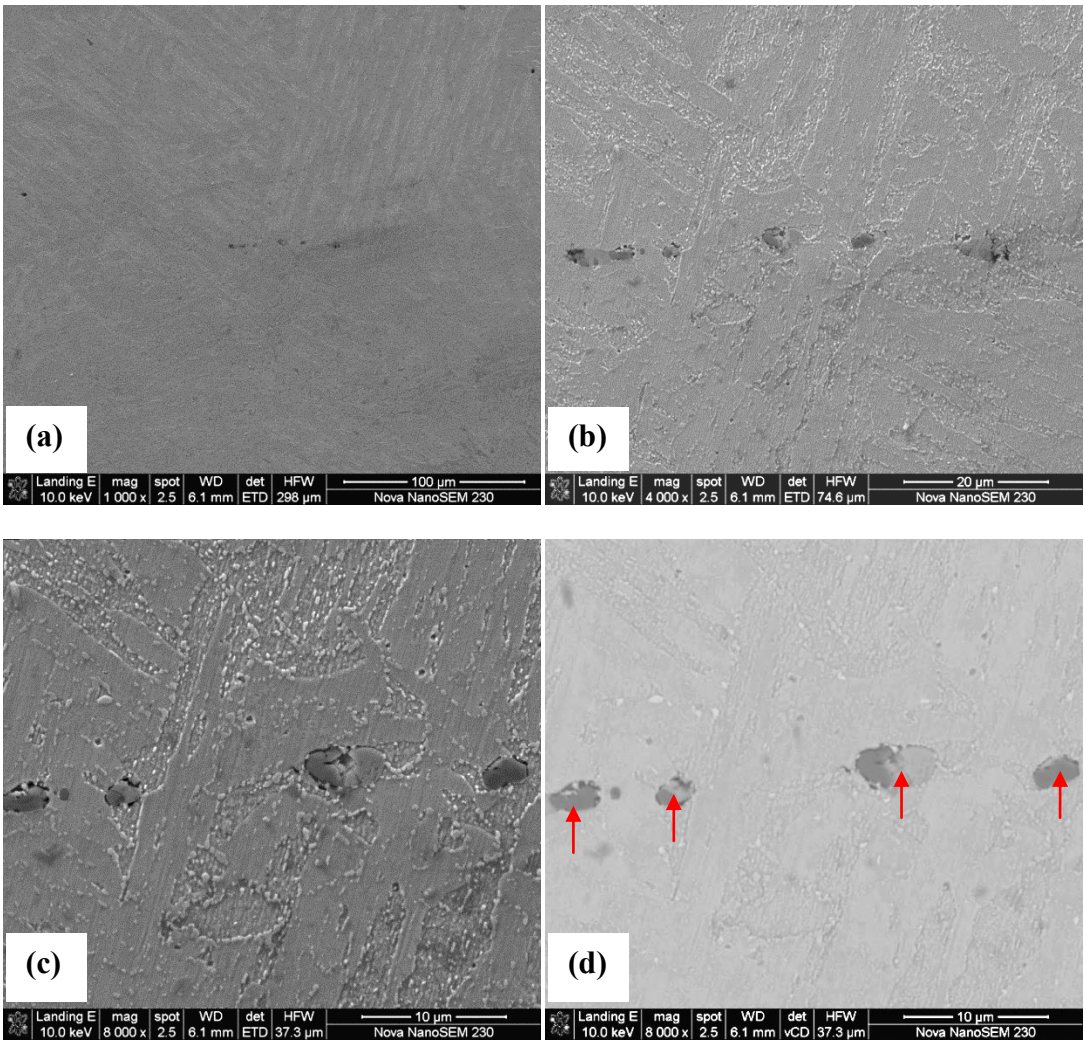

Figure 44: **SEM micrographs of X20_210_540 base material (BM). A coarse distribution of precipitates was noticed on this sample. Strings of inclusions (shown with arrows) which had evidence of damage were observed (a) SE image, (b) SE image, (c) SE image and (d) BSE image.**

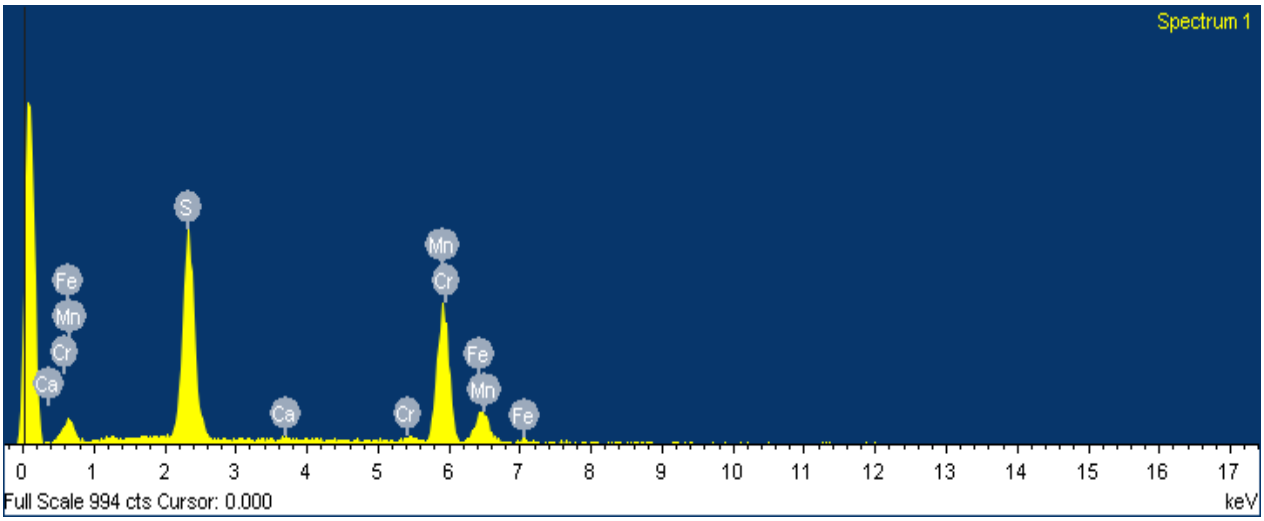

Figure 45: **SEM-EDS analysis of inclusions appearing in bright contrast [see Figure 44 (d)] indicated that they were manganese sulfide inclusions. These inclusions were observed on X20_210_540.**

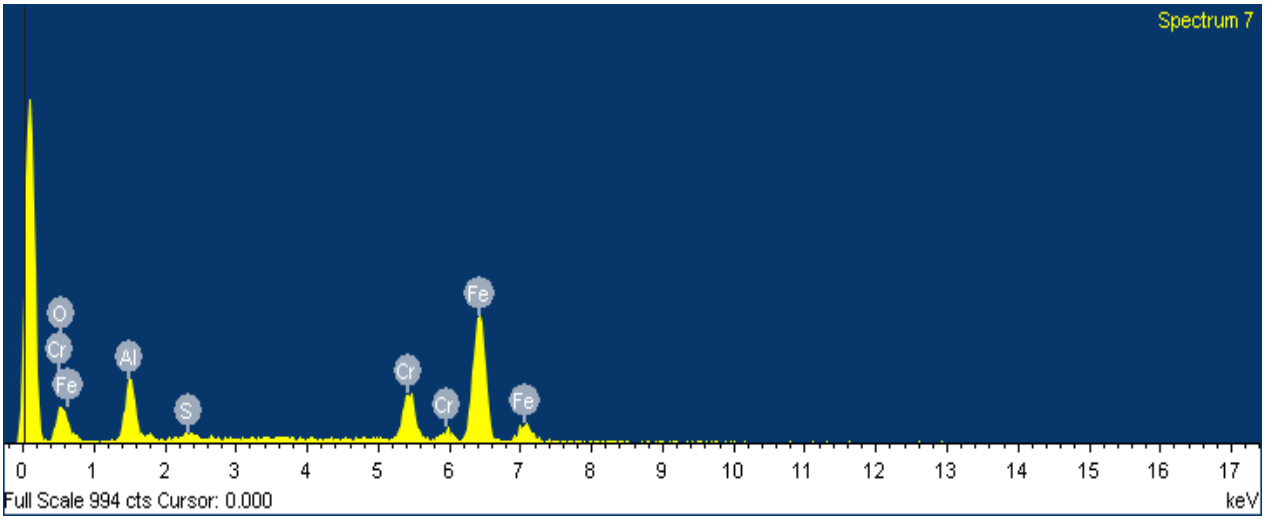

Figure 46: **SEM-EDS analysis of the inclusions observed on X20_210_540. Inclusions appearing in dark contrast [see Figure 44 (d)] were found to be aluminium oxide/sulfide inclusions.**

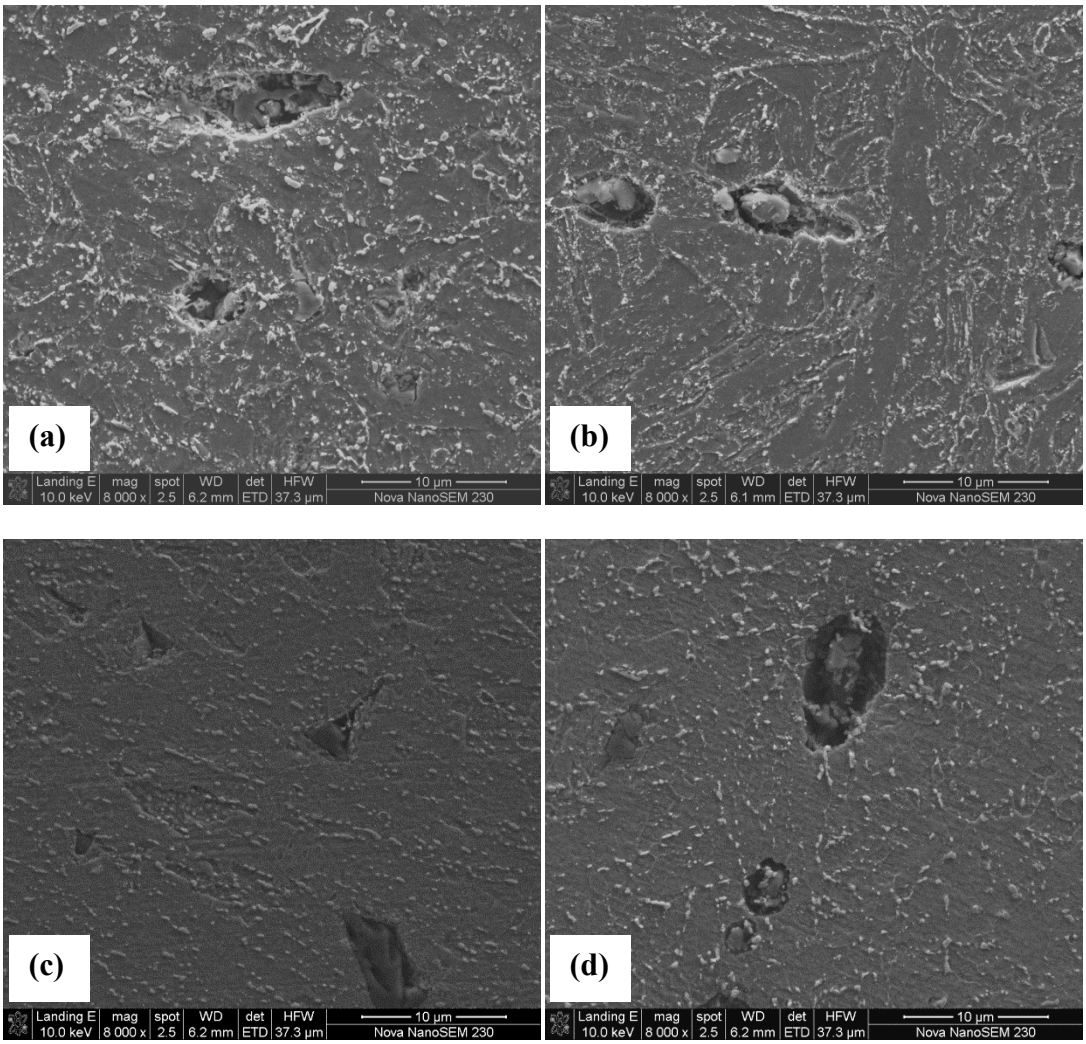

Figure 47: SEM-SE micrographs of X20_210_540 weldment and X20_210_540 simulated HAZ (a) weldment FGHAZ (b) weldment CGHAZ (c) simulated FGHAZ (d) simulated CGHAZ.

Figure 48 shows micrographs taken on X20_130_555 BM. Aligned aluminum oxide and manganese sulfide inclusions with perceptible damage were observed on X20_130_555 BM (see Figure 48, Figure 49 and Figure 50).

Analysis of X20_130_555 weldment and simulated HAZ indicated refinement in precipitate distribution in the HAZ relative to the BM (see Figure 51).

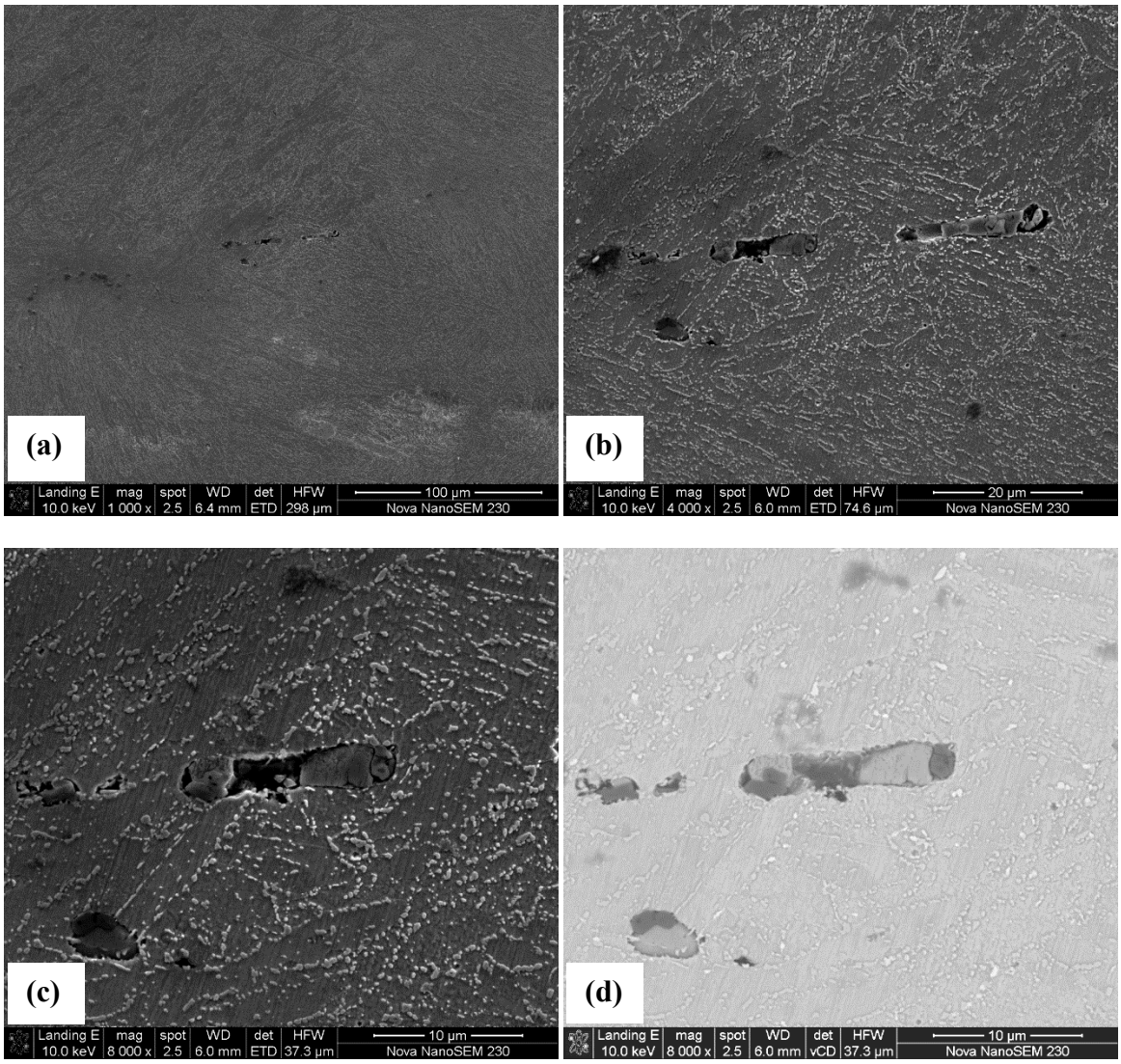

Figure 48: SEM micrographs of X20_130_555 BM. Coarse distribution of precipitates and strings of inclusions which had evidence of damage were noticed (a) SE image, (b) SE image, (c) SE image, and (d) BSE image.

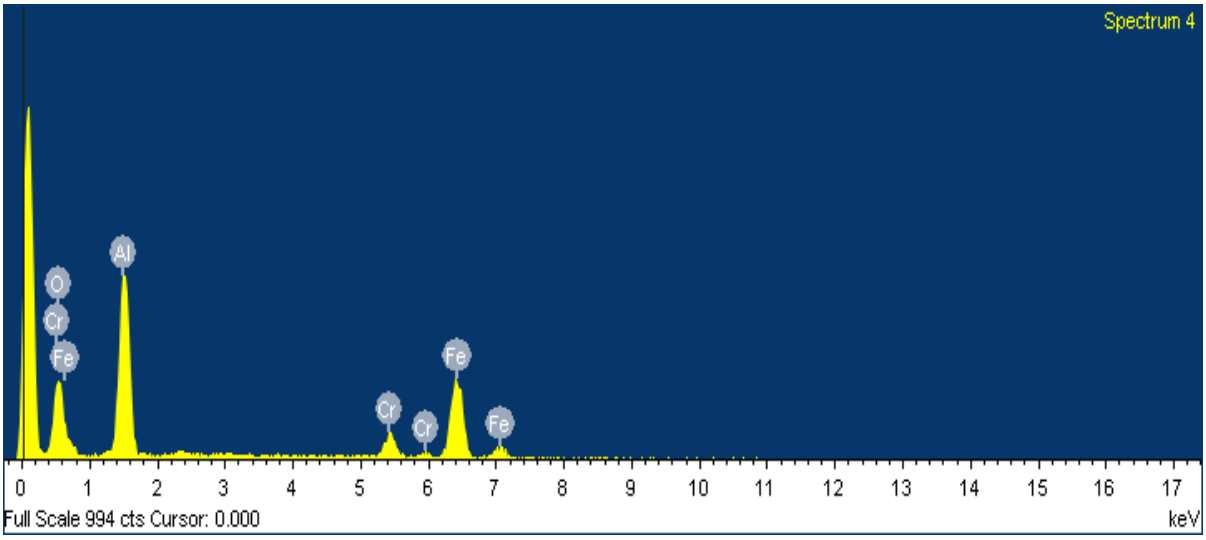

Figure 49: **SEM-EDS analysis of inclusion observed on X20_130_555. Inclusions which appeared in dark contrast were detected as aluminium oxides [see Figure 48 (d)].**

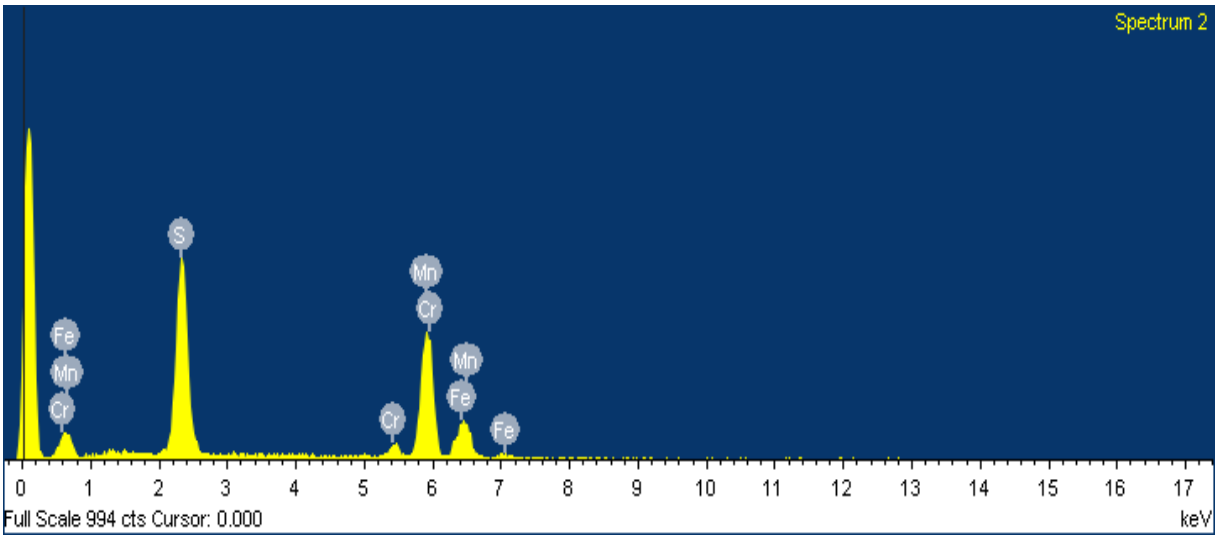

Figure 50: **SEM-EDS analysis of inclusions appearing in bright contrast [see Figure 48 (d)] indicated that they were manganese sulfides. These inclusions were noticed on X20_130_555.**

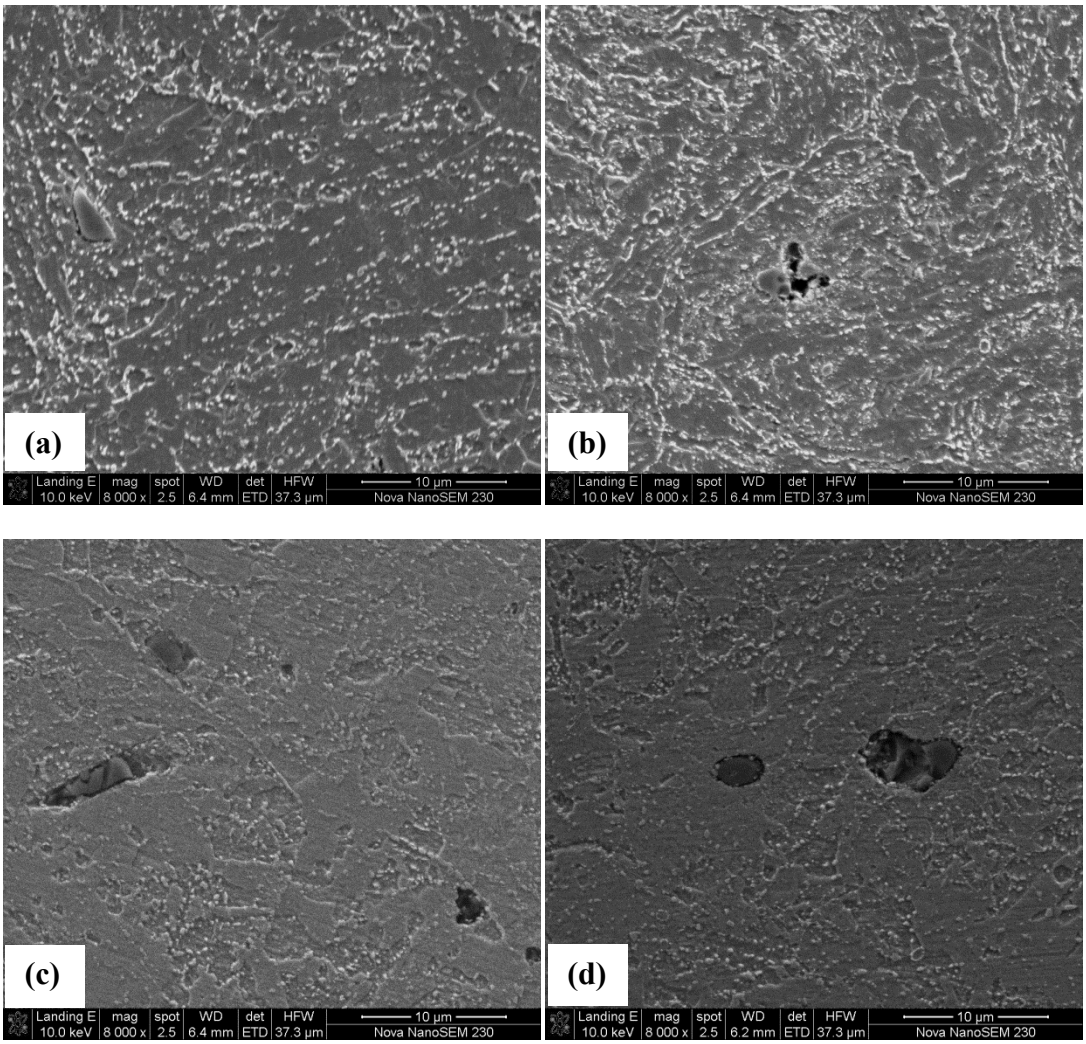

Figure 51: **SEM-SE micrographs of X20_130_555 weldment and X20_130_555 simulated HAZ (a) weldment FGHAZ (b) weldment CGHAZ (c) simulated FGHAZ (d) simulated CGHAZ. Increase in precipitate density was noticed in the HAZ.**

4.7. Microstructure: Grain Analysis

SEM-EBSD analysis was carried on New X20, X20_210_540 and X20_130_555 weldments and simulated HAZ. Figure 52 and Figure 53 show EBSD all-Euler (AE) angle maps for New X20 weldment (BM, FGHAZ, CGHAZ and WM) and New X20 simulated HAZ.

X20_210_540 weldment and simulated HAZ EBSD AE maps are shown in Figure 54 and Figure 55 respectively. The X20_210_540 BM had large grain size relatively to other regions of the weldment.

The EBSD results for X20_130_555 weldment and simulated HAZ are shown in Figure 56 and Figure 57, respectively.

Fine grained microstructure was noted in the FGHAZ of all weldments and simulated FGHAZ samples.

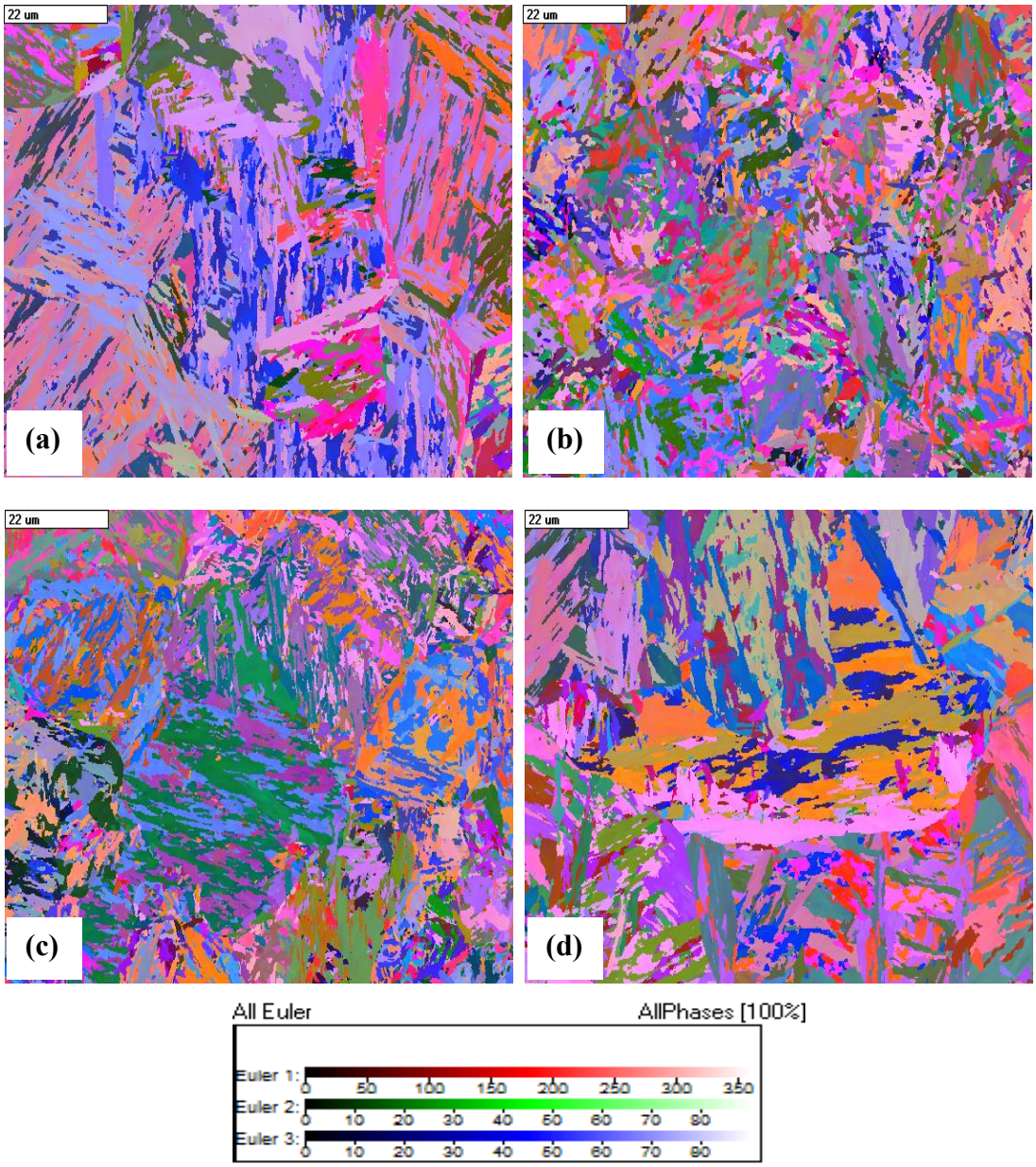

Figure 52: **SEM-EBSD AE angle maps of New X20 weldment (a) New X20 BM, (b) New X20 FGHAZ, (c) New X20 CGHAZ and (d) WM. Fine grain structure was noticed on the FGHAZ of New X20 weldment.**

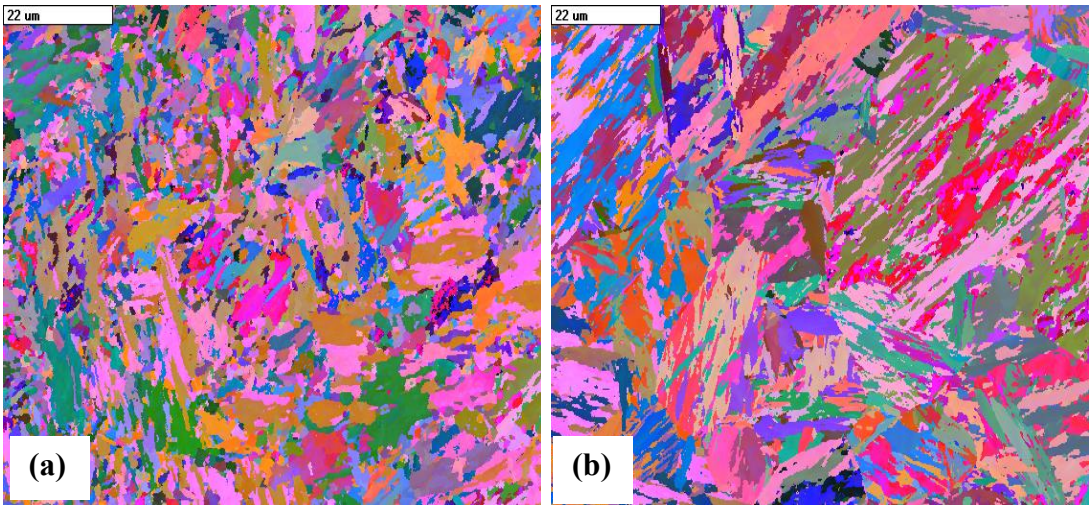

Figure 53: **SEM-EBSD AE angle maps showing New X20 simulated FGHAZ and simulated CGHAZ, respectively. Fine grain structure was noted on the simulated FGHAZ.**

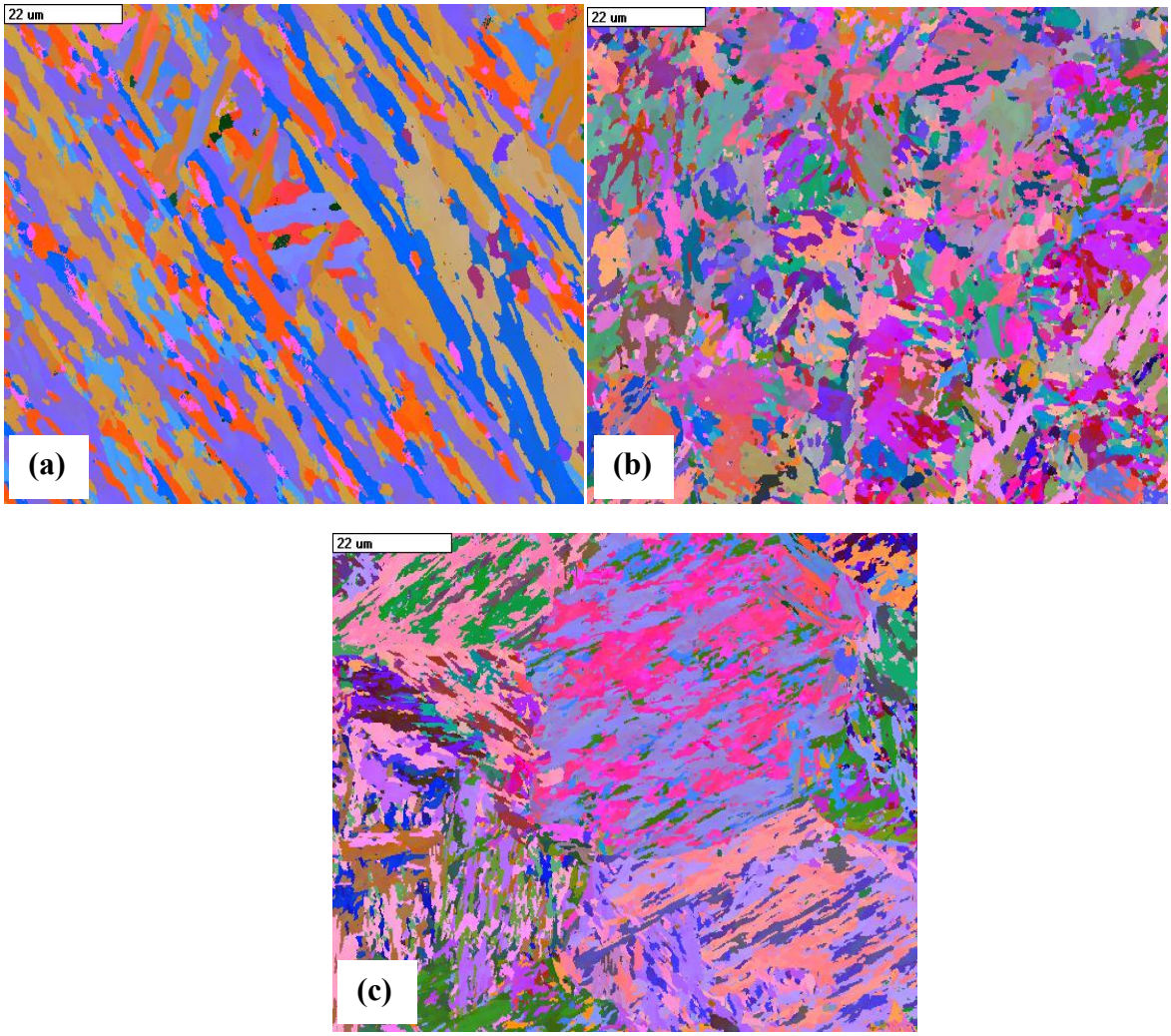

Figure 54: **SEM-EBSD AE angle maps of X20_210_540 weldment (a) BM, (b) FGHAZ, and (c) CGHAZ. Fine grained microstructure was noted in the FGHAZ of X20_210_540.**

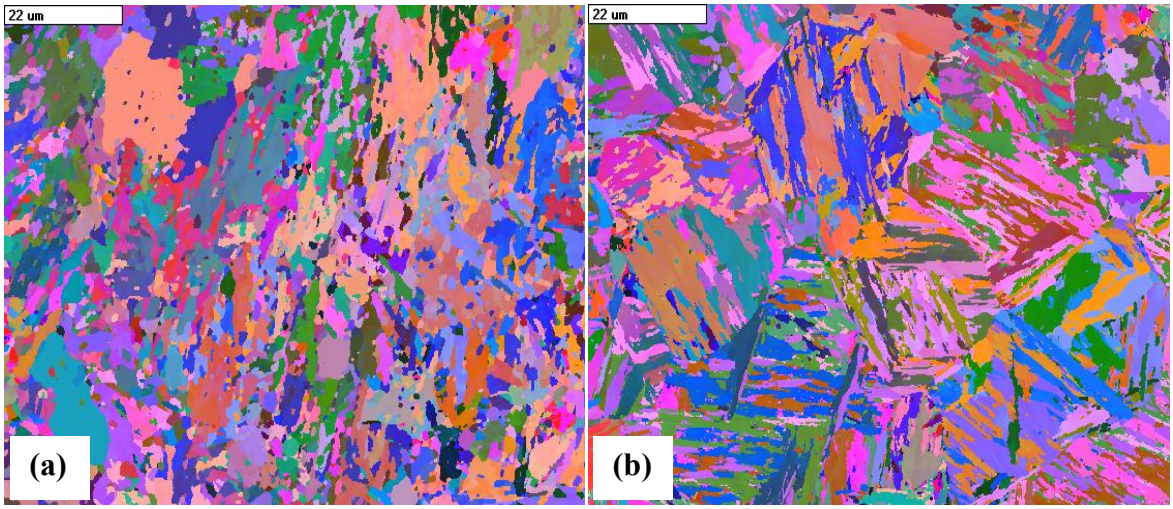

Figure 55: **SEM-EBSD AE angle maps showing X20_210_540 simulated FGHAZ and simulated CGHAZ, respectively. Fine grain structure was noted in the simulated FGHAZ.**

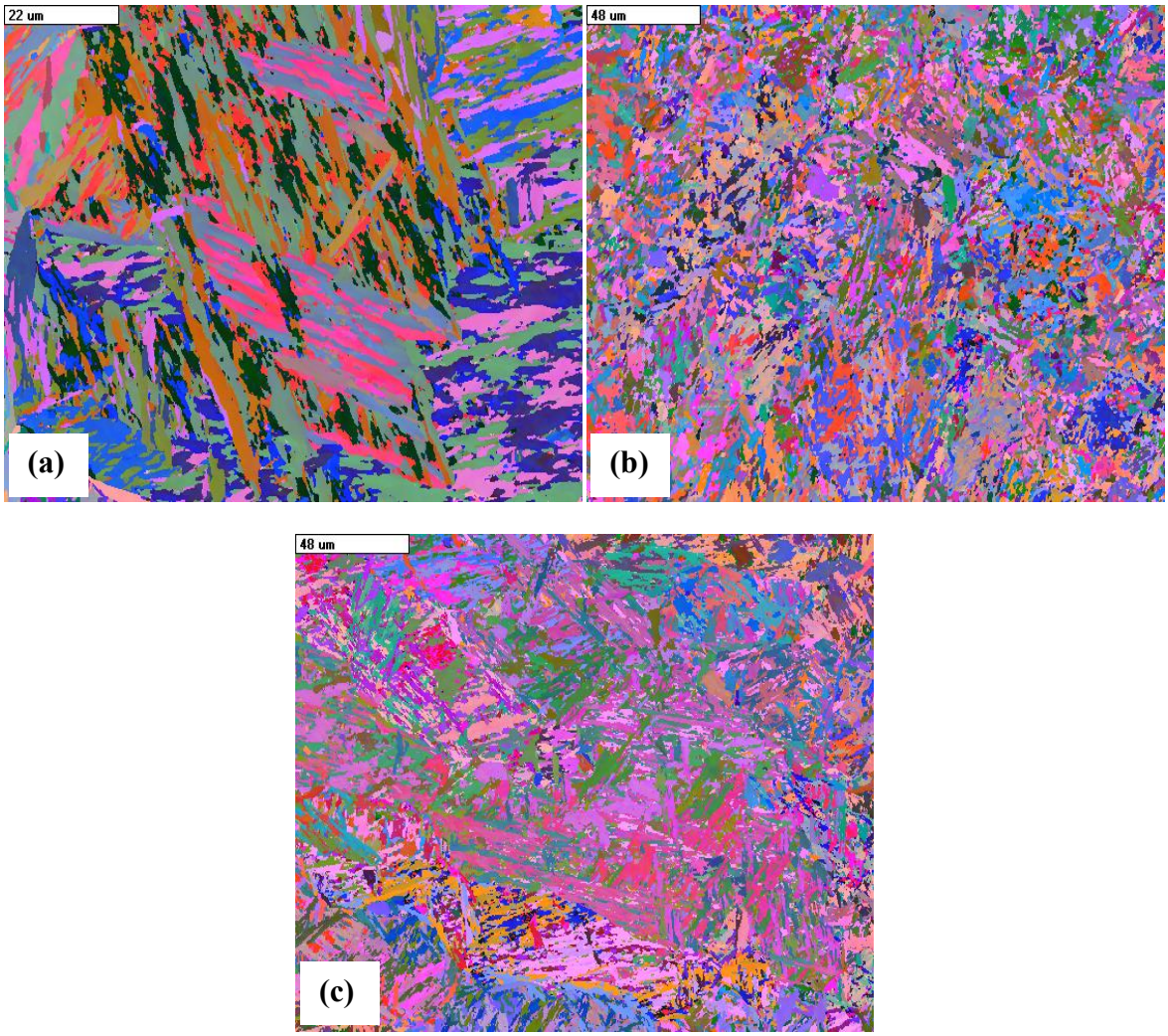

Figure 56: **SEM-EBSD AE angle maps of X20_130_555 weldment (a) BM, (b) FGHAZ, and (c) CGHAZ. Fine grained microstructure was noted in the FGHAZ of X20_210_540 weldment.**

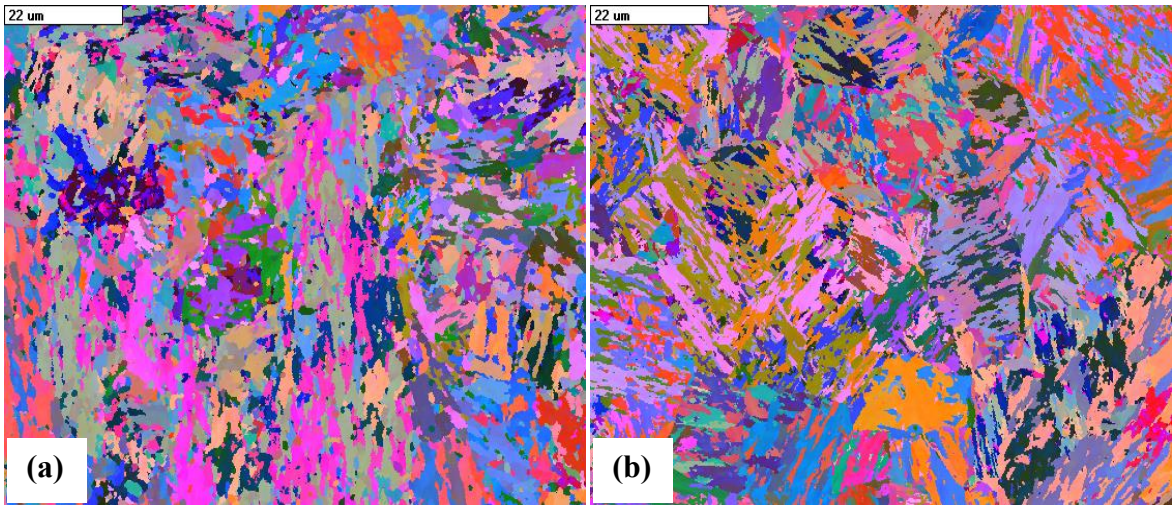

Figure 57: SEM-EBSD AE angle maps showing X20_130_555 simulated FGHAZ and simulated CGHAZ, respectively. Fine grained structure was noted in the simulated FGHAZ.

Figure 58 shows misorientation angle distribution for New X20 BM. Low angle grain boundaries (LAGB)/subgrains have misorientation angle distribution of 1.5-20° and high angle grain boundaries (HAGB)/grains have misorientation angle distribution above 20°.

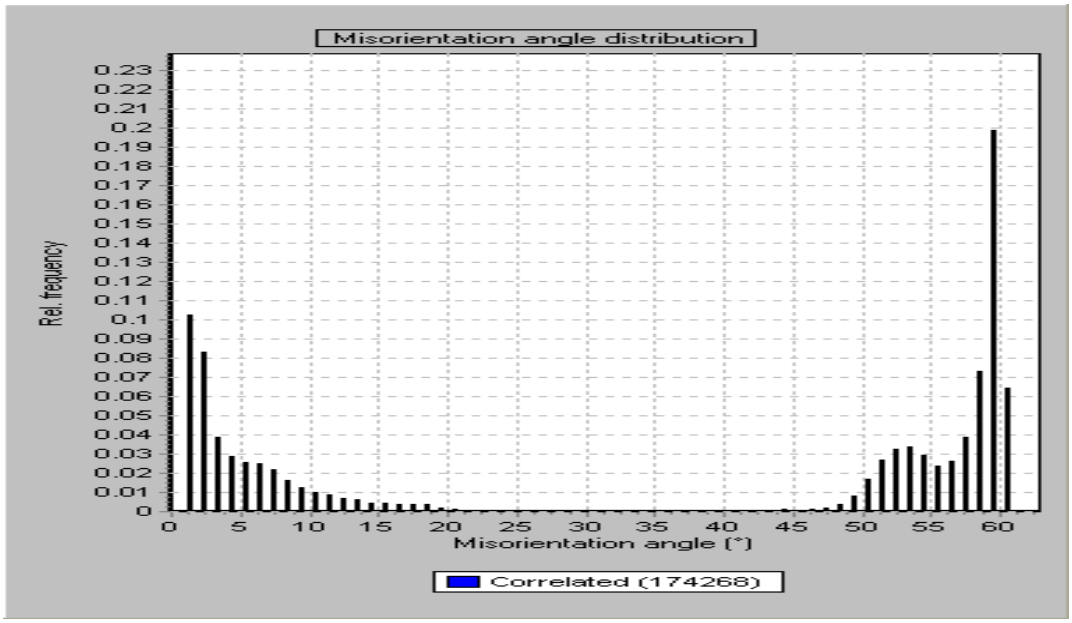

Figure 58: Misorientation angle distribution for New X20 BM. Low-angle grain boundaries (LAGB) have misorientation angle distribution between 1.5º and 20º and high-angle grain boundaries (HAGB) have misorientation angle distribution above 20º.

4.7.1. Subgrain Size and Grain Size Calculations

Subgrain sizes and grain sizes were calculated using Channel 5 program. These parameters were calculated for New X20 weldment, New X20 simulated HAZ, X20_210_540 weldment, X20_210_540 simulated HAZ, X20_130_555 weldment and X20_130_555 simulated HAZ. The data obtained during Channel 5 analysis had lower pixels data and this shifted the mean value calculated to lower values. The median diameter d_{50} was proposed to be a better representation of the data extracted from Channel 5 program. The median diameter was obtained at 50% accumulated area (as shown in Figure 59). The % accumulated area is calculated as follows:

$$Accumulated\ Area = \ Area_i + Area_{i+1}$$

$$i = 0 \ldots . . n$$

$$\%Accumulated\ Area = \frac{Accumulated\ Area}{Total\ Area}$$

The results obtained are shown in Table 24. The martensite lath size was generally low in the FGHAZ relative to the CGHAZ.

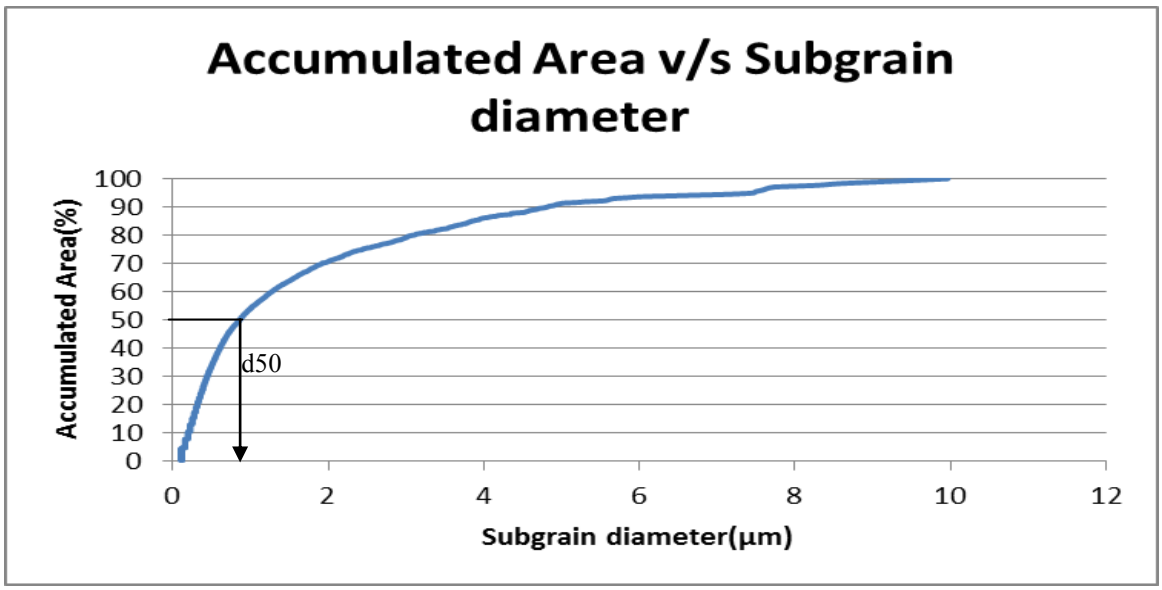

Figure 59: **Accumulated area v/s subgrain size plot for New X20 BM. Median diameter is obtained at 50% accumulated area.**

Table 24: **Measured martensite lath and subgrain median diameter d_{50}.**

Sample ID.	Martensite lath size(µm)	Subgrain size(µm)
New X20 BM	2.27	0.86
New X20 FGHAZ	2.00	0.95
New X20 CGHAZ	3.49	1.49
New X20 Simulated FGHAZ	6.23	1.67
New X20 Simulated CGHAZ	9.07	3.90
X20_210_540 BM	17.23	7.28
X20_210_540 FGHAZ	2.23	1.00
X20_210_540 CGHAZ	1.48	0.67
X20_210_540 Simulated FGHAZ	6.86	2.50
X20_210_540 Simulated CGHAZ	7.47	3.66
X20_130_555 BM	8.98	3.73
X20_130_555 FGHAZ	6.15	2.44
X20_130_555 CGHAZ	8.86	2.82
X20_130_555 Simulated FGHAZ	6.18	2.20
X20_130_555 Simulated CGHAZ	5.92	2.20
WM	3.44	1.48

The mean martensite lath size and mean subgrain size measurements were conducted using V-map 8. The equivalent circle diameter (ECD) was calculated for martensite lath and subgrains

and the results obtained are shown in Table 25. The calculated subgrain ECD was further used to calculate the subgrain strengthening effect as follows:

$$\sigma_{sg} = 10Gb/\lambda_{sg}$$

G = 65GPa, b = 2.5x10^{-10}m [21, 44].

The results obtained are shown in Table 25. Low subgrain hardening effect was noticed in the FGHAZ of X20 weldments relative to the CGHAZ.

Table 25: Calculated mean martensite lath size, mean subgrain size and subgrain hardening.

Sample ID.	Martensite lath size(µm)	Subgrain size(µm)	σsg (MPa)
New X20 BM	0.78	0.62	260
New X20 FGHAZ	0.90	0.70	232
New X20 CGHAZ	0.76	0.60	271
New X20 Simulated FGHAZ	1.00	0.52	312
New X20 Simulated CGHAZ	1.10	0.70	232
X20_210_540 BM	1.28	1.13	144
X20_210_540 FGHAZ	0.99	0.86	189
X20_210_540 CGHAZ	0.85	0.62	262
X20_210_540 Simulated FGHAZ	0.89	1.11	146
Duv_210_540 Simulated CGHAZ	0.80	1.14	142
X20_130_555 BM	1.07	0.80	203
X20_130_555 FGHAZ	1.78	1.28	127
X20_130_555 CGHAZ	1.43	1.05	155
X20_130_555 Simulated FGHAZ	1.01	0.71	229
X20_130_555 Simulated CGHAZ	0.86	0.55	296
WM	0.98	0.83	195

4.8. Microstructure: Precipitates Analysis

New X20 weldment, New X20 simulated HAZ, X20_210_540 weldment, X20_210_540 simulated HAZ, X20_130_555 weldment and X20_130_555 simulated HAZ were analysed using TEM. The samples were analysed to characterize precipitate evolution during welding.

Figure 60 shows bright-field and dark-field TEM micrographs of New X20 BM. Precipitates were noted within subgrains and on subgrain boundaries. Chemical composition of precipitates was confirmed by EDS analysis (see Figure 61 and Figure 62). Chromium rich $M_{23}C_6$ precipitates were found at subgrain boundaries and vanadium rich MX precipitates were found on the subgrain boundaries and within subgrains. Similar precipitates were detected on X20_210_540 and X20_130_555 weldment and simulated HAZ.

Evolution of $M_{23}C_6$ precipitates was studied in different regions of New X20 weldment and the results obtained are showed in Figure 63. Low precipitate density was noted in the FGHAZ of New X20 weldment. Similar results were observed in the simulated HAZ.

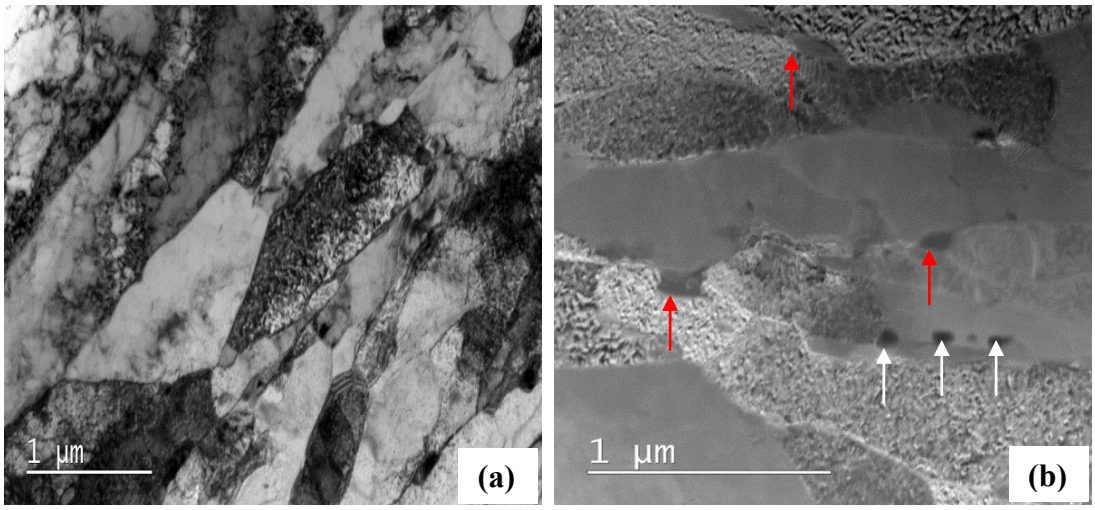

Figure 60: TEM micrographs of New X20 BM (a) bright-field (b) dark-field. Chromium rich $M_{23}C_6$ precipitates were observed on sub-grain boundaries (shown with red arrows) and MX precipitates (shown with white arrows) were observed on sub-grain boundaries and within sub-grains.

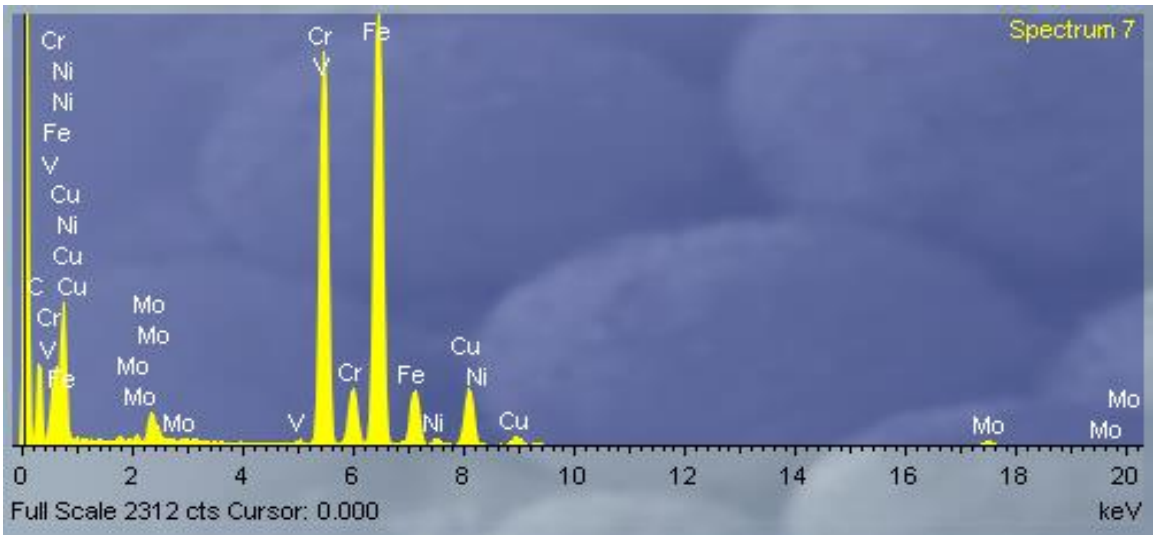

Figure 61: **TEM-EDS analysis of precipitates observed on the subgrain boundaries. The precipitates were confirmed to be chromium rich $M_{23}C_6$.**

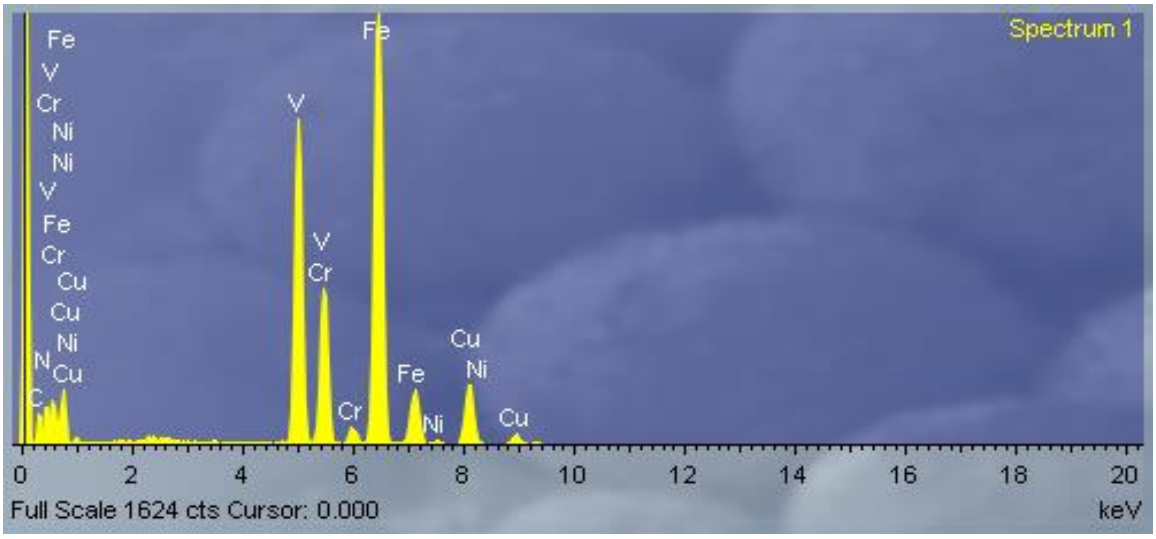

Figure 62: **TEM-EDS analysis of precipitates observed within subgrains. The EDS analysis results indicated that the precipitates were MX precipitates, which are rich in vanadium.**

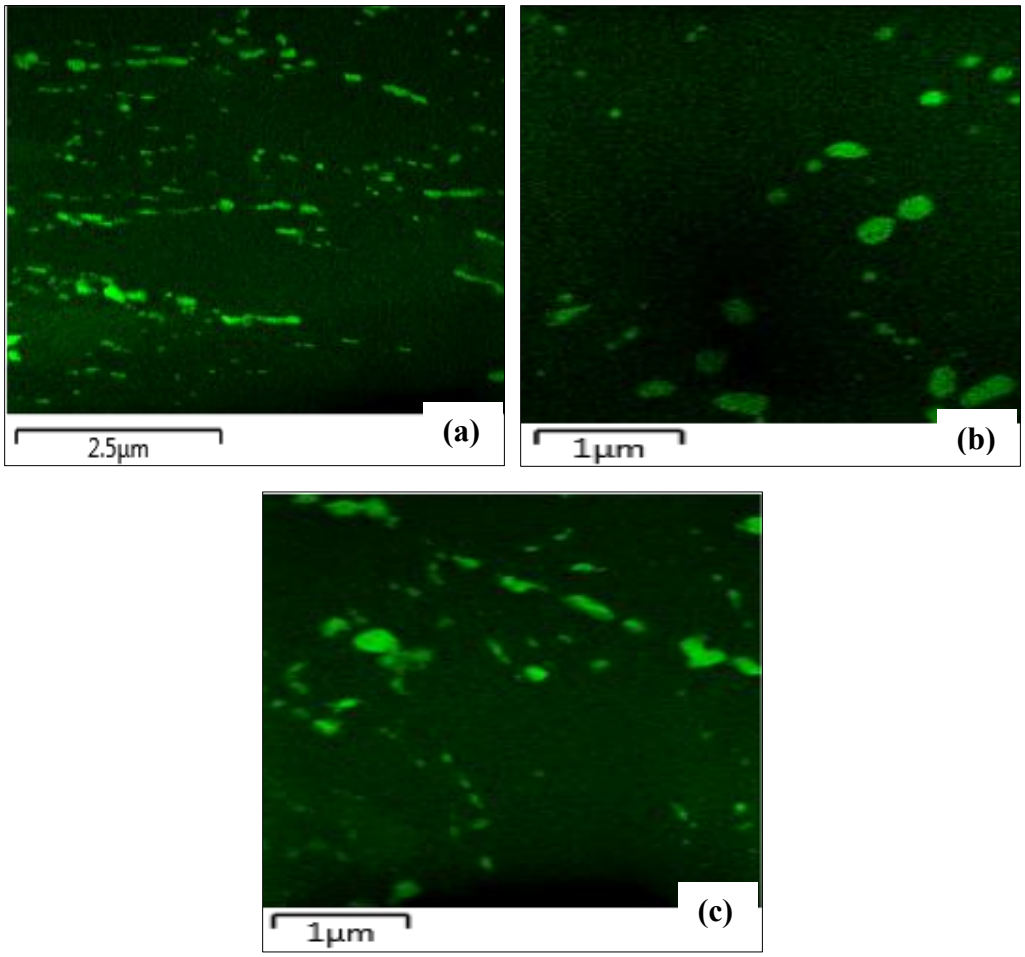

Figure 63: Energy filtered TEM (EFTEM) micrographs showing $M_{23}C_6$ precipitates in different regions of the New X20 weldment (a) BM (b) FGHAZ (c) CGHAZ. Low precipitate density was noted in the FGHAZ.

$M_{23}C_6$ precipitates evolution was also studied in X20_210_540 weldment and X20_130_555 weldment and the results obtained are shown in Figure 64 and Figure 65, respectively. High precipitate density and fine distribution of precipitates was noted in the CGHAZ of both weldments. Similar results were observed in X20_210_540 simulated HAZ and X20_130_555 simulated HAZ

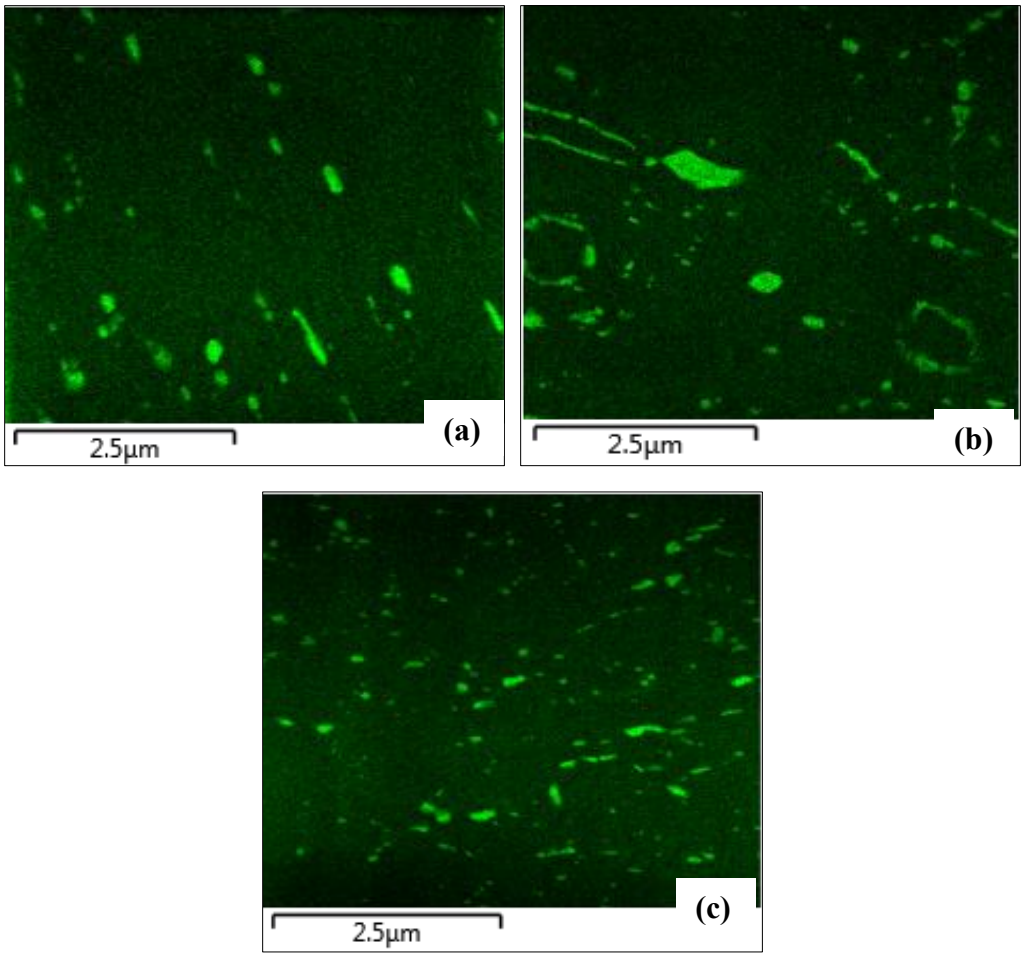

Figure 64: **EFTEM micrographs showing $M_{23}C_6$ precipitates in different regions of X20_210_540 weldment (a) BM (b) FGHAZ (c) CGHAZ. High precipitate density was noticed in the CGHAZ.**

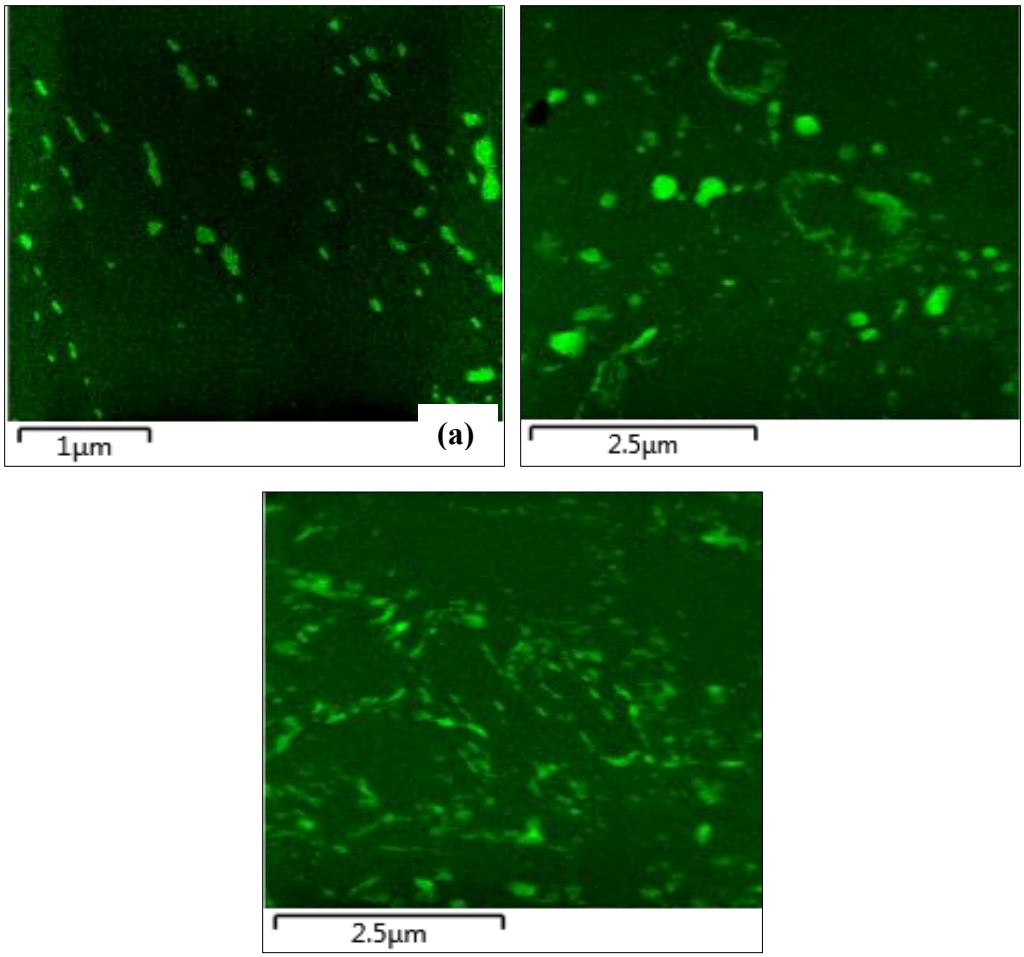

Figure 65: EFTEM micrographs showing $M_{23}C_6$ precipitates in different regions of the X20_130_555 weldment (a) BM (b) FGHAZ (c) CGHAZ. Significantly high precipitate density was noted in the CGHAZ.

Quantitative study of precipitates on the weldments and simulated HAZ samples was conducted using Image J program. Precipitates maps obtained during TEM analysis were used in the program to calculate the equivalent area of precipitates. This data was then used to calculate the equivalent circle diameter (ECD) of precipitates. Stereological correlations were used to calculate the mean diameter, phase fraction and interparticle spacing from calculated ECD (see section 2.5 for detailed information). Stereological equations used to calculate precipitates parameters are as follows:

$\bar{d} = \frac{\sum_i d_m w_{Sample,i}}{\sum_i w_{Sample,i}}$ - Mean diameter

$f_V = \frac{1}{V_{Sample}} \sum_i \frac{d_i^3}{6} \frac{t_i}{t_i + d_i}$ - Phase fraction

$\lambda = \sqrt{\frac{\ln(3)}{2\pi \sum_i n_{V,i}} + (2r_A)^2} - 2r_A$ - Interparticle spacing

The Orowan stress was calculated as follows:

$$\sigma_{or} = (\alpha . M . G . b)/\lambda$$

α = 0.8, M = 3, G = 65GPa and b = 2.5×10^{-10}m [21, 44].

A summary of precipitate parameters calculated is shown in Table 26. Low Orowan back-stress values were calculated in the FGHAZ (weldment and simulated HAZ) relative to the CGHAZ and this was due to high precipitate inter-particle spacing in the FGHAZ.

Table 26: Summary of parameters calculated $M_{23}C_6$ precipitates.

Sample ID.	d_{mean} (nm)	fV (%)	λ (nm)	σ_{or} (MPa)	No. of Precipitates Analyzed
New X20 BM	98	4.2	226	173	101
New X20 FGHAZ	124	4.1	295	132	32
New X20 CGHAZ	112	5.9	221	177	63
New X20 Simulated FGHAZ	148	3.7	359	109	273
New X20 Simulated CGHAZ	111	2.9	327	120	725
X20_210_540 BM	120	2.60	381	102	46
X20_210_540 FGHAZ	112	5.0	270	144	87
X20_210_540 CGHAZ	86	2.6	249	156	117
X20_210_540 Simulated FGHAZ	168	1.9	742	55	110
X20_210_540 Simulated CGHAZ	125	2.6	387	103	180
X20_130_555 BM	95	2.8	243	160	60
X20_130_555 FGHAZ	114	4.5	279	140	110
X20_130_555 CGHAZ	110	5.7	219	178	168
X20_130_555 Simulated FGHAZ	129	1.8	622	67	184
X20_130_555 Simulated CGHAZ	128	3.2	398	100	266
Weld-Metal	61	2.2	222	176	230

The $M_{23}C_6$ precipitate phase fraction evolution in an X20 steel was evaluated using the MATCALC program. The phase fraction evolution was assessed with respect to temperature and the results obtained are shown Figure 66. A maximum of 4.5% phase fraction of $M_{23}C_6$

precipitates is obtained in an X20 steel and this is stable until temperatures above 550°C, were the value start dropping rapidly.

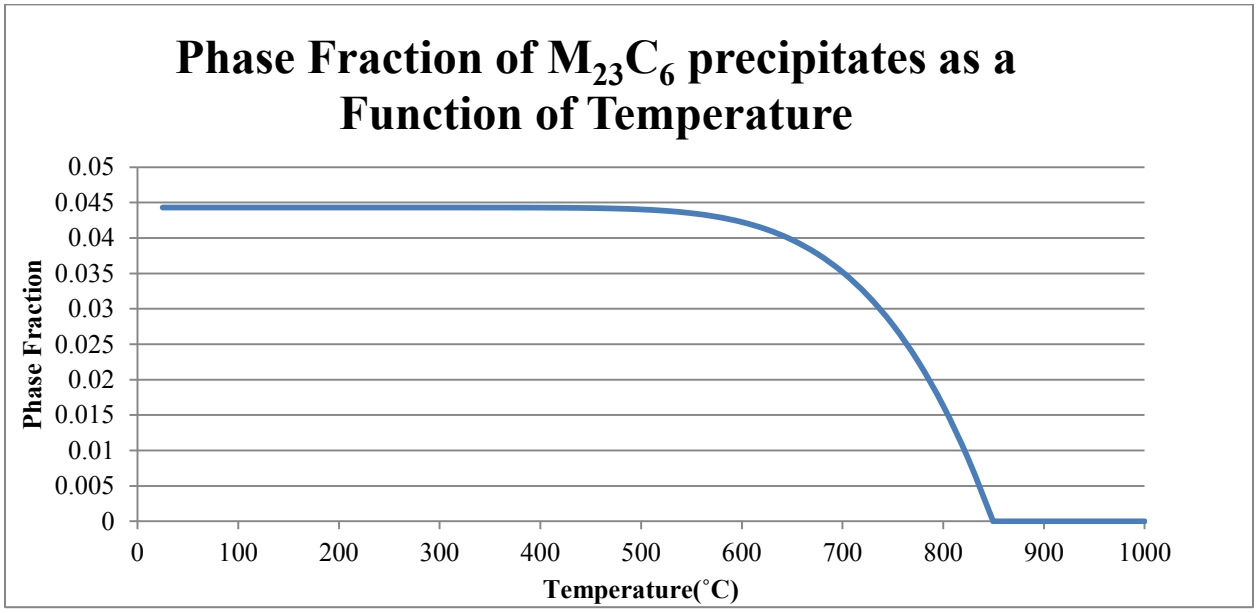

Figure 66: **Phase fraction of $M_{23}C_6$ as a function of temperature for X20 steel. The phase fraction was calculated using MATCALC program. Maximum phase fraction of 0.045 was calculated and this starts decreasing rapidly at temperatures above 550°C.**

5. Discussion

5.1. Life Assessment for Service Exposed X20 Steels

Life estimates conducted for X20 steel base materials using master curves and creep damage models indicate the following:

- Life exhaustion of 26/12% and 52/12% (-20% of P6525 mean/P6525 mean) for X20_210_540 BM and X20_130_555 BM, respectively.
- Life exhaustion of 69/54% and 84/44% (using maximum/average creep void density) for X20_210_540 BM and X20_130_555 BM, respectively.
- The remaining life calculated from creep damage models indicated a life in excess of 18 years if the average creep damage is used. The life estimates conducted using maximum creep void density indicated that X20_130_555 BM has reached end of life, while X20_210_540 had 10 years of life.

5.2. Evolution of Hardness

Hardness measurements were conducted on the X20 weldments (BM, HAZ and WM) and simulated HAZ specimens to assess evolution of mechanical properties during welding.

Low hardness values were measured in the FGHAZ (weldment and simulated) of New X20 relative to the CGHAZ (weldment and simulated). The low hardness values were in agreement with low Orowan back-stress values calculated for the FGHAZ relative to the CGHAZ.

New X20 simulated FGHAZ and CGHAZ had low Orowan back-stress values compared to the weldment FGHAZ and CGHAZ, but had similar hardness values. The difference in Orowan back-stress values can be explained by different TEM sample preparation methods used. The TEM samples for the weldments were prepared using FIB-SEM which yields relatively thin specimens, allowing features to be resolved with less difficulty, on the contrary, the samples prepared from the simulated HAZ were relatively thick and this resulted in poor resolution of features.

The hardness measured in the FGHAZ of New X20 was similar to that of the BM, but the FGHAZ had lower Orowan back-stress values compared with the BM. Similar hardness values could have resulted from rapid heating and cooling heat-treatment that the FGHAZ undergoes

during welding, which results in formation of a martensitic microstructure with similar hardness as the BM.

High hardness values were measured in X20_210_540 FGHAZ (weldment and simulated) relative to the BM. The increase in hardness was correlated by high Orowan back-stress value in the FGHAZ of X20_210_540 weldment. The back-stress values calculated in the simulated FGHAZ was low and this was due to interference of the matrix during TEM analysis of samples prepared using the conventional TEM sample preparation method.

Hardness profiling conducted on X20_130_555 weldment and simulated HAZ indicated low hardness values in the FGHAZ (weldment and simulated) compared to the CGHAZ (weldment and simulated). The FGHAZ had low Orowan back-stress values compared to the CGHAZ, which is in agreement with measured hardness values.

The hardness measured in the X20_130_555 FGHAZ was similar to that of the BM and this was not in agreement with the calculated Orowan back-stress. Low Orowan back-stress values were calculated in the FGHAZ relative to the BM. Similar hardness values measured in these two regions could have resulted from the heat-treatment that is experienced in the FGHAZ during welding.

The hardness measurements conducted on the BM of each weldment indicated a decrease in hardness after service exposure. X20_210_540 BM had hardness values below the specification requirements for X20 steel. The decrease in hardness can be correlated with the decrease in precipitate strengthening during creep exposure as shown in Table 26.

The FGHAZ of all the weldments showed low hardness values relative to the CGHAZ. The low hardness measured in the FGHAZ was in good agreement with low Orowan back-stress values in the FGHAZ relative to the CGHAZ.

5.3. Creep Rupture Tests and Life Estimates for X20 Steel WJ's

New X20 – X20_210_540 weld-joint and New X20 – X20_130_555 weld-joint were used to conduct cross-weld creep rupture test at 650˚C using a reference 63MPa. The weld-joints indicated rupture in the FGHAZ of creep aged X20 steels (X20_210_540 and X20_130_555). Significant void formation was perceptible in the region of fracture as shown in Figure 32 and Figure 34 i.e. type IV failure. Similar failure was reported by other researchers (Francis 2006).

The FGHAZ of all the weldments had a coarse distribution of $M_{23}C_6$ precipitates relative to other regions of the weldments (exception being the X20_210_540 where the FGHAZ had a finer precipitate distribution compared to the BM). Coarse distribution of precipitates leads to fewer obstacles for dislocation movement during creep and promotes recovery of the matrix.

The FGHAZ of the weldment and simulated HAZ had a fine grained microstructure compared to other regions of the weldments (see Figure 52, Figure 53, Figure 54, Figure 55, Figure 56 andFigure 57). The fine grained microstructure in the FGHAZ promotes diffusion of vacancies during creep exposure and leads to enhanced diffusional creep.

The FGHAZ of New X20 weldment had slightly low Orowan back-stress value and small grain size relative to the FGHAZ of other weldments (X20_210_540 and X20_130_555) as shown in Table 26 and Table 25, respectively. The low precipitate strengthening and the small grain size in the New X20 FGHAZ, meant that the New X20 weldment FGHAZ had poor creep properties relative to the FGHAZ of X20_210_540 weldment and X20_130_555 weldment, yet the weld-joints failed in the FGHAZ of X20_210_540 weldment and X20_130_555 weldment. This indicates that prior creep damage had an influence on creep behaviour of weldments.

New X20 - X20_130_555 weld-joint had a low creep rupture time relative to New X20-X20_210_540 weld-joint as shown in Table 18 and this can be related to high creep damage observed on X20_130_555 prior welding.

Creep life estimates conducted for X20_210_540 weldment and X20_130_555 weldment using creep damage models in conjunction with master curves indicated the following:

- Estimated exhaustion levels of 69/54% (maximum/average) in the X20_210_540 BM and 84/44% (maximum/average) in the X20_130_555 BM where welds were made.

- The creep rupture test results (650ºC, 63MPa) for New X20 to X20_210_540 and New X20 to X20_130_555 were within the predicted scatter-band for a weldment (WRF=70%) with creep aged BM. The results also indicated that life estimates conducted using maximum creep damage are over-conservative on failure time predictions while life estimates conducted using average creep void density gave realistic failure time.
- Weldments RLE conducted at operating conditions (540ºC) indicated that X20_210_540 weldment can still be managed within the Eskom outage philosophy (must be replaced in 3 to 6 years or 12 to 15 years if maximum or average creep damage is used, respectively).
- RLE for X20_130_555 weldment (at 540ºC) indicated that the weldment cannot be managed within the outage philosophy if maximum creep void density is used to conduct life estimates, while life estimates conducted using average creep void density indicated that the component must be replaced in 9 – 12 years.
- The RLE for X20 steel weldments conducted at operating conditions, using the average creep damage indicate that X20_210_540 and X20_130_555 weldment can safely be managed within an inspection window of 3 years.
- Although Eskom weldability limits are set at <100voids.mm^2 on X20 steel aged for more than 100kh, in risk applications weldability could be considered acceptable despite damage of 95 – 250 voids/mm^2 and 70 – 485 voids/mm^2. The voids were relatively fine and not homogeneously distributed. Exhaustion levels can be used for weldability limits rather tvoid count.

5.4. Evolution of Hot Strength

Mechanical property evaluation conducted at X20 design temperature (545˚C) on the BM and simulated HAZ showed low yield strength values and low hot strength values in the simulated FGHAZ relative to the CGHAZ and the BM as shown in Table 23. The decrease in hot strength can be explained by coarse distribution of $M_{23}C_6$ precipitates and fine grained microstructure observed in the FGHAZ. Coarse distribution of precipitates leads to few obstacles to retard dislocation movement during plastic deformation and fine grained microstructure promotes diffusion of vacancies during high temperature deformation. Similar mechanical properties were obtained at elevated temperature for X20 steel (Tuma 2009).

5.5. Evolution of Creep Voids

New X20 BM, X20_210_540 BM and X20_130_555 BM were investigated with the SEM to characterize creep voids evolution. Creep voids were observed on service exposed samples. Some damage was located on manganese sulphide and aluminium oxide inclusions. The damage observed on MnS inclusions could have been introduced during the hot rolling process while that observed on the aluminium oxide inclusion are possibly due to pile up of vacancies, leading to formation of voids. Similar damage was observed on MnS inclusions on a virgin X20 steel (Aghajani 2009).

X20_210_540 had relative small inclusions (≤5µm) with damage, while inclusions observed on X20_130_555 were relative large (≤10µm). The sizes of inclusions were different because the two steels were not cast from the same ingot.

5.6. Evolution of Precipitate Parameters

New X20 (weldment and simulated HAZ), X20_210_540 (weldment and simulated HAZ) and X20_130_555 (weldment and simulated HAZ) were analysed to characterize precipitate evolution during welding. The results obtained for the analysis are shown in Table 26

The precipitate evolution in New X20 weldment and simulated HAZ indicated coarse precipitate distribution in the FGHAZ relative to the CGHAZ and the BM. Coarse distribution of precipitates in the FGHAZ was due to incomplete dissolution of precipitates during welding. The HAZ experiences rapid heating during welding and hence requires temperatures well above the upper critical temperature for complete dissolution of precipitates to occur. The FGHAZ experiences temperatures in the range of 820ºC – 1000ºC, resulting in incomplete dissolution of precipitate and coarsening during cooling.

X20_210_540 FGHAZ (weldment) indicated a refinement in precipitate strengthening relative to the BM. Finely distributed precipitates were observed in the FGHAZ of this X20 steel and this was due to dissolution of some of the precipitates and nucleation of finer precipitates during welding. The new finely dispersed carbide features lower interparticle distance and thus higher precipitate strengthening relative to the BM. The FGHAZ however, still had coarse distribution of $M_{23}C_6$ precipitates relative to the CGHAZ. The CGHAZ experiences temperatures well above

the A_{c3}, resulting in complete dissolution of precipitates and fine nucleation of $M_{23}C_6$ precipitates during welding.

The FGHAZ of X20_130_555 (weldment and simulated) had coarse distribution of precipitates relative to other regions of the weldment.

The BM of New X20, X20_210_540 and X20_130_555 were analysed to characterize precipitate evolution during service exposure. The results obtained indicated an increase in $M_{23}C_6$ precipitate interparticle spacing after creep exposure and this consequently led to a decrease in precipitate strengthening as shown in Table 26. Similar results were reported by other researchers (Aghajani 2009; Panait 2010).

The FGHAZ of all the weldments and simulated HAZ samples had a higher interparticle spacing relative to the CGHAZ. Some of the $M_{23}C_6$ precipitates remain undissolved in the matrix of the part of the HAZ which undergoes a welding thermal cycle of 820ºC – 1000ºC, and coarsen in that temperature range. Other scientist reported similar behavior (Tian 1991; Xue 2009).

The precipitate density in the simulated HAZ samples was low as shown in Table 26 and this was due to interference of the matrix with TEM signal, hence not being able to resolve other precipitates. The TEM specimens for the simulated HAZ were prepared by conventional TEM sample preparation method, which yields thick samples compared to the samples prepared with the FIB equipment.

The precipitate strengthening in the FGHAZ was always found lower than in the CGHAZ. Thus the weaker part of the welding can be considered the FGHAZ, as long as precipitates are concerned. However in the creep loaded sample (X20_210_540), the precipitate strengthening in the FGHAZ was higher than in the BM. Yet we have observed creep failure in the FGHAZ of X20_210_540 weldment. This means that the precipitate state immediately after welding is not the one which is relevant for long term creep strength. The finer grains in the FGHAZ are going to promote diffusional creep and increase number of diffusional paths, which is going to lead to accelerated coarsening of precipitates. Therefore, on the long run, the precipitates in the FGHAZ will coarsen a lot faster compared to the precipitates in the creep aged BM.

5.7. Evolution of Grains

Fine grained microstructure was generally noticed in the FGHAZ relative to the CGHAZ (see Figure 52, Figure 53, Figure 54, Figure 55, Figure 56 and Figure 57). The decrease in grain size was due to exposure to temperatures just above the upper critical temperature during welding, which leads to restricted growth of austenite grains and subsequent nucleation of fine grained martensite within small prior austenite grains (Easterling 1992).

Diffusion distances are shorter in fine-grained materials (Cambridge 2013), and this indicates that the FGHAZ of the weldment will experience enhanced diffusional creep during creep exposure. Enhanced diffusional creep will contribute to the decline of creep properties in the FGHAZ.

There is potential of grain boundary sliding (GBS) due to finer grains in the FGHAZ but sufficient literature is not yet available on the role of GBS in this specific steels.

6. Conclusions

1. The decrease in mechanical properties in the FGHAZ was due to coarse distribution of $M_{23}C_6$ precipitates and the fine grained microstructure which results after the welding process. The effective diffusion coefficient is higher in this region due to small grain size and fine particle distribution is required to block recovery. The FGHAZ has relatively coarse distribution of $M_{23}C_6$ precipitates and this result in enhanced recovery of the microstructure in this region and subsequent creep failure.

2. The prior creep damage had an influence on the creep properties of the weldment and this was supported by rupture in the FGHAZ of weldments with prior creep damage. The influence of prior creep damage on the service behaviour of the weldments should be studied in detail, and this can be done by conducting creep rupture tests at different temperatures and evaluating the damage progression in the weldment with prior creep damage and the weldment with no damage. The damage progression data can be used to model creep damage propagation in a weldment and modify life estimates models for weldments with prior creep damage.

3. Hardness tests and tensile tests conducted on the BM of X20 steels indicated a decrease in mechanical properties after creep exposure and this was due to recovery of microstructure and coarsening of precipitates experienced during service exposure.

4. Deterioration in mechanical properties was evident on New X20 steel FGHAZ relative to the BM and CGHAZ. This was due to an increase in $M_{23}C_6$ precipitates interparticle spacing and decrease in grain size which took place during welding.

5. X20_210_540 FGHAZ showed similar loss in mechanical properties relative to the CGHAZ and this was attested by coarse distribution of $M_{23}C_6$ precipitates and fine grain size in this region. Improvement in hardness was evident in the FGHAZ relative to the BM and this was due to refinement in precipitate distribution which took place during welding.

6. Low hot strength values were measured in the simulated FGHAZ of X20_210_540 relative to the BM, and this was due to finer grained microstructure in the FGHAZ, which enhanced diffusion of vacancies during high temperature deformation. Despite not being considered in this thesis, the impact of GBS shall not be left unmentioned, but it is addressed to follow-up projects. Additional reason is that GBS can only be considered within the framework of creep rate modelling, not backstress. It is therefore out of the scope of this work.

7. X20_130_540 FGHAZ had low Orowan back-stress values and fine grained microstructure relative to the CGHAZ and BM and this resulted in poor mechanical properties in this region.

8. Industrial creep damage models can potentially be used to set weldability limits for X20 steel. Welding of creep damaged X20 steel with average creep void density of 178voids/mm^2 and 140voids/mm^2 is possible for X20 steel with exhaustion estimated at approximately 54% (aged for more than 200kh) and 44% (aged for more than 100kh) respectively.

References

Abe, F. (2008). International Journal of Materials Research **99**: 387-394.

Abe, F. (2008). Sci. Technol. Adv. Mater. **9**(013002).

Abe,F. (2008). Creep-resistant Steel. CRC Press Cambridge, England.

Adonyi, Y. (2006). "The Affected Zone Characterization by Physical Simulations." Welding Journal: 42 - 47.

Aghajani, A. (2009). Acta Materialia **57**: 5093 - 5106.

Aghajani, A. (2009). Scripta Materialia **91**: 1068 - 1071.

Aghajani, A. (2009). Evolution of Microstructure during Long-term Creep of a Tempered Martensitic Ferritic Steel, Bochum. **Phd**.

AGO, I. C. (2009). Efficiency Standards for Power Generation. S. K. M. P. Ltd. Canberra, Australia.
.

Anand, A. (2006). 23rd Annual Pittsburgh International Coal Conference. Pittsburgh.

ARC Creep Deformation in Materials

Armaki, H. G. (2011). Journal of Nuclear Materials **416** 273 - 279.

ASME (2008). 2007 ASME Boiler and Pressure Vessel Code.

Barkar, T. (2005). Mater. Sci. Eng. A **395**: 110-115.

Barraclough, D. R. (1985). Materials Science & Technology **1**.

Baumann, K. (1968). Internationale Energiekonferenz Laussane **10-13**: 81-91.

Bhattacharya, K. B. a. S. (2011). "Power Generation from Coal. Ongoing Developments and Outlook."

Bose, S. C. (2005). Mater. Sci. Eng. A **395** 110-115.

Cambridge (2013). "www.doitpoms.ac.uk/tlplib/creep/mechanisms.php."

Cerjak, H. (2008). Creep Strength of Welded Joints of Ferritic Steels. Creep Resistant Steels. F. Abe. Great Abington, Abington Publishing**:** 472-503.

Cerri, E. (1998). Mater. Sci. Eng. A **245**: 285-292.

Dimmler, G. (2008). Int. J. Pres. Ves. Pip **85**: 55-62.

Easterling, K. (1992). Introduction to the Physical Metallurgy of Welding. Oxford, Butterworth-Heinemann Ltd.

ECCC (2004). Data Acceptability and Data Generation: Creep Data for Welds.

ECCC (2005). ECCC Data Sheets. International ECCC Conference. London.

Ennis, P. J. (1997). Acta Mater. **45**: Acta Mater. .

EPRI (2006). *X20CrMoV12-1 Steel Handbook*. Palo Alto, CA. **1012740**.

Eskom (2013). "http://www.eskom.co.za/c/40/company-information/."

Foldyna, V. (1996). Steel Res **67**: 375-381.

Francis, J. A. (2006). Materials Science and Technology **22**: 1387-1395.

Francis, J. A. (2006). ASM International Conference on Trends in Welding Research

Francis, J. A. (2009). Science and Technology of Welding and Joining **14**: 436-442.

Frost, H. J. (1982). Deformation Mechanism Maps. . The Plasticity and Creep of Metals and Ceramics., British Library Cataloguing in Publication Data.

Giannuzzi, L. A. (1999). Science Direct **30**: 197 - 204.

Gladman, T. (1998). "Principles of Microstructural Stability in Creep Resistant Alloys. ." Microstructural Stability in Creep Resistant Alloys: 49 - 68.

Gustafson, Å. (2002). Mater. Sci. Eng. A **333**: 279-286.

Hagen, I. v. (2002). International Syposium on Niobium, Orlando.

Hagen, I. v. (2002). Creep Resistant Ferritic Steels for Power Plants. International Syposium on Niobium, Orlando.

Hald, J. (1996). Steel Res **67**: 369-374.

Hald, J. (2008). Int. J. Pres. Ves. Pip. **85**: 30 - 37.

Hättestrand, M. (2001). Mater. Sci. Eng. A **318**: 94-101.

Hess, W. F. "The Measurement of Cooling Rates Associated with Arc Welding and their Application to the Selection of Optimum Welding Conditions." Welding Journal **22**: 377-s to 422-s.

Hofer, P. (2002). " " ISIJ Int. **42**: 62-66.

Holzer, I. (2010). Computational Modelling of the Strength Evolution during Processing and Service of 9-12%Cr Steels. Faculty of Mechanical Engineering. Graz, Graz University of Technology. **Dr. of technology**.

Hongyang, J. (2010). Transactions of JWRI **39**(No. 2).

Kalwa, G. (1978). VGB Kraftwerkstechnik. **58:** pp. 604-613.

Kauhausen, E. (1957). Schweißen und Schneiden **9**: pp. 414-419.

Klueh, R. L. (2001). "High Chromium Ferritic and Martensitic Steels for Nuclear Applications."

Kostka, A. (2007). Acta Mater. **55**: 539-550.

Krauss, G. (1999). Mater. Sci. Eng. A **273-275** 40-57.

Laha, K. (2007). Metallurgical and Materials Transactions A **38A**: 58-68.

Lee, J. S. (2006). Mater. Sci. Eng. A **428**: 539-550.

Li, J. (2012). Advance Techniques in TEM Specimen Preparation. The Transmission Electron Microscope. D. K. Maaz.

Maitland, T. (2007). "Electron Backscatter Diffraction (EBSD) Technique and Materials Characterization Examples."

Malis (1988). "EELS Log-Ratio Technique for Specimen-Thickness Measurement in the TEM." journal of Electron Microscopy Technique. **8**: 193-200.

Mannan, S. L. (1999). Trans. Ind. Inst. Met **49**: 303 - 320.

Marder, A. R. (1989). "Replication Microscopy Techniques for NDE." ASM Handbook **17**: 52 - 56.

Maruyama, K. (2001). ISIJ Int. **41**: 641-653.

Masuyama, F. (2000). Key Eng Mater **171-174**: 99-107.

Mayer, K. H. (2008). Creep resistant steels, Cambridge Woodhead Publishing.

Middleton, C. J. (1996). Int. J. Pres. Ves. & Piping **66**: 33-57.

Nabarro, F. R. N. (1995). The Physics of Creep.

Nutting, J. (1998). "The Structural Stability of Low Alloy Steels for Power Generation Applications. ." Advanced Heat Resistant Steels for Power Generation.: 12 - 30

Panait, C. (2010). Mater. Sci. Eng. A **527**: 4062–4069.

Panait, C. (2010). Int. J. Pres. Ves. & Piping **87**: 326-335.

PD6525 (1990). Elevated temperature properties for steels for pressure purposes. Stress rupture properties.

Pešička, J. (2003). Acta Materialia **51**: 4847 - 4862.

Pešička, J. (2010). Scripta Materialia **62**: 353 - 356.

Pickering, F. B. (1978). Physical Metallurgy and the Design of Steels. London.

Poorhaydari, K. (2005). Welding Journal.

Sawada, K. (2001). Mater. Sci. Eng. A **319-321** 784-787.

Sawada, K. (2008). Materials Characterization **59**: 1161 - 1167.

Schinn, R. (1969). VGB Werkstofftagung**:** 54-89

Schuller, H. J. (1974). "Cracking in the Weld Region of Shaped Components in Hot Steam Lines - Material Investigations." Der Maschinenschaden **47**: 1-13.

Shen, Y. Z. (2008). J. Nucl. Mater **374**: 403-412.

Sonderegger, B. (2005). Characterisation of the Substructure of Modern Power Plant Steels using the EBSD-Method, Graz University of Technology. **Phd**.

Sonderegger, B. (2006). Ultramicroscopy **106**: 941 - 950.

Sonderegger, B. (2008). Mater. Sci. Eng. A **481-482** 466-470.

Sonderegger, B. (2011). Compute Methods in Material Science **11**(No. 1).

Spigarelli, S. (2002). Materials and Design **23**: 547-552.

Struers (2010). Preparation of ferrous metals for Electron Backscatter Diffraction (EBSD) analysis.

Tamaki, K. (1982). Precipitates of Carbides during Tempering of Cr-Mo Steels. Department of Mechanical and Metarials Engineering.

Tian, Z. L. (1991). Int. J. Pres. Ves. & Piping **46**: 339 - 348.

Tuma, J. V. (2009). Investigations of the effect of Carbide Precipitates Density on the Resistance of Welds to Accelerated Secondary Creep. ECCC Creep Conference, Zurich, DEStech.

Van-Zyl, F. H. (1997). Operating Pressure Equipment, Brisbane, Australia.

Van-Zyl, F. H. (2005). Life Assessment and Creep Damage Monitoring of High Temperature Pressure Components in South Africa's Power Plant. ECCC Creep Conference. London**:** 932-943.

Van-Zyl, F. Z. (2000). VGB International Materials Conference. Pretoria, South Africa.

Williams, D. B. (2009). Transmission Electron Microscopy. New York.

Xue, W. (2009). Nonferrous Met. Soc. **19**: s772 - s775.

Zhang, W. (2004). Probing Heat Transfer, Fluid Flow and Microstructural Evolution during Fusion Welding of Alloys. Material Science and Engineering, The Pennsylvania State University.